

**STRUCTURAL MONITORING WITH FIBER BRAGG GRATING STRAIN  
SENSOR ARRAY AND OPTICAL FREQUENCY DOMAIN  
REFLECTOMETRY**

**by**

**Abdeq Mohamed Abdi**

---

**A Dissertation Submitted to the Faculty of the**

**COLLEGE OF OPTICAL SCIENCES**

**In Partial Fulfillment of the Requirements  
For the Degree of**

**DOCTOR OF PHILOSOPHY**

**In the Graduate College**

**THE UNIVERSITY OF ARIZONA**

**2005**

THE UNIVERSITY OF ARIZONA  
GRADUATE COLLEGE

As members of the Dissertation Committee, we certify that we have read the dissertation prepared by Abdeq M. Abdi

entitled Structural Monitoring with Fiber Bragg Grating Strain Sensor Array and Optical Frequency Domain Reflectometry

and recommend that it be accepted as fulfilling the dissertation requirement for the Degree of Doctor of Philosophy

Alan R. Kost Date: 11/17/2005

Seppo Honkanen Date: 11/17/2005

Franko Kueppers Date: 11/17/2005

Final approval and acceptance of this dissertation is contingent upon the candidate's submission of the final copies of the dissertation to the Graduate College.

I hereby certify that I have read this dissertation prepared under my direction and recommend that it be accepted as fulfilling the dissertation requirement.

Alan R. Kost Date: 12/05/2005  
Dissertation Director:

### **STATEMENT BY AUTHOR**

This dissertation has been submitted in partial fulfillment of requirements for an advanced degree at The University of Arizona and is deposited in the University Library to be made available to borrowers under rules of the Library.

Brief quotations from this dissertation are allowable without special permission provided that accurate acknowledgment of source is made. Requests for permission for extended quotation from or reproduction of this manuscript in whole or in part may be his or her judgment the proposed use of the material is in the interests of scholarship. In all other instances, however, permission must be obtained from the Author.

SIGNED: Abdeq M. Abdi

## ACKNOWLEDGEMENTS

I would like to express thanks to those who made this research possible. First, special thanks go to the College of Optical Sciences for extending me the GAANN Fellowship and the Alfred P. Sloan Foundation for extending the Alfred P. Sloan Scholarship. Specifically, I would like to thank Professor Richard Shoemaker and Ms. Barbara Myers of the College of Optical Sciences academic programs. Second, I would like to thank my advisor Professor Alan Kost for his advice, support, and for pushing my research forward. Third, I would like to thank Shigeru Suzuki, Mike Morrell, and Professor Axel Schülzgen for taking part of their valuable research time to work on this project and use of their facilities. Shigeru was very instrumental in the fabrication phase of this project.

Finally, I would like to thank my parents Mohamed and Saada, my grandmother Halimo, and my siblings Fardussa, Abdullahi, Khadar, Farah, and Omar for their patience and support throughout my academic career.

## TABLE OF CONTENTS

LIST OF FIGURES .....	7
LIST OF TABLES .....	10
ABSTRACT .....	11
1. INTRODUCTION .....	12
2. SMART STRUCTURES .....	18
2.1. Philosophical basis of smart structures .....	18
2.2. Infrastructure Optics (IO) .....	21
2.3. Software implementations .....	22
3. FIBER OPTIC WAVEGUIDE .....	26
3.1. Maxwell's and the Wave Equations .....	26
3.2. Propagation in cylindrical waveguide .....	27
3.3. Fields within a step index (SI) optical fiber .....	30
4. FIBER BRAGG GRATINGS .....	36
4.1. Couple Mode Theory .....	36
4.2. Uniform fiber Bragg gratings .....	39
4.3. Transfer Matrix Method .....	43
4.4. Fabrication methods .....	44
4.5. Boron/Germanium co-doped fibers .....	47
4.6. Grating equation and Bragg diagram .....	47
4.7. Experiment .....	50
5. INTERFEROMETRY .....	53
5.1. Two beam interferometer .....	53
5.2. Multi-beam interferometer .....	55
5.3. Temporal Coherence .....	58
5.4. Fiber optic Fabry-Perot displacement sensor .....	60
6. POLARIZATION .....	66
6.1. Physical description .....	66
6.2. Measurement of polarization .....	67
7. BASIC MECHANICS OF MATERIALS .....	72
7.1. Axial stress and strain .....	72
7.2. Stress-strain curves .....	73
7.3. Hooke's Law .....	75
7.4. Deflection of beams .....	77
7.5. Finite element representation .....	79
8. OPTO-MECHANICAL RELATIONS .....	85
8.1. Temperature and strain sensitivities .....	85
8.2. Photoelasticity .....	87
8.3. Fabry-Perot Strain Gauge Calibrator .....	89
8.3.1. FPI strain gauge calibration setup and sensors .....	93
8.4. Experiment and Results .....	95

**TABLE OF CONTENTS - Continued**

8.4.1.	Piezoceramic actuator characterization.....	95
8.4.2.	Strain gauge factor for an ESG.....	98
8.4.3.	Strain gauge factor for a FBG.....	99
8.5.	Discussion.....	101
8.6.	Conclusion.....	104
9.	FIBER OPTIC SENSORS AND DISTRIBUTION METHODS.....	105
9.1.	Fiber optic sensors.....	105
9.2.	Distributed optical sensing techniques.....	111
10.	MODELING OF FBGA AND C-OFDR SYSTEMS.....	120
10.1.	Modeling FBGA system using diffractive optics.....	120
10.2.	Cavity interferences.....	123
10.3.	Transfer Matrix Approach.....	125
10.3.1.	FBGA and C-OFDR.....	126
10.3.2.	FBGA/C-OFDR design and simulation.....	130
10.3.3.	FBGA system fabrication.....	133
10.3.4.	FBGA and C-OFDR testing.....	133
10.3.5.	C-OFDR and FBGA results.....	135
10.3.6.	Discussion.....	138
10.4.	Conclusion.....	141
11.	CAVITY SUPPRESSION IN FBGA/C-OFDR SYSTEM.....	143
11.1.	Reducing FBG reflectance.....	143
11.2.	Down shifting method.....	145
11.3.	Cavity interference suppression method.....	146
11.3.1.	Cavity interference suppression simulation and results.....	148
11.3.2.	Design implementation.....	153
11.4.	Conclusion.....	158
12.	SUMMARY AND FUTURE WORK.....	160
12.1.	Summary.....	160
12.2.	Future Work.....	162
12.2.1.	Bandwidth Reduction.....	162
12.2.2.	2D FBGA/C-OFDR systems.....	164
	REFERENCES.....	166

## LIST OF FIGURES

Figure 2.1 Smart Structure System .....	19
Figure 2.2 Vern Diagram (Measures 2001) .....	20
Figure 2.3 Block diagram of an Infrastructure Optic system.....	22
Figure 2.4 Front panel display of FBGA simulation software. a) Schematic layout software and b) Signal processor. ....	24
Figure 2.5 OFDR and FBGA simulator with GUI interface.....	25
Figure 3.1 Cylindrical coordinate system .....	28
Figure 3.2 Step index optical fiber.....	30
Figure 3.3 (a) Field and intensity distribution of linear polarization modes ( $LP_{vm}$ ). (b). Normalized propagation constant versus the normalized frequency ( $V$ ) for LP modes (Okamoto 2000). ....	34
Figure 4.1 Grating structure.....	36
Figure 4.2 Sinusoidal variation of the refractive index.....	39
Figure 4.3 Division of complex grating structure into N simple grating structures .....	44
Figure 4.4 Holographic two beam interference method .....	46
Figure 4.5 Phase mask technique.....	46
Figure 4.6 Bragg diagram .....	49
Figure 4.7 FBG fabrication using a double frequency Argon laser and phase mask.....	51
Figure 4.8 (a) Change in the modulation index as a function of the exposure time. (b). Reflectance spectrum of the FBG .....	52
Figure 5.1 Michelson interferometer .....	53
Figure 5.2 Fabry-Perot interferometer .....	56
Figure 5.3 Transmittance spectrums for 1cm FPI as a function of mirror reflectance and finesse. ....	58
Figure 5.4 Fiber optic Fabry-Perot interferometric displacement sensor. ....	61
Figure 5.5 Transmittance and visibility curves for the fiber optic Fabry-Perot displacement sensor as a function of the cavity spacing.....	64
Figure 6.1 Polarization state of a field as the phase difference goes through a single revolution. ....	67
Figure 6.2 Measurements of the Stokes components using a polarizer with transmission along the x-axis and quarter-wave plate with fast axis along the x-axis. ....	68
Figure 7.1 Axial strain and stress.....	72
Figure 7.2 Stress-strain curve of mild steel. ....	73
Figure 7.3 Typical strain-stress curve for brittle materials. ....	74
Figure 7.4 (a) Cantilever beam. (b) Deflection of the beam subject to distributed shear force $f(x)$ . (c) Close up of a small section of the deflected beam. ....	77
Figure 7.5 Finite element model for a beam.....	80
Figure 7.6 Block diagram implementation of the FEM.....	83
Figure 7.7 2 meter 1 degree tapered cantilever beam with 500 N tip force. (a) Layout of the beam (b) deflection and axial strain along the length of the cantilever beam. ....	83

### LIST OF FIGURES - Continued

Figure 8.1 The orthogonal directions in an optical fiber shown in Eq. 8.11 (Measures 2001) .....	87
Figure 8.2 The physical layout of the Fabry-Perot interferometric (FPI) strain gauge calibration system. ....	91
Figure 8.3 Main components of FPI strain gauge calibrator. (a) Mono-morphic piezoceramic actuator and (b) FPI displacement and test sensor. ....	92
Figure 8.4 (a) Hardware setup used to measure the strain gauge factor of a fiber Bragg grating (FBG). (b) Hardware setup used to measure the strain gauge factor of an electric strain gauge (ESG). ....	95
Figure 8.5 Plot of the Fabry-Perot interferometric signal and the voltage applied to the piezoceramic actuator as the sample number varies from 0 to 780. ....	97
Figure 8.6 Plot of the displacement of the piezoceramic actuator as a function of the applied voltage. The load on the actuator was sensor holder #1 (SH#1) only.....	97
Figure 8.7 Plot of the fractional change in the quarter Wheatstone bridge voltage as a function of the measured axial strain. The solid line is a linear fit of the four data points. Note that the linear fit was forced to cross the origin. ....	99
Figure 8.8 Plot of the fractional change in the center wavelength of the FBG as a function of the measured axial strain using the FPI strain gauge calibration setup. The solid line is a linear fit of the four data points. Note that the linear fit was forced to cross the origin. ....	100
Figure 9.1 Intensity based fiber optic sensors: (a) Fiber optic displacement sensor, (b) Microbend optical sensor, and (b) Evanescent optic sensor .....	106
Figure 9.2 Types of interferometers: (a) Michelson, (b) Mach-Zhender, (c) Fabry-Perot, and (d) Polarization based interferometer. ....	108
Figure 9.3 Interrogation of fiber Bragg grating (FBG) sensor using (a) edge filter, (b) FPI, and (c) unbalanced Michelson. ....	110
Figure 9.4 Optical time domain reflectometry for (a) continuous sensing of optical sensors (OTDR) and (b) discrete sensing of optical sensors (Time Division Multiplexing). ....	113
Figure 9.5 Examples of quasi-distributed sensors using (a) wavelength division multiplexing (WDM) for FBGs and (b) coherent multiplexing for fiber optic Fabry-Perot interferometers (FPI).....	114
Figure 9.6 Distributed sensing using optical frequency domain reflectometry (C-OFDR). ....	115
Figure 10.1 C-OFDR interrogation of an N-element FBGA system. ....	121
Figure 10.2 A model of a N-element fiber Bragg grating array with a backend reference reflector. ....	122
Figure 10.3 Block diagram implementation of Sensor Process for transfer matrix modeled devices. ....	128
Figure 10.4 Block diagram implementation of the Signal Processor for C-OFDR system .....	130

### LIST OF FIGURES - Continued

Figure 10.5 (a) Design of the three-elements, 15.3 cm FBGA and the resulting interference signal in the (b) wavelength domain (c) and the Fourier domain.....	132
Figure 10.6 (a) FBGA and ESG attachment to a cantilever beam host. The tip of the cantilever beam is varied and the corresponding strain information from the FBGA and ESGs are compared. (b) Close up look of the FBGA and ESGs on the cantilever beam. .....	134
Figure 10.7 The figure shows the FBGA reflectance spectrum in the (a) wavelength and b) Fourier domain. ....	136
Figure 10.8 (a) ESG and FBGA results as function of cantilever beam tip displacement and axial position. b) Percent strain error of each FBG in the array with respect to ESGs results as function of tip displacement.....	137
Figure 10.9 The figure shows the simulated FBGA reflectance in (a) the Fourier domain with a 2.5 pm uniform noise added to wavelength increment. (b) FBGA demodulated spectrum.....	139
Figure 11.1 Model of FBGA/C-OFDR using cavity downshifting method .....	145
Figure 11.2 Cantilever beam model with end force F and attached FBGA.....	148
Figure 11.3 Interferences between FBGA and reflector with (b) no load and (a) 500 N force on the cantilever beam tip.....	149
Figure 11.4 Interference between FBGA and reflector in the Fourier Domain with (a) no load, (b) no load with cavity suppression, (c) 500 N end force, (d) 500 N end force with cavity suppression.....	151
Figure 11.5 (a) individual FBG prototype spectrum. (b) OFDR demodulation for strained FBG sensor # 5. (c) OFDR and FEM strain results. (d) Percent strain error between FEM and OFDR results.....	152
Figure 11.6 Cavity suppression systems using (a) Michelson and (b) FPI configurations. .....	154
Figure 12.1 Several FBGA designs. (a) Regular single line FBGA (b) Array of Fabry-Perot Interferometers (FPI) connected through phase lines (PL). (c) Two smaller FBGA sections connected through a phase line (PL).....	164
Figure 12.2 2D FBGA system .....	165

**LIST OF TABLES**

Table 11.1. Cantilever beam, FBGA, and wavelength scanning specification for C-OFDR demodulation simulation.....	149
--	-----

## ABSTRACT

In this work, concepts of smart structures, health monitoring systems, and Infrastructure Optics are discussed. This accumulates in the development of the Optical and Structural Simulation software that integrates all key components of Infrastructure Optics. Recent developments in the use of Coherent Optical Frequency Domain Reflectometry (C-OFDR) to interrogate Fiber Bragg Grating Arrays (FBGA) have shown promise in its use in infrastructure health monitoring systems. In this work, the modeling, design, simulation, fabrication, calibration, and testing of a three-element, 15.3 cm fiber Bragg grating strain sensor array with C-OFDR interrogation technique are demonstrated. The FBGA/C-OFDR was initially simulated using in-house software that incorporates transfer matrices. Compared to the previous techniques used, the transfer matrix method allows a system wide approach to modeling the FBGA/C-OFDR system.

In the second half of this work, a cavity interference suppression method is used to suppress interferences between fiber Bragg gratings. The cavity interference suppression method is simulated using two transfer matrices, after which, a practical design using a circular polarized source and polarization devices is proposed. Compared to previous techniques, the cavity interference suppression method does not require down shifting the cavity interferences to a lower frequency band, potentially saving fiber material and bandwidth.

## 1. INTRODUCTION

The history of human civilization is divided into ages that characterize the predominant stage of material technology. The Stone Age, followed by the Bronze, Iron, and finally the Synthetic Material Age are defining periods in human history. In each subsequent age, the reliability, functionality, and structural behavior of materials steadily increased, improving the quality of life as compared to earlier human existence (Gandhi 1992). The revolution in materials was also the driving force that launched the agriculture, industrial, computer, and the current information revolution. Yet again, another age is dawning - the Smart Materials Age. In this age, materials will not only structural and functional but also intelligent. Like the nerves and muscles of a vertebrate, they will be able to monitor and appropriately respond to external stimuli as determined by pre-defined goals, or using artificial neural systems give learned responses. This new age has the potential to launch yet another revolution; a revolution that combines information systems with smart materials to give birth to countless new technologies. In this work, one aspect of smart structures called structural health monitoring systems will be discussed. Recent and previous events have shown a need for smart infrastructure. The civil infrastructure in the United States is seriously deteriorating. Research has shown that half a million bridges or 42% of the bridges in the US are structurally deficient (Measures 2001). It is estimated that the cost will be over \$90 billion (1996 dollars) plus to fix. Such costs represent an enormous investment. It would be desirable for bridges to be able to sense their structural integrity and provide real time information to preventative maintenance organization so that areas of concern can be addressed before

the structures deteriorate beyond repair and/or costs become prohibitive. Another area of smart structures is in national security. One big issue occurred during the terror attacks of the World Trade Tower in New York City on September 11, 2001 was a lack of real time information of the structural integrity of the Towers. Recent documentation has shown that the towers clasped due to weakening and distortion of the steel skeletal frames due to high temperatures (Eagar 2001). The Towers were designed to withstand a direct impact with a Boeing 707; however, no considerations were given to thermodynamic effects. If the Towers were smart, then structural information would potentially have given emergency and civilian personnel early warning about the stability of the towers. Health monitoring systems can also play a role in the monitoring of other critical infrastructures such as high value public building, chemical plants, and pipelines. Another area that health monitoring systems can play is improving efficiencies and competitiveness. In today's world, the cost of raw materials and energy are increasing at a fast rate. Most of the energy today is spent on maintaining infrastructure, especially, heating and cooling buildings, and power equipments within. In addition to having strain sensors to monitor the structural integrity, heavily distributed temperature sensors can be embedded into walls and floors so that large area of the structure can be monitored instead of having point temperature sensors. This will allow monitoring of the entire temperature boundary condition of structures and point out areas of deficiency more accurately. Finally, another major area smart structures can play is space and planetary exploration. It would be unimaginable to have manned space mission to places like Mars without having smart structures because the environments are very hostile to human life.

A single failure in the structural integrity of spacecrafts or terrestrial structures can become catastrophic; it would be desirable to pin point areas of concern before they become life treating issues. Even when human life is not at stake, vehicles such Mars Rovers have shown the potential for vehicles that can operate autonomously (Woerner 2002) with little human supervision thereby expanding the usefulness and life cycle of the vehicles.

In this work, the primary interest is Infrastructure Optics which is defined as the design of optical systems, primarily fiber optics systems and devices, for use in infrastructure health monitoring systems. Compared to electrical sensing methods, fiber optic sensors are immune to electromagnetic interference, non-volatile, are able to be multiplex and distributed along several fiber lines, and can be integrated with current optical communication systems (Udd 1995). A particular type of interrogation system call Optical Frequency Domain Reflectometry (OFDR) has shown great promise in its use in HM systems due to its ability to interrogate thousands of identical sensors. Optical Frequency Domain Reflectometry (OFDR) can be divided into two categories, incoherent (I-OFDR) and coherent (C-OFDR). In C-OFDR, a highly coherent tunable laser wavelength (frequency) scans a (quasi) distributed optical system under test (Eickhoff, et al. 1981, Pierce, et al. 2000). The resulting internal reflections from the optical system produce interferences and beat frequencies (readily observed using a spectrum analyzer) that are directly related the positions and magnitude of the internal reflections. For an I-OFDR system, the intensity of the laser source is modulated instead of the wavelength (MacDonald 1981). For a C-OFDR, resolution down to micron range can be achieved

and the measurement bandwidth can arbitrarily be chosen. OFDR systems have also been used in distributed fiber optic sensors to measure various parameters such as strain, temperature, and pressure, and using various sensing techniques from Rayleigh backscattering (Froggatt, et al. 1998) , micro-bend losses (Pierce, et al. 2000), interferometric (Fuhr, et al. 1993) to wavelength based sensing systems. A wavelength based quasi-distributed sensing system such as an array of fiber Bragg gratings (FBGA) can easily be incorporated into a C-OFDR demodulation system since the measurement parameters are in terms of wavelength. Fiber Bragg Gratings (FBG) offer additional advantage compared to other sensing methods in that there is a linear strain to wavelength change relation and the grating fabrication procedure is inexpensive by either using the two beam or phase mask method, however, requires a large initial capital investment (Measures 2001).

Various methods have been used to simulate the interrogation of a FBGA system with C-OFDR. Froggatt et al. 1996 conducted an analysis of the demodulation of a FBGA with C-OFDR interrogation using a variation of the coupled mode theory. The analysis showed that for a weakly guided and low reflectivity FBGA system (FBGA plus a reference reflector), the Fourier transform of C-OFDR signal gives the positional information of each FBG in the array, and a narrow inverse Fourier transform at selected positions within this Fourier transform can then be used to recover the wavelength spectrum of a particular FBG. Childers, et al. 2002 used the Fourier transform of a sinusoidal phase grating to approximate the FBG and then summed multiple phase-shifted gratings plus the contribution from a reference reflector to model the FBGA

system. Duncan, et al. 2002 approximated the interference between the reference reflector and a low reflective FBG using the two beam interference method and then summed the contribution from each FBG in the array to model the FBGA system.

In this work, an original contribution done by this research is the use of transfer matrices to model a FBGA/C-OFDR system. The transfer matrix method allows a system wide approach to modeling the FBGA/C-OFDR system. An elemental transfer matrix can represent the optical and geometrical characteristics of a single element in the FBGA system. The response of the entire FBGA system is then determined simply by multiplying all the elemental transfer matrices in the proper order. The advantage of this approach is that any optical device can efficiently be incorporated if its transfer matrix is known. Unlike the previous techniques, higher interferences will also be taken into account and the reflectance of the FBGA/C-OFDR system can be determined directly. In this work, higher order interferences will be defined as interference resulting from multiple pass through the FBGA system and interference between the beats. Another area of FBGA/C-OFDR design is reducing the interferences between FBGs in the array. It is possible for the cavity interferences to super impose onto FBG-reflector interferences when their corresponding beat frequencies are equal, resulting in the distortion of the recovered FBG spectrums. Several techniques have been implemented to eliminate the cavity interferences. The first technique is to reduce the reflectance of the FBGs to a level that minimizes the cavity interferences. A second technique is to design the FBGA system such that the cavity interferences and the FBG-reflector interferences do not overlap. The third method is to down shift the cavity interferences to a lower frequency band

(Froggatt, et al. 1998). An original contribution done by this research is to subtract the cavity interferences directly from the overall FGBA system interference signal. The transfer matrix method will be used to analyze this technique by employing two transfer matrices. One transfer matrix represents the cavity interferences, while the second transfer matrix contains the interference between the reflector and the FBGA and the cavity interferences (Abdi, et al. 2004). The resulting reflectances from the two transfer matrices are then subtracted to suppress the cavity interferences. This technique will be implemented on a 9 element, 2 meter FBGA/C-OFDR system. The FBGA/C-OFDR will be used to monitor the axial strain field of a simulated 2 meter steel cantilever beam as the beam is subject to a 500 N tip load. The effects of the axial field on the FBGA/C-OFDR system will be discussed and the efficacy of the cavity suppression investigated. Finally, a practical implementation of the cavity suppression technique will be proposed using polarization devices and a circularly polarized source.

The main topics covered in this dissertation were previously part of two conference papers: *Infrastructure Optics* and *Fiber Bragg Grating Array Calibration*. Both papers were published in SPIE's Smart Structures and Materials and NDE (Non-destructive Evaluation) Symposium from 2004-2005. The subject matter in *Infrastructure Optics* is spread out in Chapter 2 and the subject matter in *Fiber Bragg Grating Array Calibration* is spread out in Chapters 3 and 8. An invited article based on *Fiber Bragg Grating Array Calibration* paper was submitted to the Journal of Smart Structures and Systems, An International Journal.

## **2. SMART STRUCTURES**

In this chapter, the philosophical basis of smart structures and its relation to biological system will be given. The origins and concept of Infrastructure Optics (IO) will be discussed and its relationship to smart structures explained. Towards the end, software tools used in this dissertation research to perform simulations will be discussed and its basic block diagram outlined.

### **2.1. Philosophical basis of smart structures**

The goal of a smart structure system is to model engineering systems after biological systems; put simply: to make inanimate structures behave like living systems (Udd 1994, Gandhi 1992). As shown in Figure 2.1, three basic components make a full smart structure system: structure, sensing, actuation, and processing. To analogies living systems; the Processor is the brain of the structure; the actuators are its muscles; the sensors detect changes in the structure's environment similar to our nerves. The physical parameters that can be measured can be strain, temperature, pressure, etc by either optical or electrical means. The signal processor then converts the resulting signal from the sensors into an electronic signal or a format suitable for further processing by a computer or by an embedded system. The processor will then process the electronic signal from the signal processor and determine the state of the structure using pre-defined metric or can be learned by using artificial neural systems (Gandhi 2001, Udd 1995). The metrics can be referenced with respect to the performance, health, vibrations, or damage on the structure. Using the results from the processor, the actuators can then be used to return

the structure to its optimum performance level, for example, reduce the temperature, stress, or decrease structural vibrations.

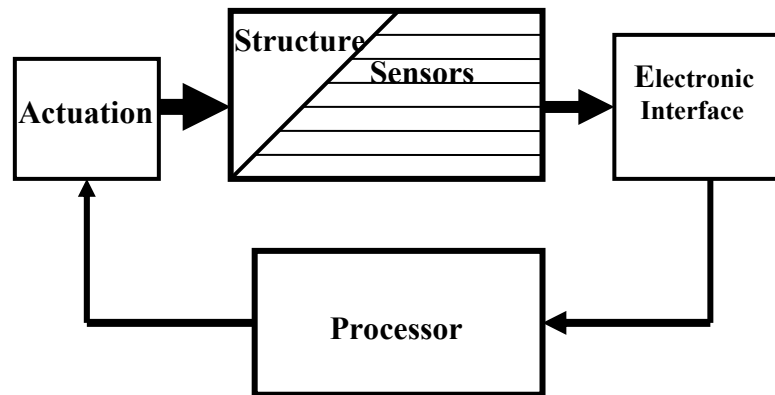


Figure 2.1 Smart Structure System

An interesting visual example of smart structures was proposed by Measures (2001) and is shown in Figure 2.2. In the figure, four basic components make up a full smart structure: structure, sensing system, actuation, and neural networks (learning algorithms).

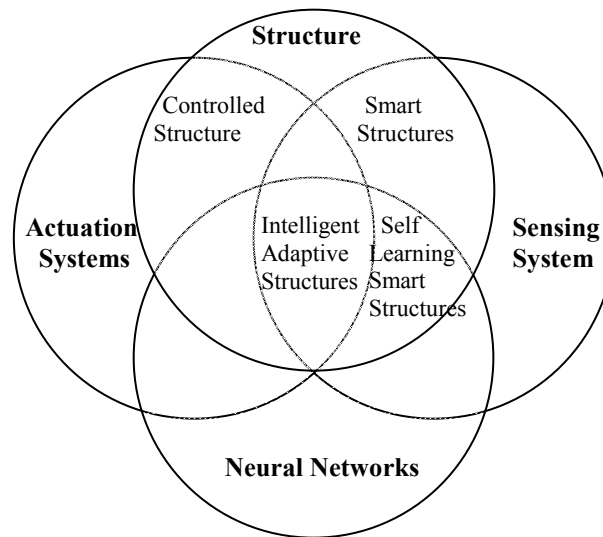


Figure 2.2 Vern Diagram (Measures 2001)

To meet the minimum definition of smart structures, the structure must be capable of sensing its environment; structures with only structurally integrated sensing are called health monitoring (HM) systems. A HM system is defined as a process in which the physical performance of structures is continually or intermittently monitored using embedded/attached sensors in order to determine the state of the structure using pre-defined metrics such as stress points, temperature, load, and previous history. Aktan, et al. 2002 analogized smart structures to the field of preventive medicine, where common and highly probable ailments are routinely monitored so that they can be caught in an early stage where they are most curable. HM system is considered a precursor to a full smart structure implementation. If the structure is capable of learning in addition to sensing, the structure is termed self-learning smart structure. If the structure is capable of

responding to its environment in addition to sensing and learning, the structure is termed an intelligent adaptive structure.

## **2.2. Infrastructure Optics (IO)**

The College of Optical Sciences (OSC) at the University of Arizona previously had no research in the area of smart structures which understandable since the field is still in the embryonic stage. Because of the author interests and previous graduate experience in smart structures (Abdi 1999, Abdi, et al. 2003), the author wanted to continue working in the area in the college. The author attended his first Smart Structures and Material Symposium during March 2002 and later wrote an informal proposal for his GAANN fellowship during the following summer and later submitted to Professor Alan Kost and Professor Richard Shoemaker, Associate Dean of OSC academic programs. The title of the proposal was Infrastructure Optics. First, the title was chosen to show that the field of smart structures is an integral component of optics and to also emphasis two key areas: infrastructure (building, roads, and bridges) and optics. Second, to show that this is a true field and like most courses contain only one or two words maximum (marketing). The word smart was not included since in the future such concept would be understood and common. Infrastructure Optics (IO) is defined as the research, development, implementation, and deployment of optical systems and devices, primarily fiber optic communication technology, for use in civil infrastructure health monitoring systems. This includes embedding/attaching distributed optical sensor networks into structural materials for buildings, roads, highways, and using a variety of novel demodulation schemes to access structural information such as strain, pressure, and temperature information over a

wide area. The main emphasis of the author's research was not building the "brain" of the system similar to what was discuss in the previous section but to focus primarily on the structure, sensing networks, and the signal processing systems as shown in Figure 2.3.

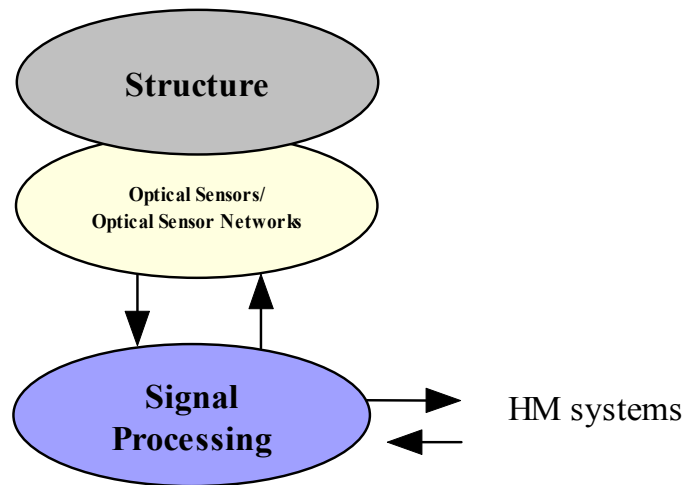
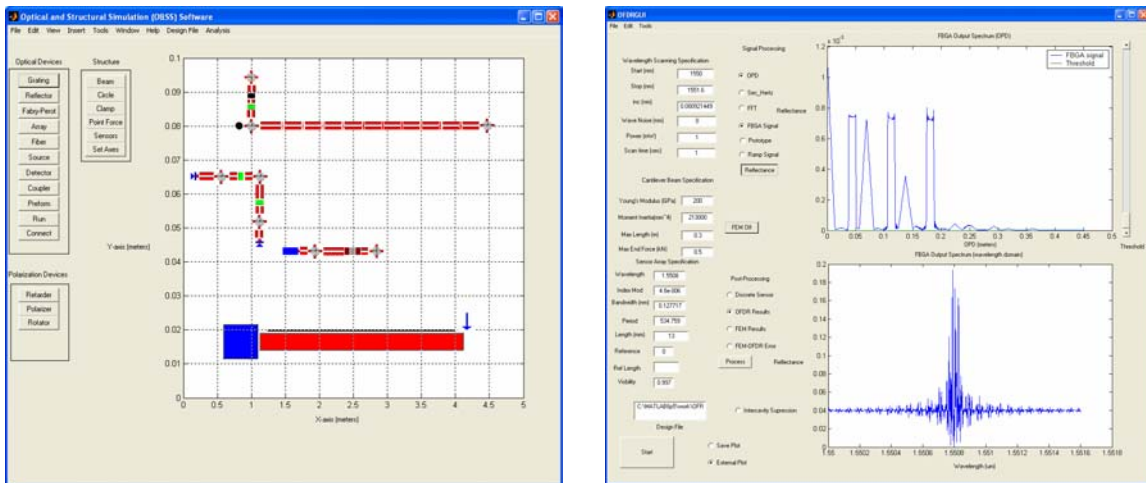


Figure 2.3 Block diagram of an Infrastructure Optic system

### 2.3. Software implementations

In order to full implement the IO system concept for a particular application, two GUI (Graphical User Interface) Matlab based simulation software were developed to integrate all three key components of the IO system (as shown in Figure 2.4) into one platform software called the Optical and Structural Simulator. The first GUI allowed the design of the IO system in an object oriented fashion and also performed the structural and optical analysis. The second GUI is the signal processor. In the layout GUI, optical devices such as gratings, couplers, reflectors, sources, detectors, and polarization devices

can be used to design a complete fiber optic measurement system. In addition to the optics, structures such as beams, columns, rods, and disks can be designed using the finite element method (FEM). The 1D FEM engine used in the OSS is a modified coded written by Professor Reddy (Reddy 1993) in the FORTRAN language. A translator was coded in Matlab to interact with this software. Currently, the translator is only capable of translating a beam problem; however, the FEM software is capable of analyzing disks, columns, and trusses. The original FEM code used in Abdi, et al. 2003 was written in-house, however, was only capable of beam structure analysis. The main reason why it would be of interest to do a structural analysis is to optimize the sensors to structural performances and to demonstrate an integrated approach. Figure 2.5 shows the block diagram of the processor software. As can be seen there are three subsystems or sub-processors: structural, optical sensor network, and signal processing. The structures like complex beams, trusses, and columns are analyzed by the FEM engine in order to properly characterize their mechanical responses.



(a)

(b)

Figure 2.4 Front panel display of FBGA simulation software. a) Schematic layout software and b) Signal processor.

Photo-elasticity can then be used to transform the mechanical response to an optical response. The optical response is then converted into an electrical response, and the signal processing model then extracts the desired measurements. The design file is automatically generated from the layout design. In addition to the design file, global parameters (optical fiber core index, sources, etc.) are automatically inserted. The design file is then inputted into the processor GUI. The Pre-Processor segments the design file into individual components (structural, sensor array, and signal processing) and passes the information to the main processor. The main processor controls the three models and extracts the desired information from each and then passes the information to the Post-Processor. Finally, the Post-Processor segments the information into individual plots, determines the error functions, and passes them to the plotting routines for end user display.

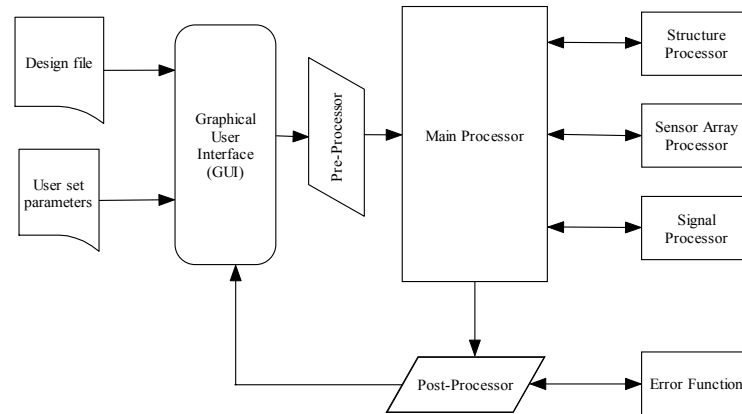


Figure 2.5 OFDR and FBGA simulator with GUI interface

During the rest of the work, more detail will be given on the sub-processors for a FBGA/C-OFDR system. In addition to the simulation of the system, the processor is also capable of processing raw experimental data. In this way, the simulation done in the layout GUI can be compared to real signals.

### 3. FIBER OPTIC WAVEGUIDE

This chapter describes the theoretical background on circular optical fiber waveguides. The wave equation in cylindrical coordinate systems will be derived from Maxwell's equations and the results applied towards solving for the modes of the optical fiber. Linear polarization (LP) modes will be discussed along with approximation methods to model the fundamental LP<sub>01</sub> mode of the optical fiber.

#### 3.1. Maxwell's and the Wave Equations

The solution for the propagations of an optical field within an optical device starts with Maxwell's equations as given by the following for a dielectric medium:

$$\text{Faraday's Law:} \quad \nabla \times \vec{E} = -\frac{\partial \vec{B}}{\partial t} \quad (3.1)$$

$$\text{Gauss's Law:} \quad \nabla \cdot \vec{D} = 0 \quad (3.2)$$

$$\text{Ampere's Law:} \quad \nabla \times \vec{H} = \frac{\partial \vec{D}}{\partial t} \quad (3.3)$$

$$\text{No monopoles:} \quad \nabla \cdot \vec{B} = 0 \quad (3.4)$$

where  $\mathbf{E}$ ,  $\mathbf{B}$ ,  $\mathbf{D}$ , and  $\mathbf{H}$  are the electric fields, magnetic flux density, electric displacement, field, and magnetic intensity vectors, respectively. The material properties are taken into account, for the case of linear, homogeneous, and isotropic media through the following relations:

$$\vec{B} = \mu_0 \vec{H} \quad (3.5)$$

$$\vec{D} = \epsilon \vec{E} \quad (3.6)$$

where  $\mu_0$  and  $\epsilon$  are the free magnetic permeability and electric permittivity of the material. The wave equation for the electric field is developed by taking the cross product of Eq. 3.1 and substituting Eq. 3.3 for the magnetic flux density, and expanding the double curls of the electric field using the BAC-CAB rule of vector identity. The resulting homogenous wave equation is the given by the following.

$$\nabla^2 \vec{E} - k^2 \frac{\partial^2 E}{\partial t^2} = 0 \quad (3.7)$$

where  $k$  is the propagation constant and is given by the following:

$$|k| = \sqrt{\mu_0 \epsilon} \omega = \frac{\omega \cdot n}{c} = \frac{2\pi n}{\lambda} = k_0 n \quad (3.8)$$

where  $\omega$ ,  $n$ , and  $k_0$  are the frequency of oscillation, effective refractive index, and the free space propagation constant.

### 3.2. Propagation in cylindrical waveguide

The best way to solve the wave equation for cylindrical symmetrical optical device is to use the cylindrical coordinate system. Figure 3.1 shows a model of a cylindrical coordinate system. The cylindrical coordinate system is completely described by a radial ( $r$ ), azimuth ( $\phi$ ), and an axial component ( $z$ ).

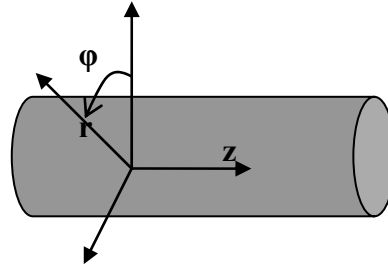


Figure 3.1 Cylindrical coordinate system

The fields propagating in the cylinder can be expressed as a summation of the fields propagating in the axial ( $z$ ), radial ( $r$ ), and azimuthally direction ( $\phi$ ):

$$E(r, \phi, z) = \hat{r}E_r(r, \phi, z) + \hat{\phi}E_\phi(r, \phi, z) + \hat{z}E_z(r, \phi, z) \quad (3.9)$$

The fields oriented in the  $r$  and  $\phi$  direction do not give a unique solution in the wave equation since they can have multiple solutions; however, the field in the  $z$  direction gives a unique solution. Converting the wave equation into the cylindrical coordinate system results in the following differential equation for an electric field with components along the  $z$ -direction (Kostuk 2002):

$$\frac{1}{r} \frac{\partial}{\partial r} \left( r \frac{\partial E_z}{\partial r} \right) + \frac{1}{r^2} \frac{\partial^2 E_z}{\partial \phi^2} + \frac{\partial E_z}{\partial z^2} + (k_0 n)^2 E_z = 0 \quad (3.10)$$

Once the  $E_z$  component field is solved, the rest of the components of the  $\mathbf{E}$  field can be obtained using Maxwell's equations. The solution of the wave equation can be determined by first using separation of variables for the  $E_z$  component and assuming

$$E_z(r, \phi, z) = R(r)\Phi(\phi)Z(z) \quad (3.11)$$

The result from the separation of variables gives the following uncoupled differential equation:

$$r^2 \frac{1}{R} \frac{\partial^2 R}{\partial r^2} + r \frac{1}{R} \frac{\partial R}{\partial r} + \frac{\partial^2 \Phi}{\partial \varphi^2} + r^2 \frac{1}{Z} \frac{\partial^2 Z}{\partial z^2} + (k_0 n r)^2 = 0 \quad (3.12)$$

Assuming an oscillatory characteristics in the z-direction,  $Z(z)=e^{-j\beta z}$ , where  $\beta$  is the propagation constant in z-direction, and rearranging like terms, the resulting differential equation further reduces to:

$$r^2 \frac{1}{R} \frac{\partial^2 R}{\partial r^2} + r \frac{1}{R} \frac{\partial R}{\partial r} - r^2 \beta^2 + (k_0 n r)^2 = -\frac{\partial^2 \Phi}{\partial \varphi^2} = \nu^2, \quad (3.13)$$

where  $\nu$  is an integer. The  $\Phi$  component is easily solved and has a solution of the form  $\Phi(\varphi)=Ae^{j\nu\varphi}$ . Plugging this result back into the uncoupled Eq. 3.12 gives the following transcendental differential equation:

$$r^2 \frac{1}{R} \frac{\partial^2 R}{\partial r^2} + r \frac{1}{R} \frac{\partial R}{\partial r} + r^2 \left( k_0^2 n^2 - \beta^2 - \frac{\nu^2}{r^2} \right) = 0 \quad (3.14)$$

It can readily be observed that the above equation has solutions in the form of Bessel

functions. For the case  $\left( k_0^2 n^2 - \beta^2 - \frac{\nu^2}{r^2} \right) > 0$ , the combined solution for the  $E_z$  field is in

the following form

$$E_z(r, \varphi, z) \sim J_\nu(\kappa r) e^{j\nu\varphi} e^{-j\beta z} + c.c. \quad (3.15)$$

where  $J_\nu$  is a Bessel function of the first kind and a sinusoidal varying term. For the

case  $\left( k_0^2 n^2 - \beta^2 - \frac{\nu^2}{r^2} \right) < 0$ , the solution is in the following form:

$$E_z(r, \varphi, z) \sim K_\nu(\gamma r) e^{j\nu\varphi} e^{-j\beta z} + c.c. \quad (3.16)$$

where  $K_v$  is a Bessel function of the second kind and a decaying term.

### 3.3. Fields within a step index (SI) optical fiber

An optical fiber is made up of core and clad regions. The clad region has a higher index of refraction than the core and help maintain total internal reflection (TIR) thereby confining most of the field to within the waveguide structure. Figure 3.2 shows a diagram for a step index (SI) fiber with core and clad refractive index  $n_1$  and  $n_2$ , respectively, and a core radius of  $a$ .

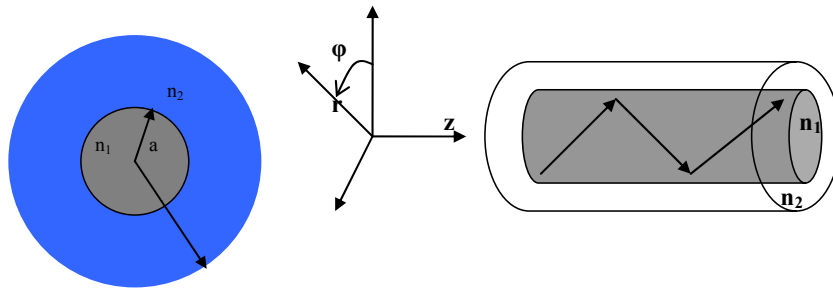


Figure 3.2 Step index optical fiber

In order for a field to propagate within the core, the propagation constant  $\beta$  must lie between:

$$k_0 n_2 < \beta < k_0 n_1 \quad (3.17)$$

The field can have a decaying or sinusoidal varying term depending on the region of the step index fiber. For a field within the core ( $r \leq a$ ), the  $E_z$  and  $H_z$  components have the following form:

$$\begin{aligned} E_z(r, \varphi, z) &= A J_v(\kappa r) e^{jv\varphi} e^{-j\beta z} + c.c. \\ H_z(r, \varphi, z) &= B J_v(\kappa r) e^{jv\varphi} e^{-j\beta z} + c.c. \end{aligned} \quad (3.18)$$

and for  $r > a$ :

$$\begin{aligned} E_z(r, \varphi, z) &= CK_v(\gamma r) e^{jv\varphi} e^{-j\beta z} + c.c. \\ H_z(r, \varphi, z) &= DK_v(\gamma r) e^{jv\varphi} e^{-j\beta z} + c.c. \end{aligned} \quad (3.19)$$

where A, B, C, and D are constants that will be determined with the aid of the boundary conditions at the core/clad interface. As stated earlier, the rest of the components for the E-field can be derived from the Maxwell's equations in the cylindrical coordinates. The following are the rest of the components for the E and H-field:

$$\begin{aligned} E_\varphi &= -\frac{j}{\kappa^2} \left[ \frac{\beta}{r} \frac{\partial E_z}{\partial \varphi} - \omega u_0 \frac{\partial H_z}{\partial r} \right] \\ E_r &= -\frac{j}{\kappa^2} \left[ \frac{u_0 \omega}{r} \frac{\partial H_z}{\partial \varphi} + \beta \frac{\partial E_z}{\partial r} \right] \\ H_\varphi &= -\frac{j}{\kappa^2} \left[ \omega \varepsilon \frac{\partial E_z}{\partial r} + \frac{\beta}{r} \frac{\partial H_z}{\partial \varphi} \right], \\ H_r &= -\frac{j}{\kappa^2} \left[ \beta \frac{\partial H_z}{\partial r} - \frac{\omega \varepsilon}{r} \frac{\partial E_z}{\partial \varphi} \right] \end{aligned} \quad (3.20)$$

where  $\kappa^2 = k_0 n_i^2 - \beta^2$ . At the boundary between the core and clad, the  $E_z$ ,  $H_z$ ,  $E_\varphi$ , and  $H_\varphi$  must be continuous. Using the boundary conditions and inserting  $E_z$  and  $H_z$  fields of Equations 3.18 and 3.19 into Equation 3.20, the results in a set of linear equations as given by:

$$\begin{bmatrix} J_v(\kappa a) & 0 & -K_v(\gamma a) & 0 \\ 0 & J_v(\kappa a) & 0 & -K(\gamma a) \\ \frac{\beta v}{a\kappa^2} J_v(\kappa a) & \frac{j\omega u_0}{\kappa} J'_v(\kappa a) & \frac{\beta v}{a\gamma^2} K_v(\gamma a) & \frac{j\omega u_0}{\gamma} K'_v(\gamma a) \\ \frac{j\omega \varepsilon_1}{\kappa} J'_v(\kappa a) & \frac{\beta v}{a\kappa^2} J_v(\kappa a) & -\frac{j\omega \varepsilon_2}{\gamma} K'_v(\gamma a) & \frac{\beta v}{a\gamma^2} K_v(\gamma a) \end{bmatrix} \begin{bmatrix} A \\ B \\ C \\ D \end{bmatrix} = 0, \quad (3.21)$$

Finding the determinate of the 4x4 matrix gives the following characteristic equation:

$$\left(\frac{\beta v}{a}\right)^2 \left[\frac{1}{\gamma^2} + \frac{1}{\kappa^2}\right]^2 = \left[\frac{J_v(\kappa a)}{\kappa J'_v(\kappa a)} + \frac{K'_v(\gamma a)}{\gamma K_v(\gamma a)}\right] \left[\frac{k_0^2 n_1^2 J'_v(\kappa a)}{\kappa J_v(\kappa a)} + \frac{k_0^2 n_2^2 K'_v(\gamma a)}{\gamma K_v(\gamma a)}\right] \quad (3.22)$$

If fields are weakly guided ( $\Delta n = (n_1 - n_2) \sim 0.005$ ), some of the modes will have a similar propagation constant  $\beta$ , and the characteristics equation can be simplified to the following:

$$\left(\frac{v}{a}\right)^2 \left[\frac{1}{\gamma^2} + \frac{1}{\kappa^2}\right] = \left[\frac{J_v(\kappa a)}{\kappa J'_v(\kappa a)} + \frac{K'_v(\gamma a)}{\gamma K_v(\gamma a)}\right] \quad (3.23)$$

The above result can further be simplified to produce one equation:

$$\kappa \frac{J_{j-1}(\kappa a)}{J_j(\kappa a)} = -\gamma \frac{K_{j-1}(\gamma a)}{K_j(\gamma a)} \quad (3.24)$$

Depending upon the j index value, various modes can be generated as given by:

$$\left( \begin{array}{l} j=1 \quad TE, TM \quad \text{modes} \\ j=v+1 \quad EH_v, \quad \text{modes} \\ j=v-1 \quad HE_v, \quad \text{modes} \end{array} \right) \quad (3.25)$$

where TE and TM are the Transverse Electric and Magnetic modes, respectively, and EH and HE are hybrid modes. The EH and HE modes have skewed propagation paths and the TE and TM propagate along the axis of the fiber. Since some of the modes described in Eq. 3.25 have nearly the same propagation constant, therefore nearly degenerate, they can be summed together to form series of linear polarized (LP) modes:

$$\begin{aligned} &LP_{1m}\text{-Sum of } TE_{0m}, TM_{0m}, \text{ and } HE_{2m} \\ &LP_{vm}\text{-Sum of } HE_{v+1,m}, \text{ and } EH_{v-1,m} \\ &LP_{0m}\text{-Sum of } HE_{1m} \text{ only} \end{aligned} \quad (3.26)$$

A LP mode is defined such that a linearly polarized field coupled into the optical fiber will remain linearly polarized by the sum of TE, TM, HE, and EH modes. Figure 3.3(a) shows the field and intensity distribute for  $LP_{01}$ ,  $LP_{11}$ , and  $LP_{21}$  modes. The normalized frequency number ( $V$ ) is inversely related to the wavelength, core diameter ( $a$ ), and differences in core/clad refractive index:

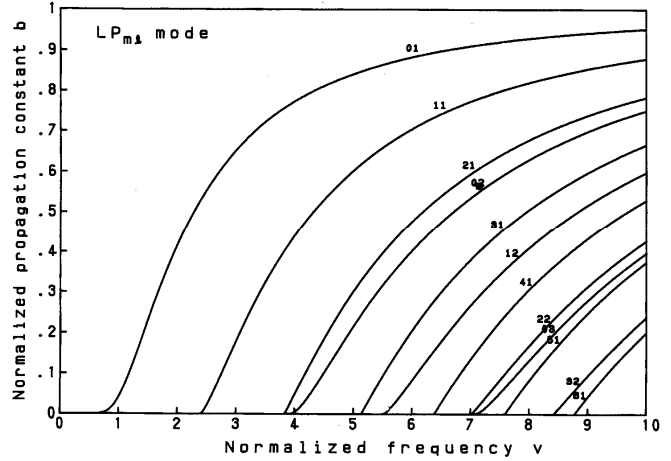
$$V = \frac{2\pi a}{\lambda} \sqrt{n_1^2 - n_2^2} \quad (3.27)$$

Figure 3.3(b) shows the normalized propagation constant versus the normalized frequency for LP modes, where the normalized propagation constant is given by:

$$b = \frac{\frac{\beta^2}{k_0^2} - n_2^2}{n_1^2 - n_2^2} \quad (3.28)$$

LP-mode designations	Traditional designations	Electric field distribution	Intensity distribution of $E_x$
LP <sub>01</sub>	HE <sub>11</sub>		
LP <sub>11</sub>	TE <sub>01</sub>		
	TM <sub>01</sub>		
	HE <sub>21</sub>		
LP <sub>21</sub>	EH <sub>11</sub>		
	HE <sub>31</sub>		

(a)



(b)

Figure 3.3 (a) Field and intensity distribution of linear polarization modes (LP<sub>vm</sub>). (b). Normalized propagation constant versus the normalized frequency (V) for LP modes (Okamoto 2000).

LP<sub>01</sub> (HE<sub>11</sub>) is the fundamental mode and has no cutoff, and can be approximated as a Gaussian beam:

$$E(r) = E_0 e^{-\left(\frac{r}{w}\right)^2} \tag{3.29}$$

The best fit between the Gaussian and Bessel function in the core is made by choosing a beam waist (w) of the following form:

$$w = a \left[ 0.65 + 1.619V^{-1.5} + 2.87V^{-6} \right] \tag{3.30}$$

At cutoff, the normalized frequency  $V$  is about 2.405, giving a beam waist of 1.1 times the core diameter, and 96 % overlap between the Bessel and Gaussian functions. In this research, the fiber is operating above cutoff wavelength and the  $HE_{11}$  mode will be the only mode propagating in the optical fiber. Plane wave propagation for the  $HE_{11}$  is further assumed; this will significantly simplify the simulation of fiber optic systems.

## 4. FIBER BRAGG GRATINGS

This chapter gives the theoretical overview of fiber Bragg gratings (FBG). The application of the couple mode theory will be discussed and the results applied towards uniform reflective type FBGs. The transfer matrix approach to simulated complex FBG structures is given. In the experimental section, a Boron-Germanium co-doped fiber will be fabricated using the phase mask technique and then characterized.

### 4.1. Couple Mode Theory

The couple mode theory describes the interaction between modes in a media with a perturbed refractive index (Kashyap 1999, Kostuk 2002). It can be used to compute the power diffracted by a fiber Bragg grating. Figure 4.1 shows a grating of length  $l$  with a periodically modulated refractive index of period  $\Lambda$ .

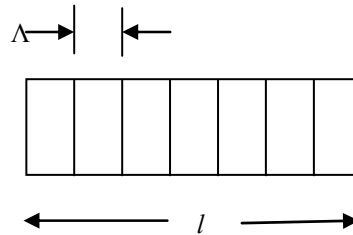


Figure 4.1 Grating structure

The permittivity of the grating is the summation of the unperturbed permittivity and the perturbed permittivity or:

$$\varepsilon(x, y, z) = \varepsilon(x, y) + \Delta\varepsilon(x, y, z) \quad (4.1)$$

The perturbation can occur in all three axes, however, for this work, the refractive index is modulated in the z-direction. The unperturbed permittivity  $\varepsilon(x,y)$  must satisfy the wave equation. Plugging the permittivity of the unperturbed waveguide,  $\varepsilon(x,y)$ , into the wave equation results in the following expansion of the wave equation:

$$\left( \frac{\partial^2}{\partial x^2} + \frac{\partial}{\partial y^2} + \omega^2 \mu_0 \varepsilon(x,y) - \beta_m^2 \right) E_m(x,y) = 0 \quad (4.2)$$

The resulting field in the perturbed waveguide can be expressed as a summation of the orthogonal modes of the unperturbed waveguide:

$$E(x,y,z) = \sum_m A_m(z) E_m(x,y) e^{-j\beta_m z}, \quad (4.3)$$

where  $\beta_m$  and  $A_m(z)$  are the propagation constant and amplitude of the transverse field component of mode  $m$  in the z-direction. Substituting this into the wave equation and eliminating the  $(x,y)$  dependence, and rearranging the terms results in the following:

$$\sum_k \left[ \frac{\partial^2 A_k}{\partial z^2} - j2\beta_k \frac{\partial A_k}{\partial z} \right] E_k(x,y) e^{-j\beta_k z} = -\omega^2 u_0 \sum_l \Delta \varepsilon(x,y) A_l E_l(x,y) e^{-j\beta_l z} \quad (4.4)$$

For small index modulation values, the power transfer between modes is small and the slow varying approximation can be used. The net effect is the elimination of the second order differentials (curvature) in Eq. 4.4. Using the orthogonal properties of the modes, multiplying both sides of the above equation by  $E_k^*$  and integrating over  $(x,y)$  results in the following:

$$-j\beta_k \frac{\partial A_k}{\partial z} \iint_{y,x} E_k(x,y) E_k^*(x,y) dx dy = -\omega^2 u_0 \sum_l A_l \iint_{y,x} E_k^* \Delta \varepsilon(x,y,z) E_l(x,y) e^{j(\beta_k - \beta_l)z} dx dy \quad (4.5)$$

The variation of the field of the  $k_{\text{th}}$  mode is then given by:

$$\frac{\partial A_k}{\partial z} = -j \frac{\beta_k}{|\beta_k|} \sum_l A_l C_{kl} e^{j(\beta_k - \beta_l)z} \quad (4.6)$$

Where  $C_{kl}$  is the coupling coefficient and describes the degree of coupling between the modes and is given by:

$$C_{kl} = \frac{\omega}{4} \iint_{y,x} E_k^* \Delta \varepsilon(x, y, z) E_l(x, y) dx dy \quad (4.7)$$

The coupling coefficient states that coupling occurs between different modes if the modulation index is asymmetric and coupling between similar modes only occurs in a symmetric modulation index. For the case of an optical fiber operating above cutoff, only the  $LP_{01}$  modes will couple, and the mode coupling equations of Eq. 4.6 reduces to two coupled equations. For the case of counter-propagating modes, where the two modes are propagation in the opposite direction, the mode coupling equations reduces to the following two coupled differential equations:

$$\begin{aligned} \frac{\partial A_1}{\partial z} &= -j C_{12} A_2 e^{j2\beta z} \\ \frac{\partial A_2}{\partial z} &= -j C_{21}^* A_1 e^{j2\beta z} \quad , \\ \beta &= \frac{2n}{\lambda} = \beta_1 = -\beta_2 \end{aligned} \quad (4.8)$$

## 4.2. Uniform fiber Bragg gratings

A uniform grating is defined as a grating with a uniform modulation index. For the case of the fiber Bragg grating, coupling only occurs between the  $LP_{01}$  modes. Assuming that the fiber Bragg grating has a sinusoidal modulation as given by Figure 4.2, the effective refractive index is the summation of the average refractive index and a sinusoidal modulation index,  $n_1$ :

$$n(z) = n + n_1 \cos(Kz) \quad (4.9)$$

$$\kappa = \frac{2\pi}{\Lambda}$$

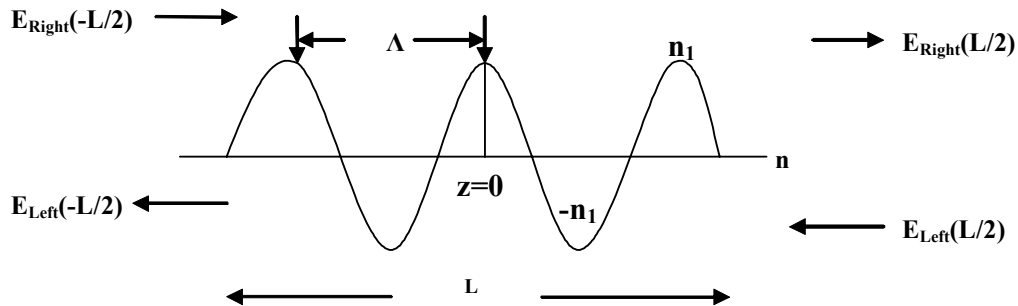


Figure 4.2 Sinusoidal variation of the refractive index

The task here is to determine the coupling coefficient and then use the couple mode equations to determine the reflectivity and transmittivity of the grating. The variation of the permittivity of the grating as a function of  $z$ -direction is the square of the change in the effective refraction index such that:

$$(n + n_1 \cos(\kappa z))^2 = \varepsilon_r + \Delta\varepsilon(z) \quad (4.10)$$

where  $\varepsilon_r$  is the permittivity constant of the unperturbed refractive index. The change in the permittivity is determined by expanding Eq. 4.10:

$$\varepsilon(z) = \left[ n^2 + 2nn_1 \cos(\kappa z) + n_1^2 \cos^2(\kappa z) \right] \varepsilon_0 \quad (4.11)$$

For a small change in refractive index modulation, the lower order terms can be ignored.

This gives the change in the permittivity:

$$\Delta\varepsilon(z) = 2nn_1 \cos(\kappa z) \varepsilon_0 \quad (4.12)$$

Plugging this result back into the coupling coefficient integral Eq. 4.7 and pulling outside non-integral dependent terms gives the coupling coefficient between the counter-propagation LP<sub>01</sub> modes:

$$\begin{aligned} C_{01^+01^-} &= \varepsilon_0 \frac{\omega}{2} nn_1 \cos(\kappa z) \iint_{y,x} E_{01^+}^*(x, y) E_{01^-}(x, y) dx dy \\ &= 2K_{ac} \cos(\kappa z) \end{aligned} \quad (4.13)$$

Where  $K_{ac}$  is the coupling constant and is directly related to index modulation magnitude and the fraction of power propagating within the core ( $\Gamma$ ):

$$K_{ac} = \frac{\pi n_1 \Gamma}{\lambda} \quad (4.14)$$

Restating the coupling equations from Eq. 4.8 by including the coupling coefficient gives the mode couple equations for a uniform grating:

$$\begin{aligned}
\frac{\partial A_1}{\partial z} &= -jK_{ac} A_2 e^{j\Delta\beta z} \\
\frac{\partial A_2}{\partial z} &= -jK_{ac} A_1 e^{-j\Delta\beta z} , \\
\Delta\beta &= 2\beta - \kappa
\end{aligned} \tag{4.15}$$

where the latter equation  $\Delta\beta$  is the phase matching condition. The coupling between the modes are maximized when the phase matching condition is meet or  $\Delta\beta=0$ . Restating Eq. 4.15 into a more convent form by plugging in the counter propagating sinusoidal fields  $E_{left}$  and  $E_{right}$ :

$$\begin{aligned}
\frac{\partial E_{Right}}{\partial z} + j\frac{1}{2}\Delta\beta E_{Right} &= -jK_{ac} E_{Left} \\
\frac{\partial E_{Left}}{\partial z} - j\frac{1}{2}\Delta\beta E_{Left} &= jK_{ac} E_{Right} \\
E_{Right} &= A_1 e^{-j\frac{1}{2}\Delta\beta z} \\
E_{Left} &= A_2 e^{j\frac{1}{2}\Delta\beta z}
\end{aligned} \tag{4.16}$$

Solving the coupling equations, gives the reflectance of the FBG:

$$\begin{aligned}
|\rho|^2 &= \left| \frac{E_{Left}(-L/2)}{E_{Right}(-L/2)} \right|^2 = \frac{K_{ac}^2 \sinh^2(\alpha L)}{K_{ac}^2 \cosh(\alpha L) - \gamma^2} \\
\gamma^2 &= \frac{1}{2}\Delta\beta \\
\alpha^2 &= K_{ac}^2 - \gamma^2
\end{aligned} \tag{4.17}$$

At the Bragg condition, the reflectivity reduces to tangent of the coupling coefficient:

$$|\rho|^2 = \tanh(\kappa_{ac} L) \tag{4.18}$$

The modulation in the refractive index can have an average dc bias and the change in permittivity can be restated in the following:

$$\Delta\varepsilon(z) = 2n\Delta n[1 + m \cos(\kappa z)]\varepsilon_0$$

where  $m\Delta n = n_1$

(4.19)

where  $m$  and  $\Delta n$  are the visibility and dc bias of the index modulation, respectively. The dc bias introduces a dc coupling coefficient similar to Eq. 4.14:

$$K_{dc} = \frac{4\pi\Gamma\Delta n}{\lambda}$$
(4.20)

The net result of dc coupling coefficient is a shift in the Bragg wavelength (Kostuk 2002):

$$\lambda_{\max} = \lambda_B \left( 1 + \frac{\Gamma\Delta n}{n} \right)$$
(4.21)

The bandwidth of the resulting Bragg spectrum depends on the modulation index. For  $(K_{ac}L)^2 \ll \pi^2$  or grating with a small index modulation, the wavelength bandwidth is given by the following:

$$2\Delta\lambda \approx \frac{\lambda^2}{nL}$$
(4.22)

For  $n_1 \gg \frac{\lambda_B}{L}$  or grating with high index modulation, the bandwidth is independent of the gradient length and is given by the following:

$$2\Delta\lambda \approx \frac{n_1}{n}$$
(4.23)

### 4.3. Transfer Matrix Method

Modeling gratings using the couple mode theory can be cumbersome if the modulation profile is complex. The transfer matrix method is available that can efficiently calculate the reflectivity and transmittivity of an arbitrary index modulation. The transfer matrix method is one method whereby the structure is segmented into smaller and simpler refractive index modulation profiles. The resultant characteristic of the complete grating structure is determined by simply multiply the transfer matrices and then imposing an overall boundary condition. The complex grating structure can be modeled as a four port system with inputs and outputs. The input and output of the system can be represented through a transfer function T (Kashyap 1999):

$$\begin{bmatrix} E_{Right}(-L/2) \\ E_{Left}(-L/2) \end{bmatrix} = [T] \begin{bmatrix} E_{Right}(L/2) \\ E_{Left}(L/2) \end{bmatrix} \quad (4.24)$$

Assuming no input to the system from  $E_{Left}(L/2)$  of the grating and a normalized input into the system from the left, the system than can be represented by:

$$\begin{bmatrix} 1 \\ E_{Left}(-L/2) \end{bmatrix} = \begin{bmatrix} T_{11} & T_{12} \\ T_{21} & T_{22} \end{bmatrix} \begin{bmatrix} E_{Right}(L/2) \\ 0 \end{bmatrix} \quad (4.25)$$

The solutions to the above equation are given by:

$$\begin{aligned} E_{Right}(L/2) &= \frac{1}{T_{11}} \\ E_{Left}(-L/2) &= \rho = \frac{T_{21}}{T_{11}} \end{aligned} \quad (4.26)$$

Since the input is normalized,  $E_{Right}(L/2)$  and  $E_{Left}(-L/2)$  are also the transmittivity and reflectivity of the grating, respectively. If a grating structure of length L is divided into N

segments as shown in Figure 4.3, the system can be represented as a multiplication of individual transfer functions:

$$\begin{bmatrix} E_{Right}(-L/2) \\ E_{Left}(-L/2) \end{bmatrix} = [T^N [T^{N-1} \dots [T^3 [T^2 [T^1 \begin{bmatrix} E_{Right}(L/2) \\ E_{Left}(L/2) \end{bmatrix}]]]] \quad (4.27)$$

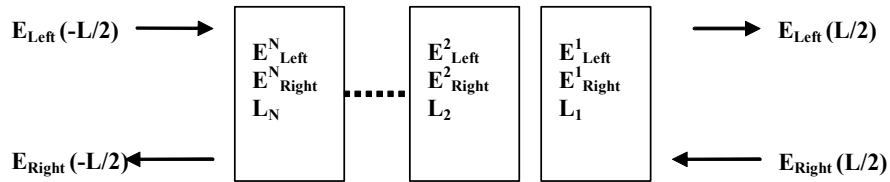


Figure 4.3 Division of complex grating structure into N simple grating structures

If each section is a simple uniform reflective type grating of length  $l_i$ , the transfer function can be determined by the solution of the couple mode theory (Kashyap 1999):

$$\begin{aligned} T_{11} &= \cosh(\alpha \delta l_i) - \frac{j \delta_c \sinh(\alpha \delta l_i)}{\alpha} \\ T_{22} &= \cosh(\alpha \delta l_i) + \frac{j \delta_c \sinh(\alpha \delta l_i)}{\alpha} \\ T_{12} &= \frac{j K_{ac} \sinh(\alpha l_i)}{\alpha} \\ T_{21} &= \frac{-j K_{ac} \sinh(\alpha l_i)}{\alpha} \end{aligned} \quad (4.28)$$

#### 4.4. Fabrication methods

It turns out that germanium doped optical fiber is sensitive to ultraviolet (UV) light, resulting in increase of the refractive index. This effect was observed by Hill, et al. (1978) during their experimentations with optical communication systems. It was

observed that when Argon ion laser was used as a source, back reflection from optical fiber were observed and increased as a function of time. It was later determined to be a result of a standing wave created by the back reflection from the tip of the fiber and the forward propagating light. This standing wave created an interference pattern within the length of the fiber which in term resulted in the modulation of the refractive index of the Germanium doped core. This effect was magnified when the Germanium content of the core increased and a UV source was used. There are many theories on the photosensitivity process of Germanium content glass; however, the exact nature is not known (Kashyap 1999). The main common area among the theories is that UV reduces the defects due to the Germanium oxides (due to incomplete manufacturing process), resulting in increase of the density of the material and its refractive index (Kashyap 1999).

Fiber Bragg gratings can be fabricated using two main fabrication techniques: Holographic or using the Phase Masking technique. The holographic technique (cf. Figure 4.4) uses the two beam interference method. A UV laser source is split into two beams and then interfered along the length of the optical fiber. The inference between the beams creates an interference (grating) pattern along the length of the optical fiber. This will then imprint the grating profile into the germanium doped core of the optical fiber. Depending on the angle of incidences, the grating period can be varied, thus changing the operating points of the grating.

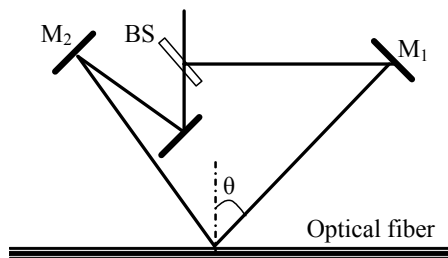


Figure 4.4 Holographic two beam interference method

The phase mask technique uses a silicate glass substrate with etched grating profile (cf. Figure 4.5). In addition, the phase mask can be fabricated using holographic methods. An incident UV laser source is split into the zero and the first orders. The zero order is usually blocked or designed out of the phase mask. The first orders interfere to create an interference pattern along the fiber. Depending on the angle of incidence of the first orders, the period of the grating can be varied similar to the holographic technique (Kashyap 1999, Battiato 1998).

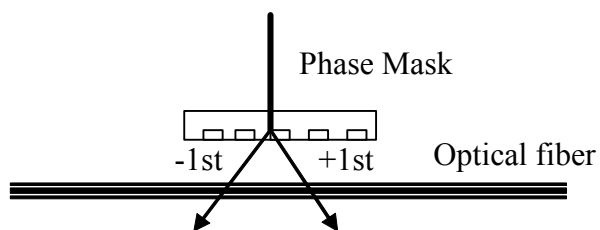


Figure 4.5 Phase mask technique

The advantages of the phase mask technique are its stability, ease of alignment, and relaxed coherence requirements when compared to the holographic technique. In addition, the phase mask can be used to mass produce gratings. However, the gratings

can only operate at single wavelength, although, there are ways to vary the wavelength by steering the  $\pm 1$  orders using mirrors. In the holographic technique, the operating wavelength can be varied by adjusting the angle of incidence.

#### 4.5. Boron/Germanium co-doped fibers

The optical fibers used in this research are a single mode SMF28 standard optical fiber and a single mode Boron/Germanium co-doped fiber. It is known that adding Boron to silicate glass (cladding) reduces the overall index of the glass (Kashyap 1999). The numerical aperture for an optical fiber is directly related to the index difference between the core and the cladding:

$$NA = \sqrt{n_1^2 - n_2^2} \quad (4.29)$$

Since the change in the index of refraction is directly related to the concentration of Germanium, adding Boron will allow greater concentration of Germanium in the core of the optical fiber while maintaining the index difference between the core and cladding region, thus maintaining the NA. The advantage of a Boron/Germanium co-doped fiber is its higher photosensitivity, shorter writing time, and its ability to be compatible with standard optical fiber and low NA fiber amplifiers (since the NA can be controlled).

#### 4.6. Grating equation and Bragg diagram

The grating equation can be used to determine the angle of diffraction for field on a grating or periodic structure (Kashyap 1999, Battiato 1998):

$$n \sin \theta_2 = n \sin \theta_1 + \frac{m\lambda}{\Lambda} \quad , \quad (4.30)$$

where  $n$ ,  $\theta_1$ ,  $\theta_2$ ,  $m$ , and  $\Lambda$  are the effective refractive index, incident angle, angle of refraction, order of diffraction, and the grating period, respectively. The grating equation describes the phase matching condition. When the angle of diffraction equals the angle of incident, the phase matching condition is satisfied and maximum coupling occurs between the incident and diffracted beam. For the case of the reflective fiber Bragg grating, the incident and diffracted field are counter-propagating in the optical fiber, where the effective refractive index are given by  $n_1 = n \sin \theta_1$  and  $n_2 = n \sin \theta_2$ ; the propagation constants are then given by  $\beta_1 = kn_1$  and  $\beta_2 = kn_2$ . Plugging into Eq 4.30 results:

$$\beta_2 = \beta_1 + \frac{2\pi m}{\Lambda} \quad (4.31)$$

Where  $\beta_1 = -\beta_2 = \beta$  for counter propagation fields and  $n_1 = n_2$  for single mode optical fiber. Re-arrange Eq 4.31 for the first orders results in the required periodicity to satisfy the Bragg condition for the first order:

$$\Lambda = \frac{2\pi}{2\beta} = \frac{\lambda_B}{2n} \quad (4.32)$$

Figure 4.6 shows the graphical technique to achieve the same results as above. Adding the propagation vectors for the field in the fiber:

$$\bar{\beta}_1 - \bar{\beta}_2 = \bar{K} \quad (4.33)$$

Since the vectors above are in the same axis, direct addition can be done.

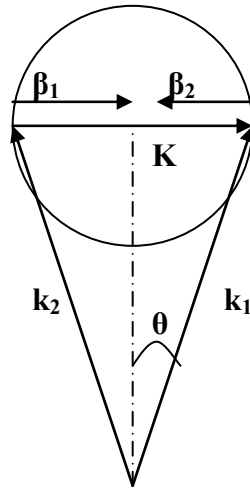


Figure 4.6 Bragg diagram

In the phase mask or holographic technique, two beams are interfered to create the grating profile in the optical fiber. If the writing wavelength is  $\lambda_{UV}$ , the grating vector  $\mathbf{K}$  is given by:

$$\bar{k}_1 - \bar{k}_2 = \bar{K} \quad (4.34)$$

Or

$$\begin{aligned} \bar{K} &= k(\hat{x} \sin \theta + \hat{y} \cos \theta + \hat{x} \sin \theta - \hat{y} \cos \theta) \\ &= 2k\hat{x} \sin \theta \end{aligned}$$

Reducing the above equation to the following format shows the required angle between the interfering beams to create a fringe pattern with periodicity  $\Lambda$ :

$$\theta = \sin^{-1} \left( \frac{K}{2k} \right) = \sin^{-1} \left( \frac{\lambda_{UV}}{2n\Lambda} \right) \quad (4.35)$$

#### 4.7. Experiment

An experiment shown in Figure 4.7 was setup to fabricate FBGs and FBGAs. The FBGs used in this research were inscribed using the phase mask technique. The period of the phase mask is 1072 nm. A Boron/Germanium co-doped photosensitive fiber, F-SBG-15 from Newport Corp operating at 1550 nm was used. The photosensitive fiber was used because laser power was then only 12 mW from a frequency doubled continuous-wave Argon ion laser operating at 244 nm (UV). About 2 cm of the coating was stripped and the optical fiber was then clamped between two fiber holders. The fiber holders were attached on top of two posts. A dummy weight was used to pre-tension the fiber. This was done in order to maintain uniform center wavelength of the FBGs. The phase grating exposed 1.3 cm of the optical fiber and placed as close to the optical fiber. One end of the optical fiber was fusion spliced to a length of SMF28 fiber. The optical fiber was source by an EDFA (Erbium Doped Fiber Amplifier) source and the resulting reflectance observed on an optical spectrum analyzer (OSA).

Initially, the fiber was cleaved and the resulting 4% Fresnel reflection of the tip was used as a reference point on the OSA. The cleaved tip was then broken off. The UV source was then turned on and the resulting reflectance in dB was recorded. The reflectance of the FBG was determined using the following:

$$dB_{Grating} = dB_{Total} - 14dB + 1.28dB \quad (4.36)$$

Where  $dB_{total}$ , -14dB, 1.28dB are the total reflectance, Fresnel reflectance, and splice loss between the photosensitive fiber and SMF28 fiber, respectively. The reflectance is then given by:

$$|\rho|^2 = 10^{\frac{dB_{Grating}}{10}} \quad (4.37)$$

The peak grating reflectance equation Eq. 4.18 and the measured reflectance of Eq. 4.37 were then used to determine the modulation. The average change in the index was determined with the aid of Eq. 4.21. Figure 4.7(a) shows the modulation index as a function of exposure time and Figure 4.8(b) shows the resulting shift in the Bragg wavelength. The final reflectance of the FBG fabricated is 90% and with a bandwidth of 200 pm and centered at 1551.2 nm.

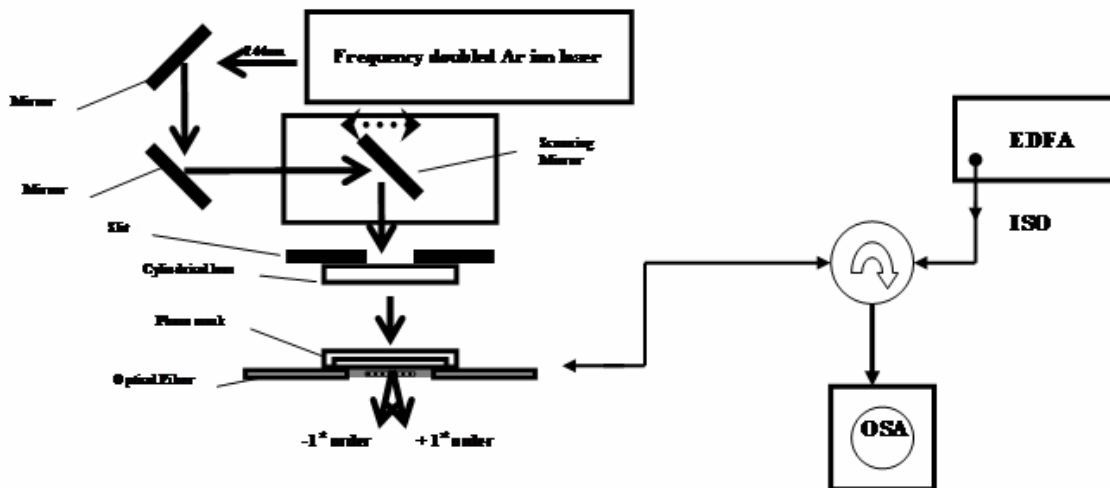


Figure 4.7 FBG fabrication using a double frequency Argon laser and phase mask

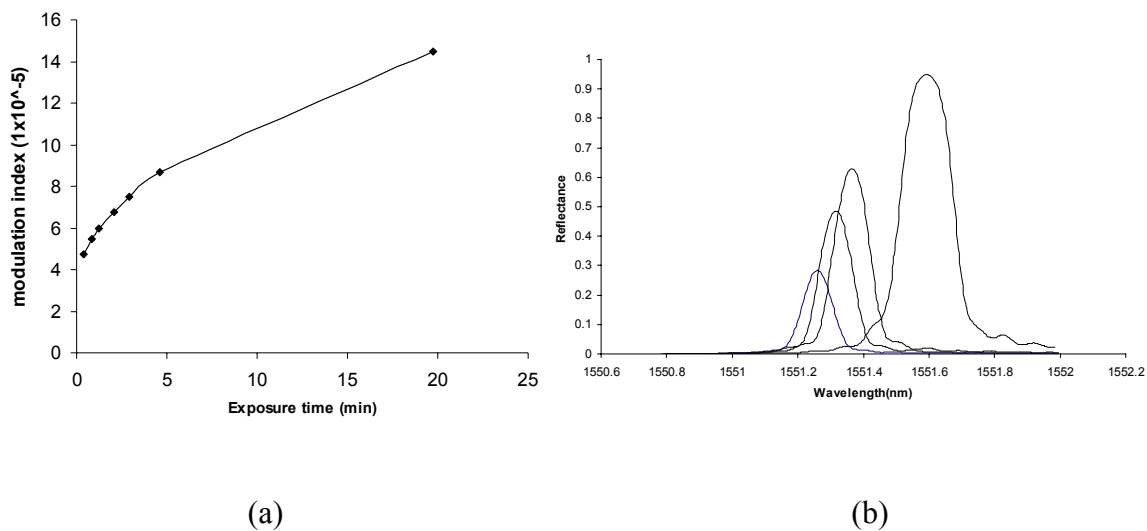


Figure 4.8 (a) Change in the modulation index as a function of the exposure time. (b). Reflectance spectrum of the FBG

From Figure 4.8, assuming that the fraction of power remaining in the core is 0.8, the average refractive index is about  $4 \times 10^{-4}$  and the modulation index is about  $1.5 \times 10^{-4}$ , giving a visibility of 0.37. You can see that the Boron-Germanium co-doped gives a large change in refractive index given the 12mW power source. For a standard optical fiber, typically 1% change in reflectance can be achieved with a 100 mW UV power source. To get higher values, hydrogen loading is required (Kashyap 1999). The FBG fabricated in this experiment was used in photoelasticity experiments later to be shown in Chapter 8.

## 5. INTERFEROMETRY

This chapter describes two beam and multi-beam interferometers. The theoretical background for each case will be given. Coherence properties of two beam interferometers will also be given. The results will then be applied towards a fiber optic Fabry-Perot displacement sensor, a component of the FPI strain gauge calibrator, later to be shown in Chapter 8.

### 5.1. Two beam interferometer

The Michelson interferometer is a two beam interferometer. Figure 5.1 shows the layout for the Michelson green interferometer. Traditionally, a Michelson operating at a single wavelength is called a Twyman-Green interferometer. Throughout this work, however, the word Michelson will be used.

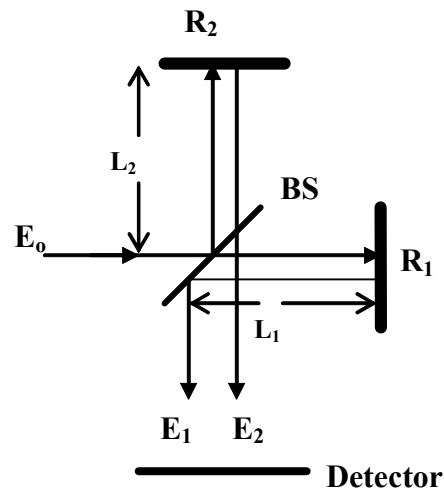


Figure 5.1 Michelson interferometer

The basic components are two reflectors,  $R_1$  and  $R_2$ , and beam splitter. An incident field of the form:

$$E_o(x_i) = E_o e^{j(kx_i)} \quad (5.1)$$

is split by the beam splitter and reflects off  $R_1$  and  $R_2$ . The temporal contribution is implied in Eq. 5.1. The fields at the detector are then given by:

$$\begin{aligned} E_1(x_1) &= E_1 e^{j(kx_1)} \\ E_2(x_2) &= E_2 e^{j(kx_2)}. \end{aligned} \quad (5.2)$$

The resultant field is given by the sum of  $E_1$  and  $E_2$ :

$$E = E_1 + E_2 \quad (5.3)$$

The detector will measure the irradiance or the square of  $E$ :

$$I = |E_1 + E_2|^2 = (E_1 + E_2)(\bar{E}_1 + \bar{E}_2) \quad (5.4)$$

Expanding:

$$\begin{aligned} I &= |E_1 + E_2|^2 \\ &= (E_1 e^{jkx_1} + E_2 e^{jkx_2})(\bar{E}_1 e^{-jkx_1} + \bar{E}_2 e^{-jkx_2}) \\ &= E_1 \bar{E}_1 + E_2 \bar{E}_2 + E_1 \bar{E}_2 e^{jk(x_1-x_2)} + \bar{E}_1 E_2 e^{-jk(x_1-x_2)} \\ &= I_1 + I_2 + 2\sqrt{I_1 I_2} \cos \phi \end{aligned} \quad (5.5)$$

where

$$\phi = k(x_1 - x_2) = 2k(L_1 - L_2). \quad (5.6)$$

Eq. 5.6 is the phase difference due to the path difference between the positions of the reflectors. The Michelson is a double pass interferometer, so  $2(L_1-L_2)$  is the optical path difference between the positions of the reflectors. The visibility of the signal is given by ratio between the AC and DC components of the irradiance signal:

$$v = \frac{AC}{DC} = \frac{2\sqrt{I_1 I_2}}{I_1 + I_2} \quad (5.7)$$

Visibility is an important parameter that can be used to determine the contrast of the signal. A small peak-peak magnitude and a large DC value will make it hard to process the signal. A large peak-peak magnitude and a small DC value will make the signal more pronounced. The visibility is maximum when irradiance  $I_1=I_2$ . If the beam splitter is 50/50 split between the two paths and  $R=R_1=R_2$  then:

$$I_1 = I_2 = \frac{I_o}{4} R \quad (5.8)$$

where  $I_i$  is the intensity of the incident beam. Re-writing Eq. 5.5:

$$I = \frac{I_0}{2} R(1 + \cos \phi) \quad (5.9)$$

## 5.2. Multi-beam interferometer

An Interferometer with more two interferences is called a multi-beam interferometer. Figure 5.2 shows a Fabry-Perot interferometer. The basic components are two semi-reflective reflectors spaced by distance  $L$ .

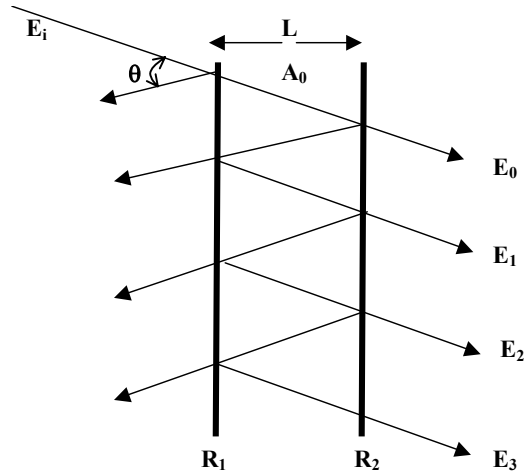


Figure 5.2 Fabry-Perot interferometer

Multiple reflections will occur between the reflective surfaces. The resulting reflectance and transmittance can be determined using traditional method by summing the reflections or can be determined directly using transfer matrix approach such that (Kashyap 1999):

$$M = \frac{1}{\sqrt{1-R_2}} \begin{bmatrix} 1 & \sqrt{R_2} \\ \sqrt{R_2} & 1 \end{bmatrix} \exp \begin{bmatrix} -j\phi_0 & 0 \\ 0 & j\phi_0 \end{bmatrix} \frac{1}{\sqrt{1-R_1}} \begin{bmatrix} 1 & \sqrt{R_1} \\ \sqrt{R_1} & 1 \end{bmatrix}, \quad (5.10)$$

where the round trip is given by  $\phi_0 = \frac{4\pi}{\lambda} L \cos \theta$ . A similar approach can be used for

Michelson. The reflectance of the FPI is then given directly by the M-matrix (Kashyap 1999):

$$R = \left| \frac{M_{11}}{M_{21}} \right|^2$$

or

$$R = \frac{R_1 + R_2 - 2\sqrt{R_1 R_2} \cos \phi_0}{1 + R_1 R_2 - 2\sqrt{R_1 R_2} \cos \phi_0} \quad (5.11)$$

The finesse of the FPI is the ratio between the fringe spacing and a width of a fringe at FWHM (full width half maximum). Assuming no losses in the cavity, the finesse is given by:

$$finesse = \frac{\pi\sqrt{R_1 R_2}}{1 - R_1 R_2} \quad (5.12)$$

If the angle of incidence is 0 degrees, then peak the peak of a fringe will occur ever  $2\pi$ :

$$\phi_0 = 2kL = 2\pi m \quad (5.13)$$

where m is the mode order. Solving for L gives the required change in the cavity spacing to produce a maximum fringe:

$$L = \frac{\lambda}{2} m \quad (5.14)$$

The free spectral range (separation between the modes) is given by:

$$\delta\lambda = \frac{\lambda^2}{2L} \quad (5.15)$$

Figure 5.3 shows the fringe pattern as a function finesse (F for short) and wavelength, assuming  $R_1=R_2$  and with a 1 cm cavity spacing. As can be seen in the figure, at low finesse (INVD in the figure for invalid since finesse is invalid for values less than 1), the Fabry-Perot interferometer is similar to a two beam interferometer. The reflectance of the FPI at low finesse is given by:

$$R = 2R_1(1 - \cos \phi) \quad (5.16)$$

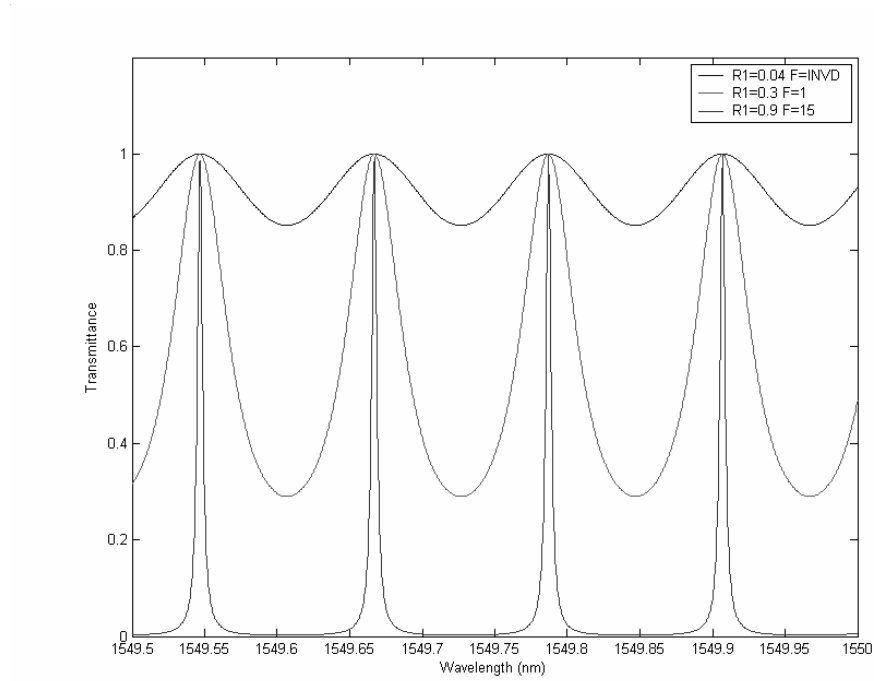


Figure 5.3 Transmittance spectrums for 1cm FPI as a function of mirror reflectance and finesse.

### 5.3. Temporal Coherence

Interferences due to multiple source or polychromatic sources results in the reduction of the fringe contrast. The fringe contrast is directly related to the temporal coherence of the source, where temporal coherence is the ability of a field in maintaining its phase continuity, without any disruptions or discontinuity, during a period time. For the case of the two beam interferometer with a polychromatic source, the total power observed at a detector as a function of optical path difference (OPD) is given by (Milster 2002):

$$\begin{aligned}
I(OPD) &= \int \left[ a^2(v)(R_1 + R_2) + 2\sqrt{R_1 R_2} a^2(v) \cos\left(2\pi v \frac{OPD}{c}\right) \right] dv \\
&= (R_1 + R_2)I_0 + 2\sqrt{R_1 R_2} I_0 \frac{\operatorname{Re}\left\{ \int \left( a^2(v) e^{j2\pi v \frac{OPD}{c}} \right) dv \right\}}{I_0}
\end{aligned} \tag{5.17}$$

where  $a^2(v)$  and  $c$  are the power spectrum density of the source and speed of light, respectively. The power spectrum density shows the distribution of the power of the optical field in the frequency domain. The first component of Eq. 5.17 is constant and the second component is a function of the Fourier transform of the power spectrum. This can be shown to be a function of coherence factor magnitude  $m_{12}$  and phase  $\varphi$ :

$$I(OPD) = (R_1 + R_2)I_0 + 2\sqrt{R_1 R_2} I_0 m_{12} \left( \frac{OPD}{c} \right) \cos \phi \left( \frac{OPD}{c} \right) \tag{5.18}$$

Where  $m_{12} \left( \frac{OPD}{c} \right)$  and  $phase \left( \frac{OPD}{c} \right)$  are given by:

$$\begin{aligned}
m_{12} \left( \frac{OPD}{c} \right) &= \left| \frac{\operatorname{Re}\left\{ \int \left( a^2(v) e^{j2\pi v \frac{OPD}{c}} \right) dv \right\}}{I_0} \right| = \left| \frac{F[a^2(v)]_{\frac{OPD}{c}}}{I_0} \right|, \\
\varphi_{12} \left( \frac{OPD}{c} \right) &= phase \left( F[a^2(v)]_{\frac{OPD}{c}} \right)
\end{aligned} \tag{5.19}$$

where  $F$  is the Fourier transform and  $m_{12}$  describes the degree of coherence. Note that  $m_{12}$  can also be considered an autocorrelation function since the interference is due to a delayed version of the source field (Yu, et al. 2004). In addition, the Fourier transform of an autocorrelation function gives the point spread function (PSF), in this case, the power spectrum density  $a^2(v)$ . This concept is applied for the case of an electric signal from a

detector in Chapter 9. To recover the power spectrum density all that is required is the Fourier transform of the coherence function. The fringe contrast is directly related to the coherence factor such that:

$$v = \frac{AC}{DC} = \frac{2\sqrt{R_1 R_2}}{R_1 + R_2} m_{12} \left( \frac{OPD}{c} \right) \quad (5.20)$$

The temporal coherence time is one over the linewidth ( $1/w$ ) of the source, in which case, the coherence length is given by:

$$L_c = \frac{c}{w} \quad (5.21)$$

From Eq. 5.19, the Fourier transform of a Gaussian power source with a linewidth of 150kHz (spectral width of the source at FWHM) is another Gaussian function with a temporal coherence time width of  $1/150\text{kHz}$ , where the coherence length is roughly 2000 meters using Eq. 5.21. This coherence length is achieved by the tunable laser source used in this work.

#### 5.4. Fiber optic Fabry-Perot displacement sensor

In this research, a fiber optic FPI was used as a displacement and strain measurement device as shown in Figure 5.4.  $R_1$  is the reflectance from the front end of a cleaved single mode optical fiber and  $R_2$  is the reflectance from a position that is adjustable. In this section,  $R_1$  and  $R_2$  will also be used to label the reflecting surfaces.

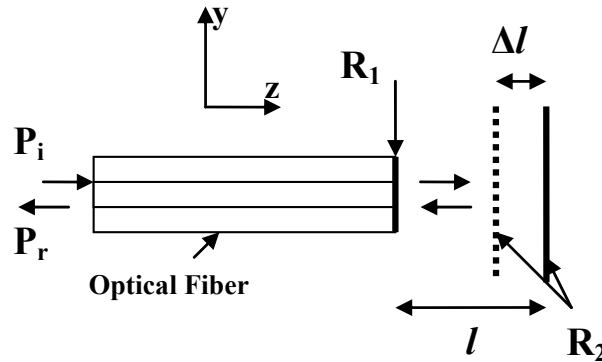


Figure 5.4 Fiber optic Fabry-Perot interferometric displacement sensor.

One end of a test sensor is attached to surface  $R_2$  and the other end of the test sensor is kept fixed. The optical field reflects from both end faces and interferes; assuming the cavity is filled with air, the round trip phase is given by:

$$\phi = \frac{4\pi(l - \Delta l)}{\lambda} = kz_0, \quad (5.22)$$

where  $l$ ,  $\Delta l$ ,  $z_0$ , and  $k = \frac{2\pi}{\lambda}$  are the nominal cavity length, cavity displacement, round trip path length, and the propagation constant, respectively. Interference fringes are produced at the output of the FPI as the position of surface  $R_2$  varies, and the distance between the fringes is  $\lambda/2$ . The resulting displacement is then given by:

$$\Delta l = N \frac{\lambda}{2}, \quad (5.23)$$

where  $N$  is the corresponding number of observed fringes, respectively.

The objectives in this section are to taken into account diffraction effects from surface  $R_1$ , determine the reflectance of the FPI, and determine the optimum nominal cavity

length. For the case of a weakly guided single mode optical fiber operating above the cutoff wavelength, only the fundamental LP<sub>01</sub> mode propagates in the optical fiber. The LP<sub>01</sub> can be approximated as a scalar Gaussian field; the normalized scalar field at surface R<sub>1</sub> is then given by:

$$f_1(x, y) = \sqrt{\frac{2}{\pi}} \cdot \frac{1}{w_0} e^{-\frac{x^2+y^2}{w_0^2}} \quad (5.24)$$

where  $w_0$  is the mode field or beam waist radius of the LP<sub>01</sub> mode and  $\int_{-\infty}^{\infty} |f(x)|^2 dx = 1$ .

The Gaussian field approximation also takes into account the decaying field in the cladding region of the fiber. To determine the diffracted field at distance  $z_0$ , the Gaussian field of Eq. 5.24 is first broken down into its constituent plane wave components; the weighting function of the plane waves is the Fourier transform of Eq. 5.24. Each plane wave is then independently propagated and then re-summed to get the resultant field at  $z_0$ .

The normalized field at  $z_0$  is then given by (Ghatak 1998):

$$f_2(x, y, z_0) = \sqrt{\frac{2}{\pi}} \frac{1}{w_0} \frac{ikw_0^2}{2z_0 + ikw_0^2} e^{-ik\frac{(x^2+y^2)}{2R(z_0)}} e^{-\frac{x^2+y^2}{w(z_0)^2}} e^{-ikz_0}, \quad (5.25)$$

where  $R(z)$  and  $w(z)$  are the radius of curvature and the beam waist radius of the Gaussian field at distance  $z_0$ , respectively:

$$R(z_0) = z_0 \left( 1 + \frac{\pi^2 w^4}{\lambda^2 z_0^2} \right)$$

$$w(z_0) = w_0 \left( 1 + \frac{\lambda^2 z_0^2}{\pi^2 w_0^4} \right)^{\frac{1}{2}} \quad (5.26)$$

Eq. 5.25 and 5.26 are valid for the near and far field. Assuming only longitudinal misalignment between surface  $R_1$  and surface  $R_2$ , the field  $f_2(x,y,z_0)$  incident on surface  $R_1$  will excite a  $LP_{01}$  mode in the optical fiber with coupling coefficient or transmittance given by the overlap integral:

$$T(z_0) = \left| \int_{-\infty}^{\infty} \int_{-\infty}^{\infty} f_1(x,y) f_2(x,y,z_0) dx dy \right|^2 \quad (5.27)$$

$$= \left( 1 + \frac{z_0^2 \lambda^2}{4\pi^2 w_0^4} \right)^{-1}$$

In this work, a single mode SMF 28 step index optical fiber with a mode field radius of 5.2  $\mu\text{m}$  at 1550 nm was used. The operating wavelength is 1550 nm; the tip of the optical fiber was cleaved giving a Fresnel reflectance of 4%; the material of surface  $R_2$  is aluminum with 70% reflectance at 1550 nm. Figure 5.5 shows the plot of the transmittance function as a function of the cavity length. As shown in the Figure 5.5, the transmittance drops below 6% for cavity lengths longer than 250  $\mu\text{m}$ . Since the reflectance of  $R_1$  and the transmittance are below 10%, the two beam interference method can be used to approximate the resultant field just right of the surface  $R_1$ . The resultant field is the sum of the field reflecting from surface  $R_1$  and field contribution from surface  $R_2$ . The field from the first reflection off surface  $R_1$ ,  $E_1(x,y)$ , and the field contribution from surface  $R_2$ ,  $E_2(x,y,z_0)$ , are given by (Vries, et al. 1995):

$$E_1(x,y) = \sqrt{R_1} f(x,y) \quad (5.28)$$

$$E_2(x,y,z_0) = (1 - R_1) \sqrt{R_2 T(z_0)} f(x,y) e^{-ikz_0}$$

The reflectance of the FPI displacement sensor is then given by:

$$\begin{aligned} \frac{P_r(z_0)}{P_i} &\approx \int_{-\infty-\infty}^{\infty} \int_{-\infty-\infty}^{\infty} |E_1(x, y) + E_2(x, y, z_0)|^2 dx dy \\ &= R_1 + (1 - R_1)^2 R_2 T(z_0) + 2\sqrt{R_1 R_2 T(z_0)}(1 - R_1)\cos(kz_0) \end{aligned} \quad (5.29)$$

The contrast of the FPI signal is then given by:

$$v(z_0) = \frac{2\sqrt{R_1 R_2 T(z_0)}(1 - R_1)}{R_1 + (1 - R_1)^2 R_2 T(z_0)} \quad (5.30)$$

Figure 5.5 also shows the contrast of the fringes as a function of the cavity length. Contrast is 100% at 250  $\mu\text{m}$  cavity length; at this position, the field contribution from surface  $R_2$  matches the field contribution from surface  $R_1$ . Ideally, 250  $\mu\text{m}$  is the optimum cavity length for the parameters given because the fringes will be most pronounced and their magnitude will essentially remain constant.

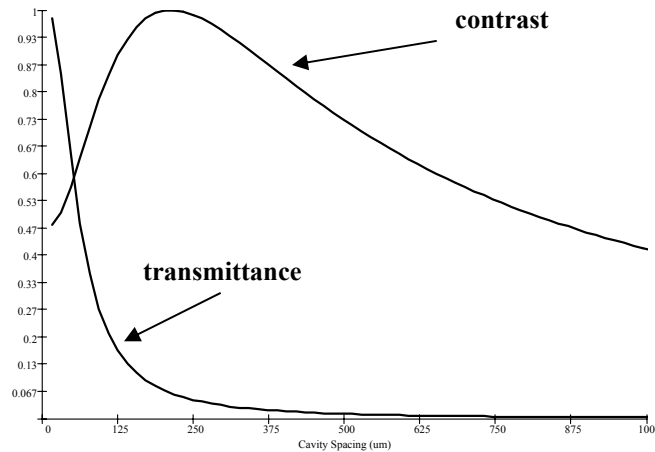


Figure 5.5 Transmittance and visibility curves for the fiber optic Fabry-Perot displacement sensor as a function of the cavity spacing.

However, the exact optimum cavity length will depend on the quality of the reflecting surfaces, scattering effects, and surface alignments. The important result of this section is that there is an optimum cavity length to maximize the contrast.

## 6. POLARIZATION

This chapter discusses the concept of polarization. The mathematical foundation of polarization will be given along with the methods of analysis. The results will be used in Chapter 11 for FBGA/C-OFDR cavity suppression.

### 6.1. Physical description

An optical field has a direction in which the electric field is aligned; this direction of the electric field is termed the polarization direction (state) of the optical field. The polarization of the electric field can be broken into two orthogonal directions, in this case, along the x and y axis:

$$\bar{E} = E_x \hat{x} + E_y e^{i\delta} \hat{y} \quad (6.1)$$

Where  $E_x$ ,  $E_y$ , and  $\delta$  are the magnitude of the electric field along the x and y axis, and the relative phase difference of the electric fields along the two orthogonal directions, respectively. Depending on the relative phase difference, the electric field can have linear, elliptical, and circulate polarization. Figure 6.1 shows the polarization state when the phase difference goes through a single revolution. As shown, a linear polarization is realized when the phase difference is a multiple of  $\pi$ . This means that the tip of the electric field will remain at a fixed angle as the field propagates. Circular polarization will result when the phase difference is exactly a multiple of  $\pi/2$  or 90 degrees. For a circular polarization, the tip of the electric field will rotate in a circular (i.e. fixed radius) pattern as function of time or space. When the field rotates clockwise as function of

position, left handed polarization (LH) will result and right handed other wise (RH). Any other phase difference not mentioned will result in an elliptical pattern.

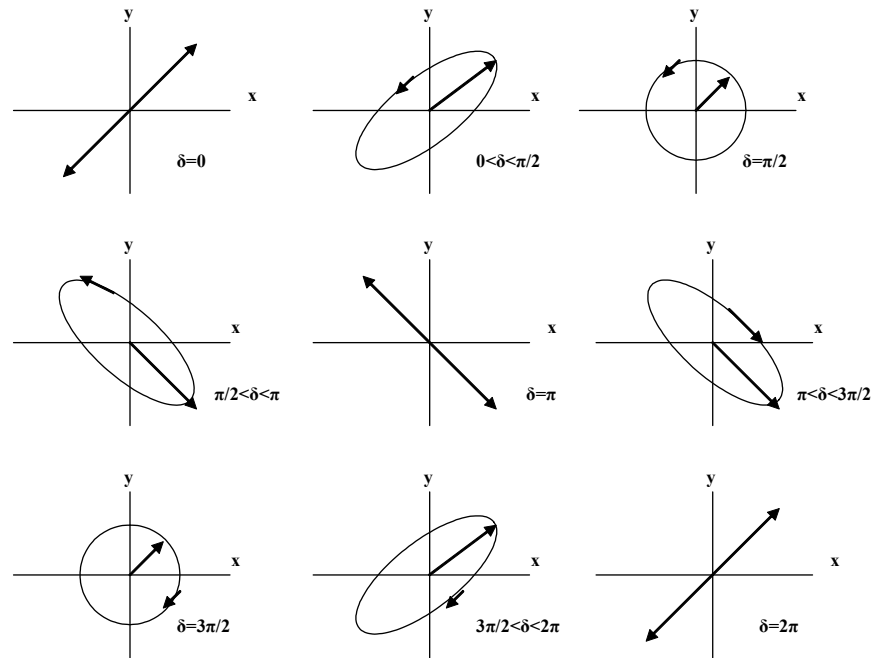


Figure 6.1 Polarization state of a field as the phase difference goes through a single revolution.

## 6.2. Measurement of polarization

Detectors measure irradiance as opposed to the electric fields directly. Muller calculus can be used to completely describe the state of polarization using the irradiance. Four components makeup Muller calculus called the Stokes vectors are (Yu, et al. 2002, Milster 2003):

$$\begin{aligned}
 s_0 &= A_x^2 + A_y^2 \\
 s_1 &= A_x^2 - A_y^2 \\
 s_2 &= 2A_x A_y \cos \delta \\
 s_3 &= 2A_x A_y \sin \delta
 \end{aligned}
 \tag{6.2}$$

Physically,  $s_0$  represent the total irradiance of the field;  $s_1$  is the difference in irradiance between vertical and horizontal polarizations;  $s_2$  is the difference in irradiance between 45 and 270 degrees of the linear polarizer; and  $s_3$  is the difference in irradiance between the right and left handed circular polarization. All the Stokes vector components can be measured by using a quarter-wave plate and a linear polarizer as shown in Figure 6.2.

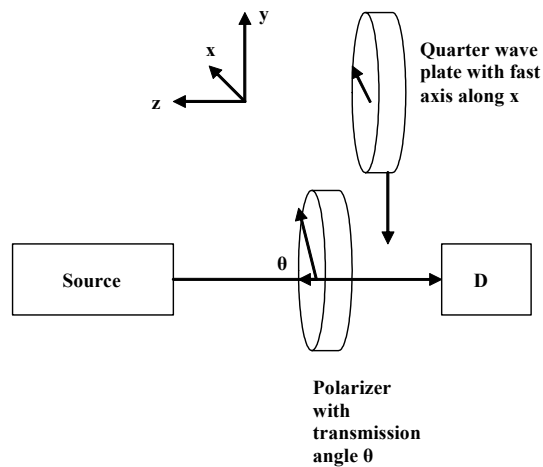


Figure 6.2 Measurements of the Stokes components using a polarizer with transmission along the x-axis and quarter-wave plate with fast axis along the x-axis.

The Stokes vector components are then given directly from the irradiance measurements:

$$\begin{aligned}
 s_0 &= I_1 + I_2 \\
 s_1 &= I_1 - I_2 \\
 s_2 &= I_3 - I_4 \\
 s_3 &= I_5 - I_6
 \end{aligned}
 \tag{6.3}$$

where  $I_1$  and  $I_2$  are the irradiance with the polarizer transmission along the vertical and horizontal axis without the quarter-wave plate, respectively.  $I_3$  and  $I_4$  are irradiance with the polarizer transmission angle at 45 and 270 degrees without the quarter-wave plate, respectively.  $I_5$  and  $I_6$  are the irradiance when quarter-wave plate fast axis is at 90 and 270 degrees, respectively. When  $s_0$  is non-zero and  $s_1$  through  $s_3$  are zero, then the field is unpolarized; when  $s_0$ ,  $s_1$ , and  $s_2$  are non-zero and  $s_3$  is zero, the field is linearly polarized; however, when  $s_0$  and  $s_3$  are non-zero and  $s_1$  and  $s_2$  are zero then field is circular polarized; when all the components are non-zero then field is elliptically polarized. For the case of circular polarized light, the linear polarizer has no effect on the irradiance measurement other half-reduction in optical power since a circular polarization can have rotation position that will match the polarization angle of the polarizer. This effect will be used later in chapter 11 to separate out circular and linearly polarized light.

For simulation purposes, the Stokes method is probably not the best if the fields are calculated as is done during computer simulations. Jones calculus can be used when field information is available. The Jones vector utilizes two components derived directly from Eq. 6.1:

$$\bar{J} = \begin{bmatrix} E_x \\ E_y e^{i\delta} \end{bmatrix}
 \tag{6.4}$$

The polarization state for a specific phase difference has been already described in the previous section. Eq 6.5 shows the Jones vectors for circular, elliptical, and linear polarization states (Yu, et al. 2002, Milster 2005).

---


$$\begin{aligned}\bar{J}_x &= \begin{bmatrix} 1 \\ 0 \end{bmatrix} & \bar{J}_y &= \begin{bmatrix} 0 \\ 1 \end{bmatrix} \\ \bar{J}_{LHC} &= \begin{bmatrix} 1 \\ j \end{bmatrix} & \bar{J}_{RHC} &= \begin{bmatrix} 1 \\ -j \end{bmatrix}\end{aligned}\tag{6.5}$$

---

If there n-systems to model, the resulting field of the system can be determined from an initial Jones vector by utilizing a 2x2 Jones matrix such that:

$$\bar{J}_f = M_N M_{N-1} \dots M_1 \bar{J}_i ,\tag{6.6}$$

where  $M_n$  represent the transformation matrix for a system of N optical systems. Eq 6.7 shows the Jones transformation matrices for vertical and horizontal linear polarization, left and right handed circular polarization, rotation matrix, and a general retarder, respectively:

:

---


$$\begin{aligned}
M_x &= \begin{bmatrix} 1 & 0 \\ 0 & 0 \end{bmatrix} & M_y &= \begin{bmatrix} 0 & 0 \\ 0 & 1 \end{bmatrix} \\
M_{LHC} &= \begin{bmatrix} 1 & 0 \\ 0 & j \end{bmatrix} & M_{RHC} &= \begin{bmatrix} 1 & 0 \\ 0 & -j \end{bmatrix} \\
M(\theta) &= \begin{bmatrix} \cos \theta & \sin \theta \\ -\sin \theta & \cos \theta \end{bmatrix} & M(\phi) &= e^{j\frac{\phi}{2}} \begin{bmatrix} 1 & 0 \\ 0 & e^{j\phi} \end{bmatrix}
\end{aligned} \tag{6.7}$$


---

The rotator matrix rotates the polarization of initial field and the phase retarder inserts a delay between the two states of polarization. A combination of rotating matrix and 90 degree phase retarder plate can be used to convert between polarization states, for example converting a linearly polarized light to circular light and visa-versa:

$$\begin{bmatrix} E_{1,x} \\ E_{1,y} \end{bmatrix} = M_{-45^\circ} M_{\frac{\pi}{2}} M_{45^\circ} \begin{bmatrix} 1 \\ 0 \end{bmatrix}, \tag{6.8}$$

where  $E_{1,x}$  and  $E_{1,y}$  are the fields for the x and y polarization states and  $M_p$ ,  $M_c$ ,  $M_{R(\lambda)}$ , and  $M_{\pm 45^\circ}$  are the Jones matrices for the polarizers, Quarter-wave plate, and 45 degree rotators, respectively.

## 7. BASIC MECHANICS OF MATERIALS

This chapter gives an overview of mechanics of materials. Concepts such as strain, stress, strain-stress curves are discussed. This applied towards understanding beam structures such as cantilever beams. Finite element numerical tools are discussed to model complex structures. Towards the end, the block diagram implementation of the Structural Processor is discussed.

### 7.1. Axial stress and strain

The most fundamental concepts in engineering mechanics are stress and strain. Figure 7.1 shows an example of axial stress and strain of a rod. A rod with an initial length  $L$  is stretch by a distance  $\Delta L$  by axial force  $P$ . Assuming the axial force  $P$  is acting at the centroid of the bar, the stress of the bar subject to force  $P$  is given by:

$$\sigma = \frac{P}{A} \quad (7.1)$$

In Eq 7.1, the bar is assumed to be prismatic (uniform cross section).

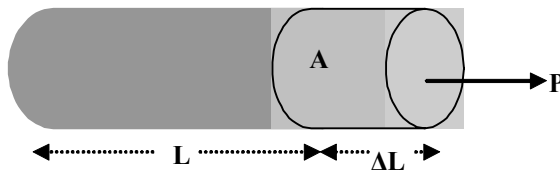


Figure 7.1 Axial strain and stress.

The axial strain is defined as the ratio between the displacement of the rod and the original length:

$$\varepsilon_x = \frac{\Delta L}{L} \quad (7.2)$$

## 7.2. Stress-strain curves

The relationship between stress and strain is function of the material property. The stress and strain curve can be used to illustrate the relationship between stress and strain. Figure 7.2 shows the typical stress-strain curve for low mild steel (Gere 2004).

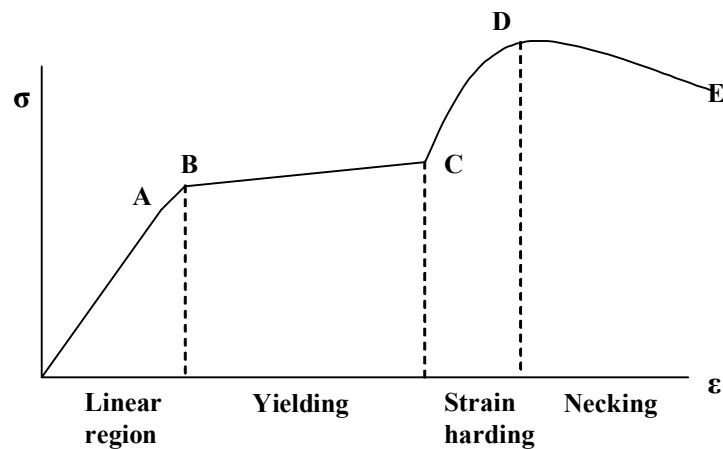


Figure 7.2 Stress-strain curve of mild steel.

In the linear region of the curve, stress increases linearly with strain, until point A or at the proportional limit. The ratio between stress and strain in this region is called the Modulus of elasticity or Young's Modulus of the material. After point A, the stress increases slowly with strain until the point B, or the Yield stress point. Beyond the yield point, the stress-strain curve is basically flat; this means that the material is strained with no increase in stress. In this region, the material is said to be undergoing

perfect plasticity. At point C, stress increases rapidly until the ultimate stress point D is reached; this rapid increase is due to decrease in the cross sectional area of the material. The material continues to be strained after point D but the stress drops until the material fractures at point E. In this region, the necking is observed around the fracture. It is easier to predict the fracture point of steel compared to brittle materials because of the cycles described in Figure 7.2. This is because for brittle materials, the fracture point can occur quite rapidly and without any warning. Figure 7.3 shows the case of brittle materials such as glass and glass composites.

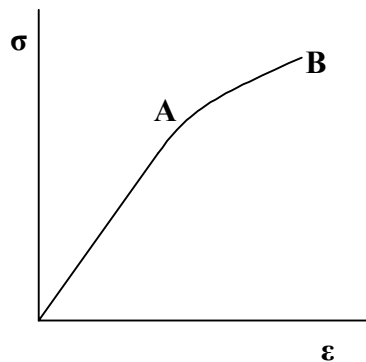


Figure 7.3 Typical strain-stress curve for brittle materials.

As shown in Figure 7.3, there is no yield point as is the case for steel and the material fractures at point B without warning. Most engineering materials operate in the linear region of the curve and below some multiple of the yield point of the materials. The allowed stress is typically specified by regulation codes and is defined at the ratio

between the Yield point of the material and the factor of safety. The allowed load is then the given by the cross sectional area of the material multiplied by the allowed stress.

### 7.3. Hooke's Law

A material is termed elastic if it returns to its original state after loading and unloading. If the material is elastic and linear, Hooke's law can be used to relate the stress and strain of the material through the modulus of elasticity (Gere 2004):

$$\sigma = E\varepsilon \quad (7.3)$$

Eq. 7.4 also assumes a linear, isotropic, and homogenous material. If a material is stretched along the axis, there will be a corresponding decrease in the cross sectional area of the bar, resulting in lateral strain and stress. The ratio between the lateral strain and axial strain is unique to the material and is called Poisson's Ratio:

$$\nu = -\frac{\varepsilon_l}{\varepsilon_x}, \quad (7.4)$$

where  $\varepsilon_l$  is the lateral strain. Most materials have Poisson's ratio in the range of 0.25-0.35. For an axial strain there is also a corresponding shear strain  $\tau$ . If the rod is stretched along the axis, there will be a corresponding decrease in its cross sectional, resulting in lateral strain:

$$\tau = G\gamma, \quad (7.5)$$

where G is the shear modulus of elasticity. It so happens that the modulus of elasticity is related to the shear modulus:

$$G = \frac{E}{2(1 + \nu)} \quad (7.6)$$

In reality, strain and stress are tensors of rank 2 and are related through a tensor of rank 4. For tensor of rank 4, there is 81 possible components, however, not all 81 components are independent and the tensor of rank 4 can be reduced to a 6x6 matrix with 36 components such that:

$$\begin{bmatrix} \varepsilon_{11} \\ \varepsilon_{22} \\ \varepsilon_{33} \\ 2\varepsilon_{23} \\ 2\varepsilon_{31} \\ 2\varepsilon_{12} \end{bmatrix} = [C] \begin{bmatrix} \sigma_{11} \\ \sigma_{22} \\ \sigma_{33} \\ \sigma_{23} \\ \sigma_{31} \\ \sigma_{12} \end{bmatrix}, \quad (7.7)$$

where  $\sigma_{ii}$ ,  $\sigma_{ij}$ ,  $\varepsilon_{ii}$ , and  $\varepsilon_{ij}$  are the axial stresses, shear stresses, axial strains, and shear strains, respectively. The C-matrix is symmetric and the number of independent components reduces to 21. For the case of an isotropic material (material with three planes and three axes of symmetry), the C-matrix contains only two independent variables and is given by (Kundu 2003):

$$\frac{1}{E} \begin{bmatrix} 1 & -\nu & -\nu & 0 & 0 & 0 \\ -\nu & 1 & -\nu & 0 & 0 & 0 \\ -\nu & -\nu & 1 & 0 & 0 & 0 \\ 0 & 0 & 0 & \frac{1}{G} & 0 & 0 \\ 0 & 0 & 0 & 0 & \frac{1}{G} & 0 \\ 0 & 0 & 0 & 0 & 0 & \frac{1}{G} \end{bmatrix} \quad (7.8)$$

### 7.4. Deflection of beams

A beam is structural that supports lateral loads as opposed to rods, where the load is axial. There are several types of beams depending on the type of support; Figure 7.4 shows the case for a cantilever beam. In the cantilever beam, one end remains fixed while other is free; this means that deflection and angular displacement is zero at the fixed end. When a shear force  $V$  is applied, the beam will be deflected as shown in Figure 7.4(b). The deflection peaks at the tip and zero at the clamped end of the beam.

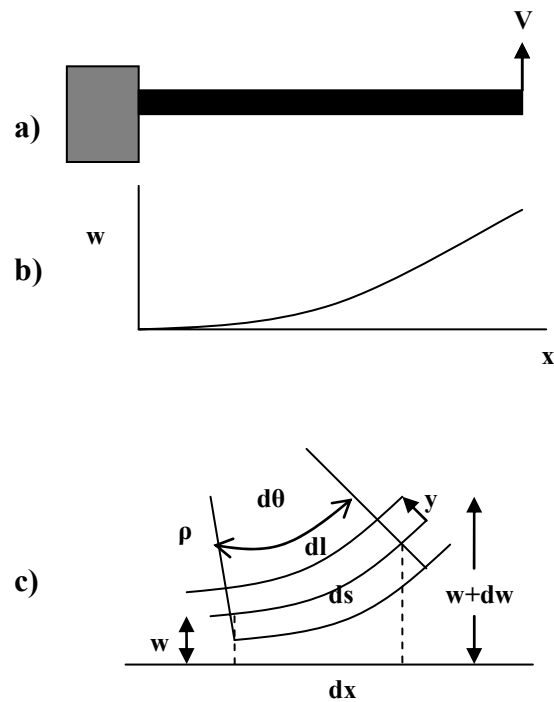


Figure 7.4 (a) Cantilever beam. (b) Deflection of the beam subject to distributed shear force  $f(x)$ . (c) Close up of a small section of the deflected beam.

In Figure 7.4(c), above the section of neutral line  $ds$ , the beam is in compression, and below the neutral line, the beam is in tension. For the case of angular section ( $d\theta$ ) of the beam, the length of section  $dl$  is then given by:

$$dl = (\rho - y)d\theta = ds - \frac{y}{\rho} ds, \quad (7.9)$$

where  $\rho$  is the radius of curvature. The resultant axial strain due to the bending can then be related to the radius curvature of the beam (Gere 2004):

$$\varepsilon_s = y \frac{d^2 w}{dx^2} = \frac{-y}{\rho} \quad (7.10)$$

The axial strain can then be related to the material parameter of the beam. For a material with modulus  $E$ , the axial stress is then given:

$$\sigma_s = -\frac{Ey}{\rho} \quad (7.11)$$

For pure bending, no axial force is applied so the sum of the stress across the cross-sectional area should be zero and the neutral point can be determined by solving:  $\int_A y dA = 0$ . Similarly for the moment:

$$\begin{aligned} M &= \int_A \sigma_s dA \\ &= \int_A \frac{Ey^2}{\rho} dA, \quad (7.12) \\ &= \frac{EI}{\rho} \end{aligned}$$

where  $I$  is the geometric moment of inertia:  $\int_A y^2 dA$ ; the moment is then related to the geometric and material property of the cantilever beam. The final task is then to relate the

displacement of the beam with the geometrical and material properties of the beam. The slope of the deflection is given by:

$$\frac{dw}{ds} = \tan \theta \quad (7.13)$$

For small angles, Eq. 7.13 can further be reduced to:

$$\frac{dw}{dx} = \theta \quad (7.14)$$

This can then be related to the curvature by taking the second derivative:

$$\frac{d^2w}{dx^2} = \frac{d\theta}{dx} = \frac{1}{\rho} = \frac{M}{EI_x} \quad (7.15)$$

This is then be related to the shear load (V) and the distributed shear forces (f(x)) by taking the third and fourth derivative of the displacement function, respectively:

$$\begin{aligned} \frac{d}{dx} (EI_x \frac{d^2w}{dx^2}) &= V \\ \frac{d^2}{dx^2} (EI_x \frac{d^2w}{dx^2}) &= -f(x) \end{aligned} \quad (7.16)$$

where  $\frac{dV}{dx} = -f(x)$  and  $\frac{dM}{dx} = V$  (Gere 2004). The latter of Eq. 7.16 is generally known as the Bernoulli's beam equation.

## 7.5. Finite element representation

The Bernoulli beam equation can be solved analytically or numerically. The solutions become complex when the cross section of the beam varies or if the beam is made of varying materials. A straight forward numerical method to solve mechanical response of structures for various boundary conditions is to use finite element modeling

(FEM). In the case of a beam, a FEM is developed by first isolating a section of the structure (element) and reducing the fourth and second order equation to low order differential equation (weaker form). This is accomplished by weighting the differential equation (DEQ) and integrating along the FEM. Integration by parts is then used to reduce the order of the DEQ (Reddy 1993):

$$\int_{x_1}^{x_2} s \left( \frac{d^2 u}{dx^2} - f(x) \right) dx = \int_{x_1}^{x_2} \left( \frac{ds}{dx} \frac{du}{dx} - f(x) \right) dx - \left[ s \frac{du}{dx} \right]_{x_1}^{x_2}, \quad (7.18)$$

where  $s$  is the weighting function that must be differential up to the maximum order of the DEQ. Figure 7.5 shows a FEM for a section of a beam. For the case of the beam, two degrees exist at node 1 and 2, representing deflection ( $w$ ) and slope ( $\theta$ ) and shear force ( $Q1$ ) and moment ( $Q2$ ).

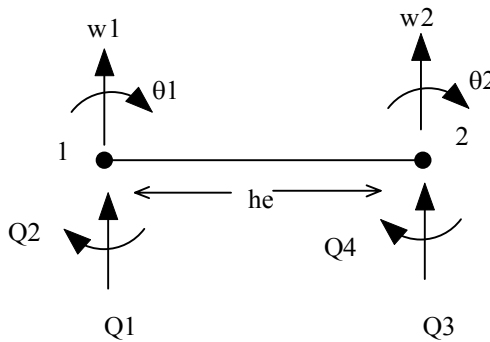


Figure 7.5 Finite element model for a beam

The weak form is further reduced to a set of four linear equations that can be solved using linear systems theory. In general FEM models are general purpose and are also used for problems not related to mechanics, for example, electromagnetic propagations in optical

devices. The finite element analysis (FEA) engine used in this work is able to solve fourth order and second order spatial and time derivatives:

$$-\frac{\partial}{\partial x} \left( a \frac{\partial u}{\partial x} \right) + \frac{\partial^2}{\partial x^2} \left( b \frac{\partial^2 u}{\partial x^2} \right) + c_0 u + c_1 \frac{\partial u}{\partial t} + c_2 \frac{\partial^2 u}{\partial t^2} = f(x, t) \quad (7.19)$$

Assuming the variable  $u$  can be approximated as:

$$u(x, t) \approx U^e(x, t) = \sum_{j=1}^n u_j^e(t) \psi_j^e(x) \quad (7.20)$$

Where  $n$  is the total number of independent orthogonal functions and is also the number of nodes of the element. The resulting FEM is then given by (Reddy 1993):

$$[K]\{u\} + [M^1]\{\dot{u}\} + [M^2]\{\ddot{u}\} = \{F\}, \quad (7.21)$$

Where

$$[K] = [K^1] + [K^2] + [M^0] \quad (7.22)$$

And

$$\begin{aligned} M_{ij}^0 &= \int_{x_A}^{x_B} c_0 \psi_i \psi_j dx \\ M_{ij}^1 &= \int_{x_A}^{x_B} c_1 \psi_i \psi_j dx \\ M_{ij}^2 &= \int_{x_A}^{x_B} c_2 \psi_i \psi_j dx \quad , \\ K_{ij}^1 &= \int_{x_A}^{x_B} a \frac{d\psi_i}{dx} \frac{d\psi_j}{dx} dx \\ F_i &= \int_{x_A}^{x_B} \psi_i f dx + \hat{Q}_i \end{aligned} \quad (7.23)$$

Where

$$\begin{aligned}
 Q_1 &= \left[ -a \frac{\partial u}{\partial x} + \frac{\partial}{\partial x} \left( b \frac{\partial^2 u}{\partial x^2} \right) \right]_{X_A}, & Q_2 &= \left( b \frac{\partial^2 u}{\partial x^2} \right)_{X_A}, \\
 Q_3 &= \left[ -a \frac{\partial u}{\partial x} + \frac{\partial}{\partial x} \left( b \frac{\partial^2 u}{\partial x^2} \right) \right]_{X_B}, & Q_4 &= \left( b \frac{\partial^2 u}{\partial x^2} \right)_{X_B},
 \end{aligned} \tag{7.24}$$

For the case of a beam  $a=0$  and for the case of a rod  $b=0$ . Once the element matrices are determined, individual FEM elements are then assembled into a global stiffness and generalized force matrixes, boundary condition are then imposed, and the primary variables solved. For the cantilever beam, the deflection at the clamped end and the moment at the tip end is zero. Figure 7.6 shows the block diagram static implantation of a Structural Processor (SP) used in this work. The SP controls the flow of information from the main processor as discussed in Chapter 2, and also orchestrates the assembling and solving of the FEM. In addition, the SP also determines the optical response of attached sensors. The basic outline is as follows: A set of orthogonal fitting functions are used to determine the FEM matrices as outlined from Eq. 7.22-7.24. This is done for every element of the structure. The FEM is then assembled into a global matrix to form a set of linear equations as given by Eq. 7.21. Structural boundary conditions are then imposed. The solver then determines the primary variables of interest (forces, deflections, strain, etc.). The photoelastic component of the block diagram is discussed in Chapter 8.

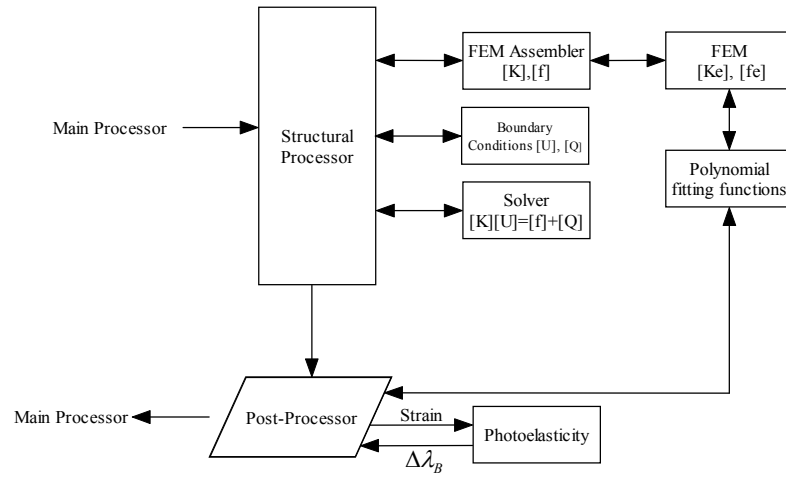


Figure 7.6 Block diagram implementation of the FEM.

Figure 7.7 shows a simulation run for a 2-meter tapered steel ( $E=200\text{GPa}$ ) cantilever beam structure subject to 500N (112lb) tip shear force.

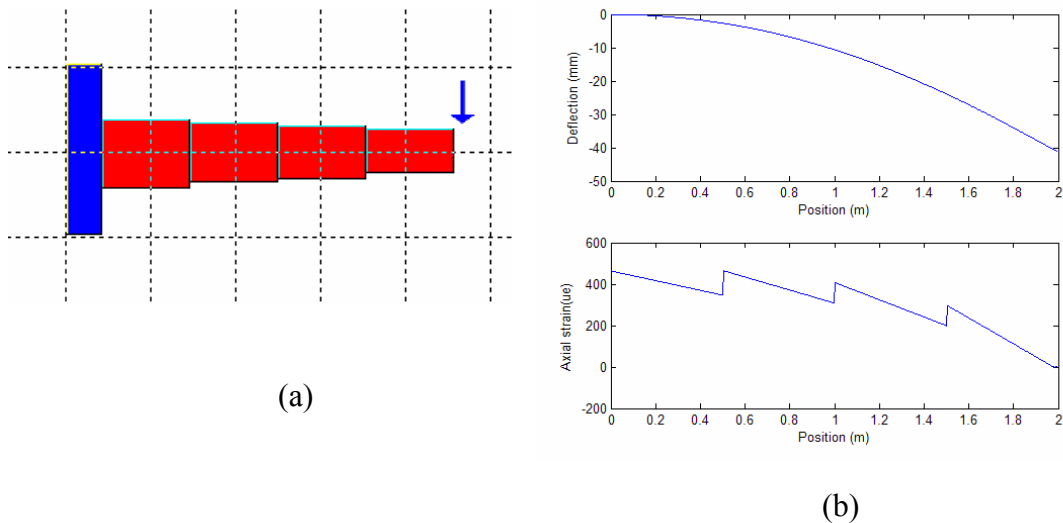


Figure 7.7 2 meter 1 degree tapered cantilever beam with 500 N tip force. (a) Layout of the beam (b) deflection and axial strain along the length of the cantilever beam.

The maximum height of the beam is 4 cm at the fixed end and the tapering angle is 1 degrees. Figure 7.7b shows the deflection and axial strain information. Notice that the peak deflection (41 mm) is at the tip and the maximum axial strain (464  $\mu\epsilon$ ) is next to clamp (fixed end). Maximum curvature (moment) occurs at the fixed end so it is expected to have peak strain. The discontinuity is due to the sectioning of the beam and the differences in the moment of inertia for each section.

## 8. OPTO-MECHANICAL RELATIONS

In order for optical sensing devices to be useful for measuring physical parameters such as temperature and strain, a relation between the measuring parameter and the optics must be determined. In this section, the opto-mechanical relation for an interferometric and fiber Bragg grating sensors will be determined theoretically and measured using a Fabry-Perot Strain Gauge Calibrator. The goal will be to determine the change in the Bragg wavelength (center wavelength) of a FBG strain sensor for a corresponding change in strain observed. The results will be used to determine the strain gauge factor (SGF) of the boron/germanium co-doped fiber in a non-destructive fashion.

### 8.1. Temperature and strain sensitivities

The optical path length of an optical sensor is a function of the refractive index and the length of the optical fiber. For an optical sensor with a gage length of  $L$ , the optical path length is by:

$$OPL = nL \quad (8.1)$$

An incremental change in the optical path length with respect to a reference stress and temperature state is given by:

$$\Delta OPL = OPL(\sigma, T) - OPL(\sigma_0, T_0), \quad (8.2)$$

where  $\sigma_0$  and  $T_0$  are the initial stress and temperature conditions. Taking the linear term of the Taylor series expansion of equation 8.2 gives the changes in the optical path length due to stress and temperature changes or more formally (Measures 2002):

$$\Delta OPL = \left[ \frac{\partial OPL}{\partial \sigma} \right]_T \Delta \sigma + \left[ \frac{\partial OPL}{\partial T} \right]_{\sigma} \Delta T, \quad (8.3)$$

where the above are with respect to constant temperature and stress for changes in stress and temperature, respectively. Inserting equation 8.1 into 8.3 and expanding gives:

$$\Delta OPL = \left[ n \frac{\partial L}{\partial \sigma} + L \frac{\partial n}{\partial \sigma} \right]_T \Delta \sigma + \left[ n \frac{\partial L}{\partial T} + L \frac{\partial n}{\partial T} \right]_{\sigma} \Delta T \quad (8.4)$$

Rearranging the above equation and introducing strain:

$$\Delta OPL = nL \left( \left[ \frac{\partial \varepsilon}{\partial \sigma} + \frac{1}{n} \frac{\partial n}{\partial \varepsilon} \frac{\partial \varepsilon}{\partial \sigma} \right]_T \Delta \sigma + \left[ \frac{\partial \varepsilon}{\partial T} + \frac{1}{n} \frac{\partial n}{\partial T} \right]_{\sigma} \Delta T \right) \quad (8.5)$$

Introducing Young's modulus and the thermal expansion coefficient  $\alpha$ :

$$\Delta OPL = nL \left( \left[ 1 + \frac{1}{n} \frac{\partial n}{\partial \varepsilon} \right]_T \frac{\Delta \sigma}{Y} + \left[ \alpha + \frac{1}{n} \frac{\partial n}{\partial T} \right]_{\sigma} \Delta T \right) \quad (8.6)$$

Introducing strain and temperature sensitivity:

$$\begin{aligned} \xi_{\varepsilon} &= 1 + \frac{1}{n} \left[ \frac{\partial n}{\partial \varepsilon} \right]_T \\ \xi_T &= \alpha + \frac{1}{n} \left[ \frac{\partial n}{\partial T} \right]_{\sigma} \end{aligned} \quad (8.7)$$

The fractional change in the optical path length due to changes in temperature ( $\Delta T$ ) and strain ( $\Delta \varepsilon$ ) can be stated simply:

$$\frac{\Delta OPL}{OPL} = \xi_{\varepsilon} \Delta \varepsilon + \xi_T \Delta T, \quad (8.8)$$

Where,

$$\begin{aligned} \Delta \varepsilon &= \varepsilon - \varepsilon_0 \\ \Delta T &= T - T_0 \end{aligned} \quad (8.9)$$

## 8.2. Photoelasticity

For the relation in Equation 8.8 to be useful, the photo-elasticity must be determined. A change in strain will result in a corresponding change in the index of refraction (Measures 2002):

$$\left[ \frac{\partial n}{\partial \varepsilon} \right]_T \Delta \varepsilon = \Delta n \quad (8.10)$$

From photo-elastic theory, for a field polarized in the  $i_{\text{th}}$  direction within the fiber, the corresponding change in index of refraction in the  $i_{\text{th}}$  direction due to a strain field in the  $j_{\text{th}}$  direction (cf. Figure 8.1) is given by (Measures 2002):

$$\Delta n_i = - \sum_{j=1}^6 \frac{n_i^3}{2} \rho_{ij} \varepsilon_j \quad (8.11)$$

where  $\rho$  is the photo-elastic or strain-optic tensor,  $\varepsilon_1$  to  $\varepsilon_3$  are the principle or axial strains, and  $\varepsilon_4$  to  $\varepsilon_6$  are the shear strains.

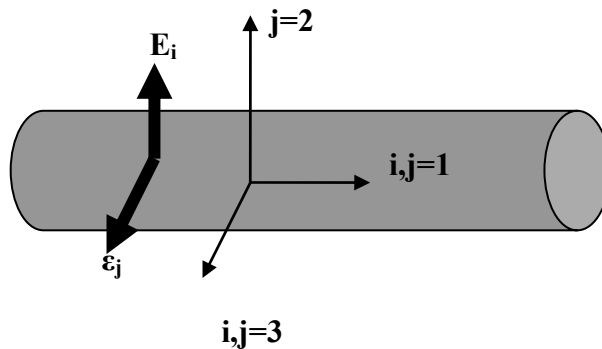


Figure 8.1 The orthogonal directions in an optical fiber shown in Eq. 8.11 (Measures 2001)

Throughout this work, the 1-direction is along the fiber axis. Plugging Eq. 8.11 into 8.10 and using the results to expand Eq. 8.8 results in the following fraction change in the optical path length for field polarized in the  $i$ th direction, assuming originating from initial zero stress position:

$$\left[ \frac{\Delta OPL}{OPL} \right]_i = \varepsilon_i - \frac{n_i^2}{2} \rho_{ij} \varepsilon_j + \xi_T \Delta T \quad (8.12)$$

For an isotropic, homogenous medium, the strain-optic tensor contains only two independent components  $\rho_{11}$  and  $\rho_{12}$ . The photo optic tensor then becomes (Measures 2001):

$$\rho_{ij} = \begin{bmatrix} \rho_{11} & \rho_{12} & \rho_{12} & 0 & 0 & 0 \\ \rho_{12} & \rho_{11} & \rho_{12} & 0 & 0 & 0 \\ \rho_{12} & \rho_{12} & \rho_{11} & 0 & 0 & 0 \\ 0 & 0 & 0 & 1/2(\rho_{11} - \rho_{12}) & 0 & 0 \\ 0 & 0 & 0 & 0 & 1/2(\rho_{11} - \rho_{12}) & 0 \\ 0 & 0 & 0 & 0 & 0 & 1/2(\rho_{11} - \rho_{12}) \end{bmatrix} \quad (8.13)$$

For a purely axial strain field in the direction of the optical fiber or 1-direction and with no transverse coupling and shear strains, the strain field vector is given by the following:

$$\bar{\varepsilon} = \begin{bmatrix} \varepsilon_1 \\ -\nu \varepsilon_1 \\ -\nu \varepsilon_3 \\ 0 \\ 0 \\ 0 \end{bmatrix}, \quad (8.14)$$

where  $\nu$  is again the Poisson's ratio. Plugging 8.13 and 8.14 into 8.12, and assuming a constant temperature, the fraction change in optical path length due to strain in the fiber optic axial direction becomes:

$$\frac{\Delta OPL}{OPL} = \varepsilon_1 - \frac{n^2}{2}(\rho_{12} - \nu(\rho_{11} - \rho_{12})) \cdot \varepsilon_1 = G_\varepsilon \varepsilon_1 \quad (8.15)$$

For the case of fused silica glass,  $\rho_{11}=0.121$ ,  $\rho_{12}=0.270$ ,  $\nu=0.17$ , and  $n=1.458$ , the SGF is 0.78. The phase change due to changes in optical path length is directly related to the propagation constant for the case of an interferometric sensor. For the case of FBGs, the change in the Bragg wavelength due to changes in the optical path length is directly related to changes in the periodicity of the grating as given by Bragg condition. The net effect is that the fraction change in the Bragg wavelength is directly proportional to the fractional change in the optical path length (Measures 2002, Udd 1995):

$$\frac{\Delta \phi}{\phi} = \frac{\Delta \lambda_B}{\lambda_B} = \frac{\Delta OPL}{OPL} \quad (8.16)$$

where the phase due to an optical path length  $nL$  is given by

$$\phi = \frac{2\pi n}{\lambda} L, \quad (8.17)$$

### 8.3. Fabry-Perot Strain Gauge Calibrator

The following experiment determined the SGF for a Boron/Germanium co-doped fiber using a non-destructive Fabry-Perot Strain Gauge Calibration system. The FPI strain gauge calibrator setup is shown in Figure 8.2. The dimension of setup is 18 cm x 3.7 cm x 2 cm and is composed of four main components: rail, two sensor holders, piezoelectric actuator, and a FPI displacement sensor. The setup was fabricated from Aluminum using

a vertical milling machine. The rail is used to adjust the gauge length,  $L_g$ , by varying the relative position of the sensor holders. The aluminum sensor holders hold both ends of the test sensor. On one sensor holder (SH#2) is a tensioner that keeps one end of the test sensor fixed by friction adjusted with side screw. The second holder (SH#1) is attached to the piezoelectric actuator through a cemented machine screw. SH#1 and SH#2 are composed of a lower and upper-half. The lower-half slides on the aluminum rail while the upper half clamps the test sensor in place. To prevent the sensor holders from damaging the sensors, two thin layers of plastic were glued between the upper and lower parts. Two machine screws were then used to tightly grip the test sensor in order to reduce slippage of the sensor holders. The piezoelectric actuator (cf. Figure 8.3(a)) used was fabricated with a 2.7 cm diameter mono-morphic piezoceramic transducer, Radio-Shack model 273-0373A. The transducer was employed because of availability. A mono-morphic base plate consists of a metallic base plate and a piezoceramic basic plate. The diameter of piezoceramic plate diameter is 20.3 mm and the thickness is 0.2 mm. When a field is applied across the piezoceramic, the piezoceramic will expand radially, bending the metallic base plate laterally and pulling SH#1 (Sun 2004). The piezoceramic used is polled such that the base plate bends away from the piezoceramic side. This means that the SH#1 had to be cemented to piezoceramic side instead of the metallic side so that the actuator pulls SH#1 instead of pushing it.

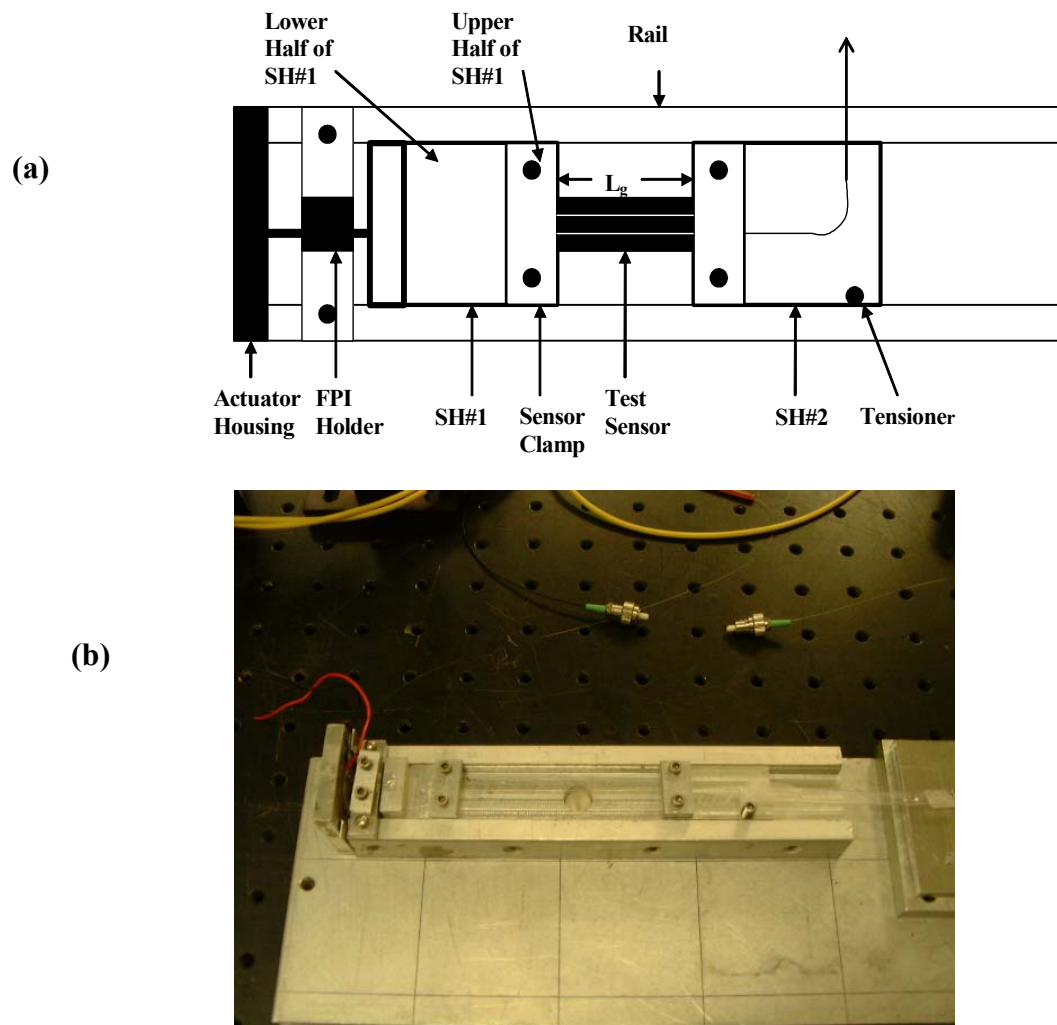


Figure 8.2 The physical layout of the Fabry-Perot interferometric (FPI) strain gauge calibration system.

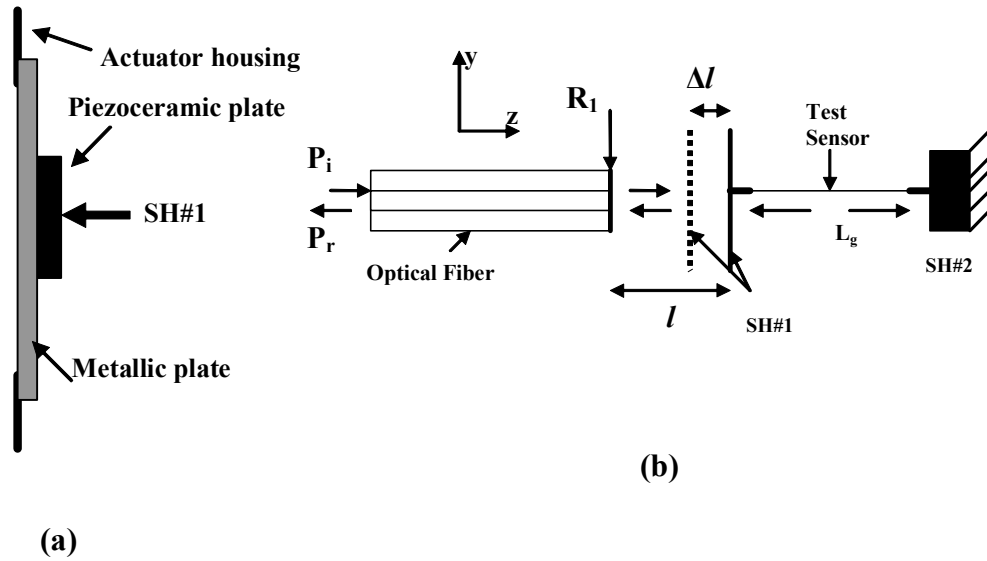


Figure 8.3 Main components of FPI strain gauge calibrator. (a) Mono-morphic piezoceramic actuator and (b) FPI displacement and test sensor.

A low finesse FPI displacement sensor (cf. Figure 8.3(b) and Chapter 5) was setup between a cleaved tip (surface  $R_1$ ) of a single mode SMF 28 optical fiber and the machine finished surface of SH#1. The optical field reflects from both end faces and interferes. Interference fringes are produced at the output of the FPI as the position of surface SH#2 varies, and the distance between the fringes is  $\lambda/2$ . The resulting strain in the test sensor due to a displacement  $\Delta l$  is then given by:

$$\varepsilon = \frac{\Delta l}{L_g} = N \frac{\lambda}{2L_g}, \quad (8.18)$$

where  $L_g$  and  $N$  are the gauge length and the corresponding number of observed fringes, respectively. If a single fringe is miscounted, the error of the fringe count would be  $1/N$ ,

however, for most cases, a peak is counted to within an error of  $\pm\lambda/16$  or 70.7% of the peak assuming a cosine function for the low finesse FPI reflectance signal, therefore, the estimated fringe count error will be  $\pm 1/8N$ . The previous error can be reduced further by the root of the number of measurements or runs of the experiment.

### **8.3.1. FPI strain gauge calibration setup and sensors**

Figure 8.4 shows the FPI strain gauge calibration setups and connections to external measurement equipment. For both setups, a high voltage source (Bertan 230) was used to drive the piezoelectric actuator, and a 1542.94 nm diode laser (ILX Lightwave 7900) was used as a source for FPI. A computer based oscilloscope attached to a fiber optic photo-detector (ILX Lightwave 1820) was used to observe the fringes from the FPI. The cavity length of the FPI was manually adjusted until maximum fringe contrast was observed on the oscilloscope.

Figure 8.4(a) shows the FPI strain gauge calibration setup to calibrate the FBG test sensor. The FBG sensor fabricated in Chapter 4 was used as the test sensor. The gauge length for the calibration process was 8 cm and the total length of photosensitive fiber used was 13 cm. Beyond the 13 cm of photosensitive fiber was a length of standard SMF 28 fiber. About 10 cm of the photosensitive fiber was striped down to the cladding. An optical spectrum analyzer (HP 86140A) with minimum bandwidth resolution (ability to distinguish between two peaks) of 0.07 nm was used to observe the reflected FBG spectrum.

Figure 8.4(b) shows the setup to calibrate the SGF for the electric (resistive) strain gauge (ESG). The basic ideal of calibrating the RSG was to validate the FPI strain gauge

calibrator. The ESG used was model CEA-06-250UN-120 (Vishay, Inc.), with a gauge length of 6.35 mm and a substrate length of 13.2 mm. The SGF given by the manufacturer was  $2.085 \pm 0.5\%$ . Typically, the SGF quoted by the manufacture is the average SGF as determined from a batch of ESGs. A simple quarter Wheatstone bridge and a single stage operational amplifier gauge amplifier with a gain set at 65.4 were used to interrogate the ESG. A change in the voltage output of a balanced quarter-Wheatstone bridge is directly related to the induced strain. The strain-voltage relationship with the quarter bridge arrangement is given by the following (Figliola 2000):

$$\frac{\Delta V}{V} = \frac{SGF \cdot \Delta \epsilon}{4 + 2 \cdot SGF \cdot \Delta \epsilon} \approx \frac{SGF \cdot \Delta \epsilon}{4}, \quad (8.19)$$

where  $V$  and  $\Delta V$  are the bridge voltage and the change in the bridge voltage, respectively. The quarter bridge source voltage was regulated and the bridge base voltage was set at 3.1 V. Measurements were taken from the quarter Wheatstone bridge/amplifier arrangement using a digital voltmeter (DVM). The resolution of the Wheatstone and strain gauge amplifier is estimated to be  $1\mu\epsilon$ .

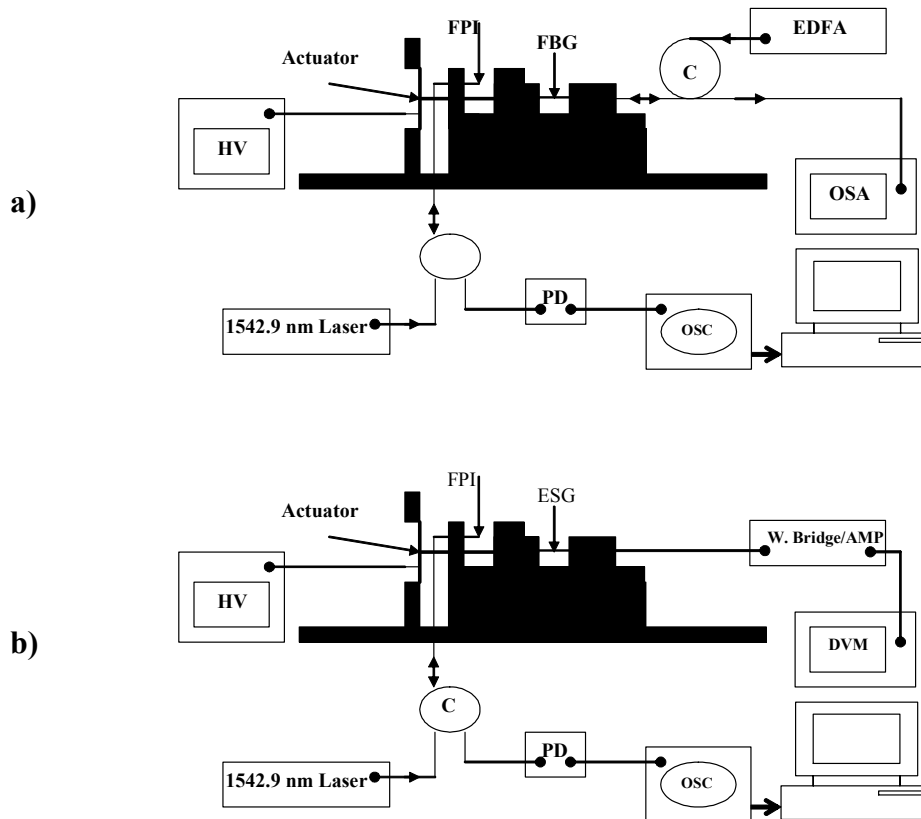


Figure 8.4 (a) Hardware setup used to measure the strain gauge factor of a fiber Bragg grating (FBG). (b) Hardware setup used to measure the strain gauge factor of an electric strain gauge (ESG).

## 8.4. Experiment and Results

### 8.4.1. Piezoceramic actuator characterization

All piezoelectric devices exhibit some degree of hysteresis and nonlinearity (Basedow 1980). The hysteresis is the change in displacement as the piezoceramic material is loaded and unloaded. The hysteresis is a result of the residual polarization that remains in the piezoceramic material after unloading, similar to ferromagnetic materials. Non-

linearity is a deviation from linear (self-explanatory). For both case, the parameters are quoted as a percentage of maximum range. Both parameters are undesirable because it makes it difficult to have direct relations, for example, between displacement and the driving source of the piezoceramic. The hysteresis and non-linearity of the piezoceramic actuator were determined by plotting the displacement as a function of the applied voltage. The voltage across the piezoelectric actuator was manually ramped up to 160 V and then manually ramped down towards 0 V. The load on the actuator was sensor holder #1 (SH#1) only. The applied voltage was observed simultaneously on the oscilloscope along with the output of FPI displacement sensor via the fiber optic photo-detector. The cyclic loading of the piezoelectric actuator was repeated four times to get an average. Figure 8.5 shows the resulting FPI signal waveform and the applied voltage for one cycle. Figure 8.6 shows the average displacement as a function of the increasing and decreasing voltage. A 26  $\mu\text{m}$  displacement at 160 V corresponds to 34 fringes from the FPI at 1550 nm. The hysteresis and deviation from linearity of the actuator are 26.7% and 11% (increasing voltage curve) of full scale, respectively. From hysteresis and linearity values, we concluded that using the voltage to predict displacement will result in displacement errors if linear operation is assumed for the piezoelectric actuator. In addition, the voltage and displacement relationship was dependent on the loading characteristics of the test sensor.

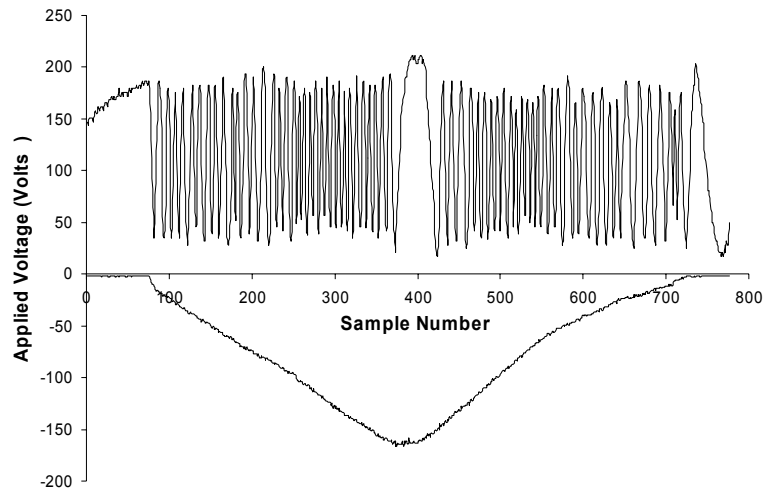


Figure 8.5 Plot of the Fabry-Perot interferometric signal and the voltage applied to the piezoceramic actuator as the sample number varies from 0 to 780.

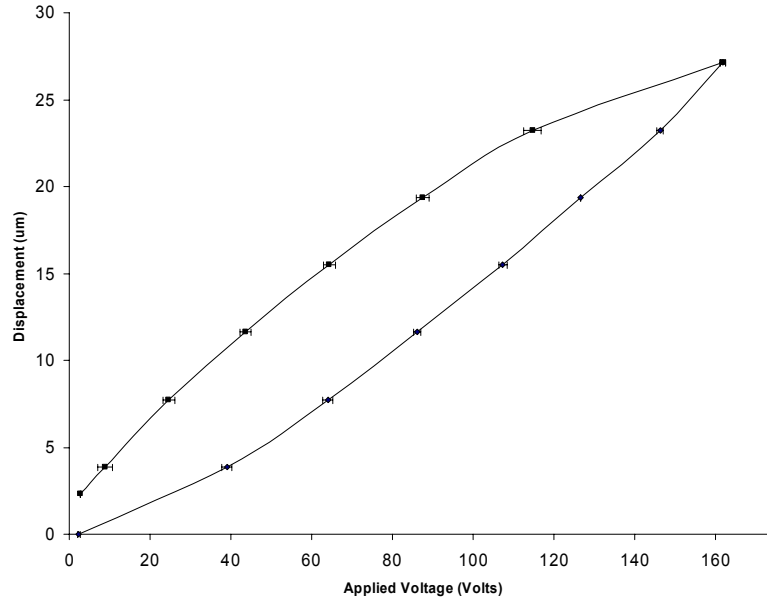


Figure 8.6 Plot of the displacement of the piezoceramic actuator as a function of the applied voltage. The load on the actuator was sensor holder #1 (SH#1) only.

#### 8.4.2. Strain gauge factor for an ESG

The gauge length of the ESG was  $11.5 \text{ mm} \pm 2.2\%$  as measured by a standard ruler. The conversion factor between strain and the number of fringes was determined to be  $67.08 \text{ } \mu\epsilon$  per fringe. The voltage across the piezoelectric actuator was manually ramped, and the fringes from the FPI sensor were counted, in addition to recording the voltage level from the bridge/amplifier. Data was taken up to the fourth fringe spacing corresponding to a peak strain of  $268 \text{ } \mu\epsilon$ . The experiment was then repeated 10 times to get an average. The estimated fringe count error for the ten runs and four fringes is about 1%. The change in the bridge voltage was determined by dividing the change in amplifier output by the gain. This was then divided by the bridge source voltage to determine the fractional change in the quarter bridge output. Figure 8.7 shows the average and standard deviation of fractional change in the bridge voltage as a function of axial strain. A linear fit of the data points is also shown. From the slope of the fit, the SGF is  $2.047 \pm 0.033 \text{ V/V}/\mu\epsilon$  (1.6%).

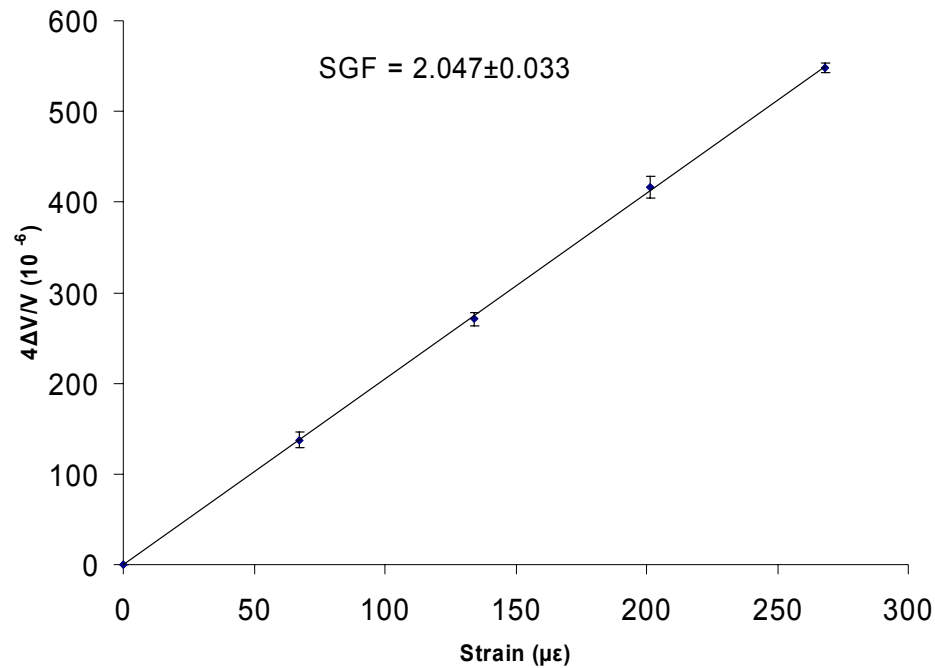


Figure 8.7 Plot of the fractional change in the quarter Wheatstone bridge voltage as a function of the measured axial strain. The solid line is a linear fit of the four data points. Note that the linear fit was forced to cross the origin.

#### 8.4.3. Strain gauge factor for a FBG

The setup in Figure 9.3(a) was used to determine the strain gauge factor of the FBG strain sensor. The conversion factor between strain and the number of fringes was determined to be 9.64  $\mu\epsilon$  per fringe. The ramping of the piezoelectric actuator was slightly different from the previous procedure for the ESG. The high voltage source was manually ramped in four stages corresponding to 4, 8, 12, and 16 fringe spacings, with each stage starting from the initial position. The entire measurement procedure was repeated three times to for average values. The estimated fringe count error for the three runs and 16 fringes is about 0.45%. The fractional change in the Bragg wavelength was determined by dividing the change in the Bragg wavelength by the Bragg wavelength. A

procedure, similar to that described in the ESG calibration section above, was used to determine the SGF for the FBG strain sensor. Figure 8.8 shows the average and standard deviation of the fraction change in Bragg wavelength as a function of strain. A linear fit of the data points is also shown. From the slope of the fit, the SGF is  $0.77 \pm 0.021$  m/m/ $\mu\epsilon$  (5.45%).

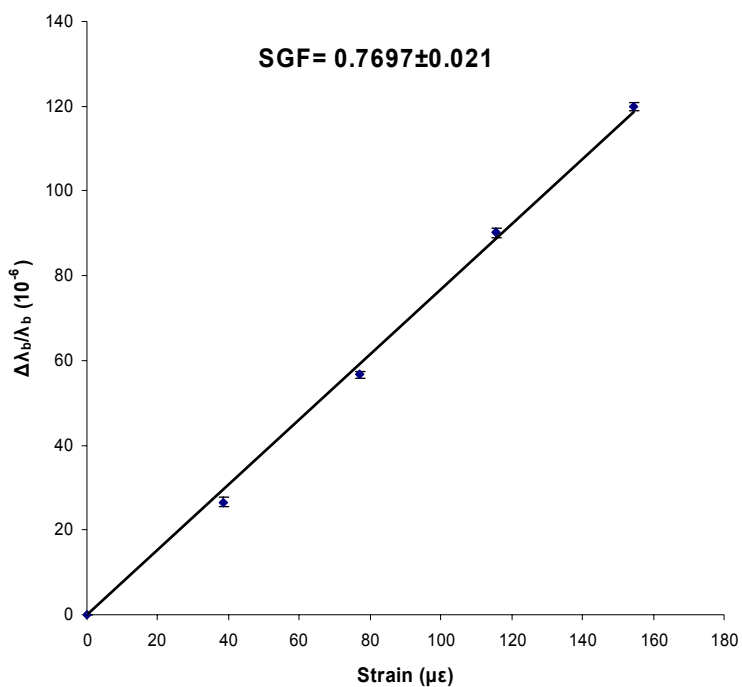


Figure 8.8 Plot of the fractional change in the center wavelength of the FBG as a function of the measured axial strain using the FPI strain gauge calibration setup. The solid line is a linear fit of the four data points. Note that the linear fit was forced to cross the origin.

## 8.5. Discussion

The main advantage of the FPI strain gauge calibrator is its self-referencing capability, meaning that calibration is not required other than knowledge of the wavelength of the FPI source, gauge length of the FPI strain gauge, and the observed number of fringes. In addition, the displacement can be measured at increments of half a wavelength of the optical source irrespective of the hysteresis and non-linearity of the piezoelectric actuator. The FPI strain gauge can be improved further by operating at a shorter wavelength. If the operating wavelength is reduced, the displacement and strain-fringe count resolution of the strain gauge calibrator will improve. For example, if the operating wavelength reduces to 680 nm from 1550 nm, the displacement increment will improve by 127%.

The SGF of the ESG and FBG were 2% and 4% lower, respectively, compared to the accepted values using the FPI strain gauge calibration setup. As stated earlier, a thin layer of plastic was used between the sensor holder clamps to protect the test sensor from damage. The clamps were then tightened along with the test sensor by two machines screws. However, the test sensor may still have moved due to the thin plastic. As a result, the displacement transfer between the piezoelectric actuator and the test sensor may have degraded. This means that a larger displacement from the actuator was required for a specific amount of strain resulting in a reduced SGF. Another source of error is the measurement of the gauge length. A change in 1mm for an 8 cm gauge length can introduce 1.3% error in the average SGF; however for the case of the ESG, a 1mm error in the gauge length should result in average SGF error close to 9%. Slips in the clamps

also introduce errors in the gauge length. In addition to mechanical errors, the resolution of the OSA introduces errors. The bandwidth resolution was given in the OSA datasheet; however, the resolution of the peak finder is not given. The bandwidth resolution is the ability of the OSA to distinguish between two peaks in the spectrum; however, there is only one peak for the FBG spectrum. If the bandwidth resolution of 0.07 nm is taken as the peak resolution, the SGF error should be much higher; the error in strain should be closer to  $58\mu\epsilon$  for 0.07 nm; obviously a better error was achieved by the OSA. Further repeatability measurements were done on the OSA. The results show that the absolute error in wavelength between the tunable laser and the measured wavelength of the OSA is 0.07 nm, however, difference error in wavelength is 0.002 nm, well within the repeatability of the tunable laser. For the case of ESG calibration, the width available for clamping was much wider than the FBG sensor and the Young's modulus of the ESG matrix and plastic layer are comparable resulting in a tighter grip. This will explain the larger SGF error for the FBG sensor as opposed to the ESG.

Since the actuator used to stretch the RSG is a piezoelectric, the strain range is limited compared to mechanical or electro-mechanical means. In this work, we were able to achieve  $\sim 400\mu\epsilon$  if the HV was set at 300V. Considering the thickness of the mono-morphic piezoelectric actuator, this result is decent. Further improvements in the range can be made using a mono-morphic actuator with a larger area or use a more resilient piezoceramic material or a bi-morphic piezoceramic actuator. In a bi-morphic piezoceramic actuator, the piezoceramic plate is bonded to both sides of the metallic plate, increasing the pulling power of the actuator.

In addition to range, the FPI strain gauge setup was fabricated from aluminum, a material that has significant temperature expansion coefficient. The material was chosen because it was easier to mill and suitable for the first prototype of the FPI strain gauge calibrator; in addition, the measurement time was short and at room temperature. In the future, a material with low temperature expansion coefficient such as steel should be used.

The calibration procedures for the FPI strain gauge calibrator are somewhat more complex compared to the cantilever beam method. The complexity comes from the fringe counting and the extra equipment necessary to operate the FPI strain gauge calibrator, namely the FPI, high voltage source, and piezoelectric actuator. The FPI strain gauge calibration process can be simplified by integration into a compact device controlled by a dedicated microprocessor or a computer. The computer would control the laser and the high voltage source using appropriate drivers, and a data acquisition system would process the resulting signals from the FPI and test sensor. Using the procedures described in the previous section, the processed signals from the FPI and test sensor would then be used to determine the SGF. The exact form of the hardware to interrogate the test sensor will depend on the sensing method: optical or electrical, and wavelength domain or time domain. However, as was shown in section 6, the method for determining the SGF of an ESG and FBG strain sensor were similar.

## 8.6. Conclusion

A non-destructive interferometric strain gauge calibration technique to measure the strain gauge factor of a FBG strain sensor and electric strain gauge (ESG) is demonstrated. The FPI strain gauge calibration setup utilizes a piezoelectric stretcher and a fiber optic Fabry-Perot interferometric displacement sensor. The piezoelectric actuator strains the sensor and the FPI measures the resulting displacement and strain. The results show that the SGF for ESG and boron/germanium doped FBG are  $2.047 \pm 0.033 \text{ V/V}/\mu\epsilon$  and  $0.77 \pm 0.021 \text{ m/m}/\mu\epsilon$ , respectively, or within 2% and 4% of accepted values, respectively. The FPI strain gauge calibration setup is non-destructive, compact, self-referencing, and avoids the non-linearity of the piezoelectric actuator. Such a setup is practical for calibrating the SGF of low modulus sensors. Further improvements in the FPI strain gauge calibrator can be made by using a short wavelength, reducing the thermal expansion coefficient of the base material, and increasing the range.

## 9. FIBER OPTIC SENSORS AND DISTRIBUTION METHODS

This chapter will give a limited overview of fiber optic sensor technology and fiber optic sensor distribution methods. More detail is given for the case of Coherent Optical Frequency Domain Reflectometry (C-OFDR).

### 9.1. Fiber optic sensors

Fiber optic sensors can be grouped in three main categories: intensity based, interferometric based, and diffractive based sensors (Yu, et al. 2004). An example of intensity based sensor is the fiber optic displacement sensor, microbend sensor, and the evanescent wave coupling sensor. The fiber optic displacement sensor (cf. Figure 9.1(a) and Chapter 5) was previously analyzed. The difference is that displacement is correlated with the drop in the optical power re-entering the optical fiber, using the transmittance function, after reflecting from surface R, instead of operating on the FPI displacement method. In the microbend loss mechanism, small deformation along the length of the fiber results in light leaking out of the fiber. This imperfection can be created mechanically by inserting a length of the optical fiber in a mechanism that creates small imperfections along the length of the fiber as shown in Figure 9.1(b) (Yu, et al. 2004). Microbend losses increase as pressure is applied across this mechanism, resulting in the drop of optical power at the output end of the fiber. Thus, the drop in the output can be correlated with the pressure applied to the optical fiber.

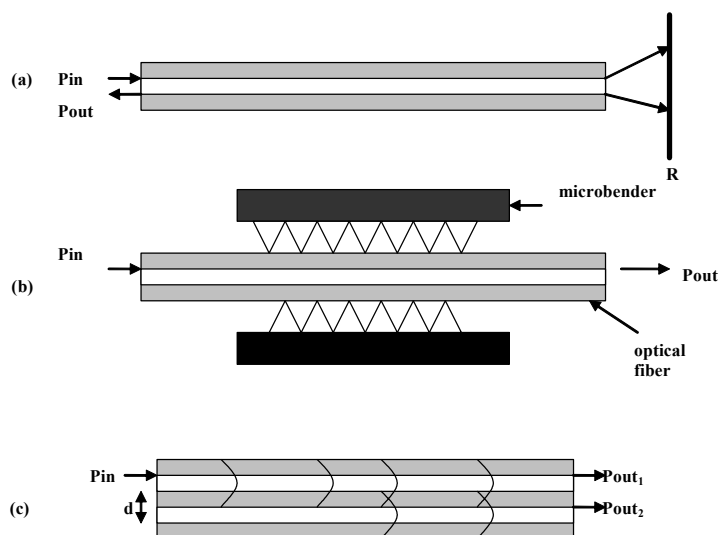


Figure 9.1 Intensity based fiber optic sensors: (a) Fiber optic displacement sensor, (b) Microbend optical sensor, and (c) Evanescent optical sensor

In the evanescent optical fiber, similar intensity drop can be created by varying the coupling between two optical fibers. Figure 9.1(c) shows an evanescent type optic sensor. The core of the optical fibers are closely spaced by distance  $d$ . The evanescent field of the input optical fiber extends into the second optical fiber, exciting modes in that optical fiber and transfer part of the power from optical fiber 2 to optical fiber 1. The amount of coupling between the optical fiber will be directly related to the spacing between the cores and pressure can be exerted between the optical fibers to increase the amount of coupling, similar to the microbend sensor. The advantage of the intensity based sensors is their cost structure which is cheap compared to the other optical techniques. In addition, the signal processing requirement is inexpensive and simpler. The disadvantage

of microbend sensor is the requirement of the reference source since a small fluctuation in the power can result in errors. Also, the measurement resolution is less favorable compared to other optical method such interferometric techniques.

The next class of optical fiber sensors is the interferometric type. As stated in Chapter 5, interference is created between two coherent beams, resulting in fringe patterns as the optical path length difference between the two beams is varied. Optical fiber interferometric sensors include Michelson, Fabry-Perot, Mach-Zhender, and polarimetric fiber interferometers as shown in Figure 9.2. The mechanism of an interferometer has previously been discussed. The difference between the types of interferometers depends whether the system is single pass or multiple pass, single arm or double arm. The Michelson and Fabry-Perot interferometers are double pass and multiple pass interferometers, respectively. This means that the light traverse at least twice through the interferometers. An example of a single pass is shown in Figure 9.2(b) for the Mach-Zhender (Yu, et al. 2004). Multiple pass interferometers are more sensitive than a single pass system because the optical path difference, therefore the phase difference, accumulates for each pass. For a single pass system, the observed fringes are spaced a wavelength part, while for a multiple pass system, the spacing is half a wavelength. An interesting type of interferometer is the polarization based sensor. For the polarization interferometer, light is launched (usually at 45 degrees to the optical axis of the fiber) into a polarization maintaining fiber (PMF) at a polarization angle given by the polarizer (P). The perturbation (or measured parameter) is forced to act on one of the polarization states, resulting in a phase difference. The analyzer then interfere the two polarization

states of the fiber, resulting in a phase difference directly related to measured perturbation. The advantage of interferometers compared to intensity based sensors is their high resolution but the cost structure is moderately higher. In addition, the signal processing requirement is also moderate, basically requiring an oscilloscope to measure the resulting fringes and at worst an optical spectrum analyzer for the FPI. The disadvantages are their non-linearity and are prone to be vibration and temperature sensitive.

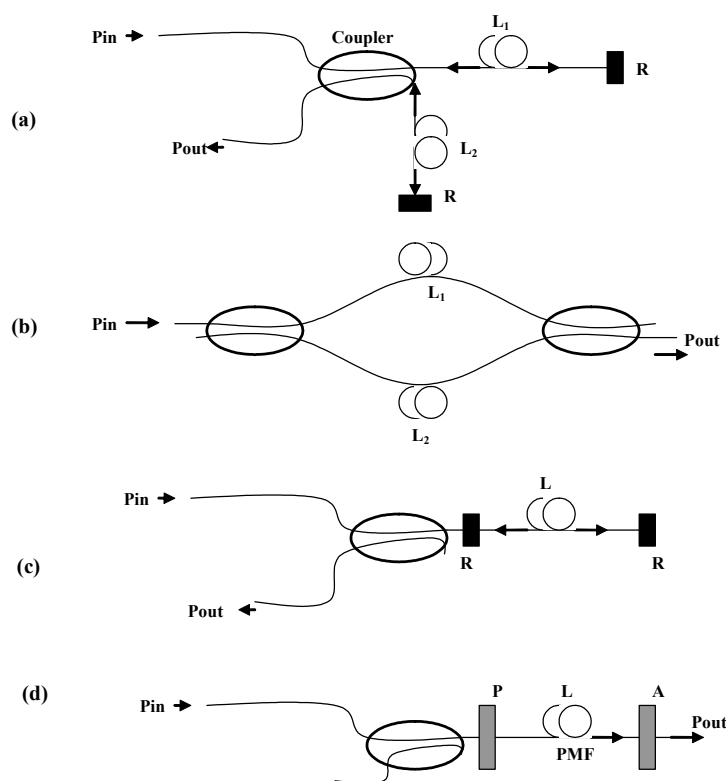


Figure 9.2 Types of interferometers: (a) Michelson, (b) Mach-Zhender, (c) Fabry-Perot, and (d) Polarization based interferometer.

The final class of optical sensing technique is the diffractive based sensor. A prime example of a diffractive sensor is the fiber Bragg grating (FBG). The principle operation of the FBG was previously discussed. In this section, the type of interrogation of the FBG is a primary interest. There are several techniques that are currently employed to determine the wavelength shift of a FBG due to changes in the index and period of the grating. Figure 9.3(a)(b) shows the cases for interrogating a FBG sensor using an edge filter technique and a FPI. In the edge technique, a filter, with a linearly varying transmittance as a function of wavelength, is used. In this case, the change in the Bragg wavelength of the FBG sensor will be directly related to the changes in the transmittance, therefore, will be directly related to changes in the optical output of the filter. For the case of the FPI interrogation, a FPI operating in the same range as the FBG sensor is used. Typically, a high finesse FPI with a long free spectral range ( $\sim 40\text{nm}$ ) is used. The FPI scans the FBG sensor, in this case, operating in the transmission. When the FPI matches the Bragg wavelength of the FBG sensor, the optical output of the matched FBG maximizes. The FPI scans and locks on Bragg wavelength of the FBG sensor using a feedback system and a piezoelectric stretcher. The voltage input to the piezoelectric actuator is correlated (calibrated) with the FPI so the changes the Bragg wavelength of the FBG sensor can be determined. A matched FBG (operating the same range as the FBG sensor) can be used in place of the FPI. The rest of the system is similar to the FPI system; however, the matched FBG operates in the reflective mode and an extra coupler is needed. Other techniques used to interrogate FBG include using an un-balanced Mach-Zehnder as shown in Figure 9.3(c).

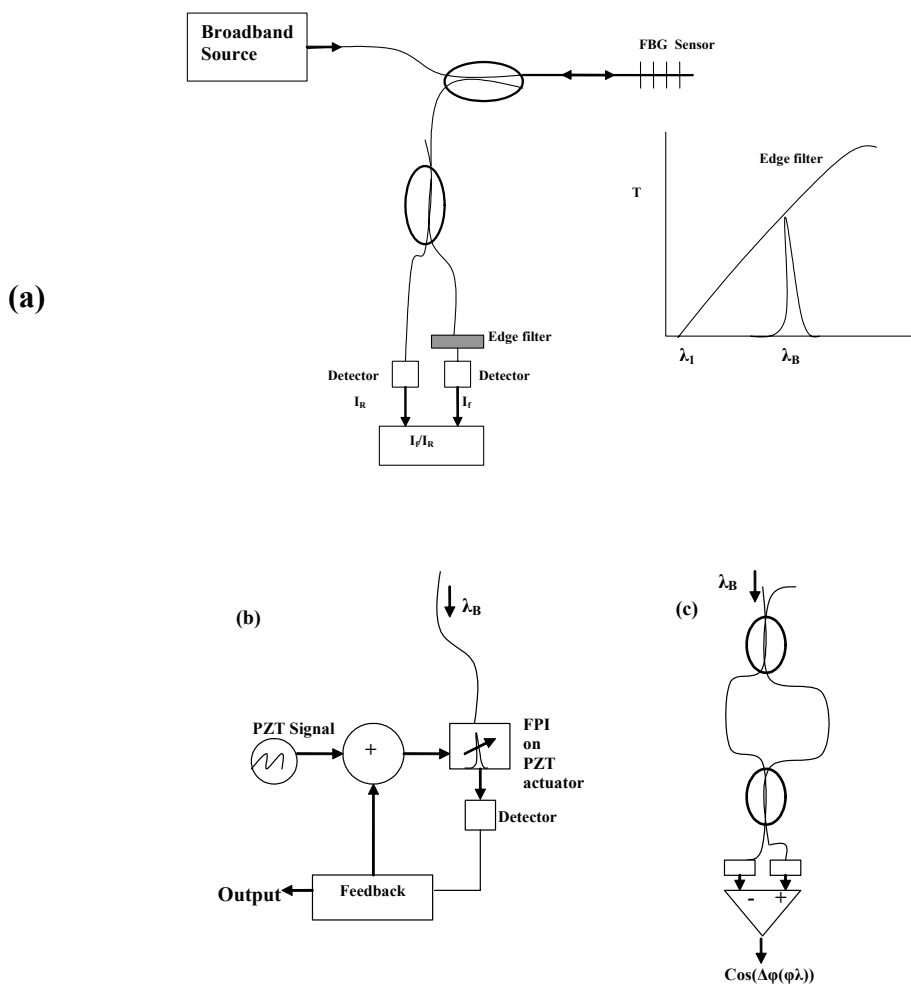


Figure 9.3 Interrogation of fiber Bragg grating (FBG) sensor using (a) edge filter, (b) FPI, and (c) unbalanced Michelson.

This technique is somewhat similar to the Optical Frequency Domain Reflectometry technique that will be discussed later in this section. In the un-balanced Mach-Zehnder technique, path difference is set between the reference arm and test arm of the interferometer. A change in the wavelength of the interferometer will introduce a phase change, similar to a change in the optical path difference. This means that changes in the

Bragg wavelength of the FBG sensor are converted to a phase change. Very high resolution can be achieved using an un-balanced Mach-Zehnder. Compared to the other sensing method, diffractive optical sensor offer linearity with respect to the measurement, however, the initial capital cost to fabricate the gratings are high, and the signal processing hardware can be expensive. Most of the interrogation expenses occur when optical spectrum analyzers and laser sources are employed; it is much more cost effective to use diffractive devices to recover the wavelength information and LEDs as sources. The main attraction to diffractive based sensors is its ability to be interrogated into the current optical communication hardware and systems.

## **9.2. Distributed optical sensing techniques**

The main advantage of optical sensors compared to electric sensors is its ability to be distributed and multiplexed along single or several optical fiber lines. Electrical sensor typically require a lead for each sensor, thus can be cumbersome when large amount sensing is required to measure a wide area. There two types of distribution of optical fiber: continuous distribution and quasi-distribution. In a continuous distribution of optical fiber sensors, the entire length of the optical fiber is a sensing region. For a quasi-distributed optical fiber sensor, discrete points along the fiber serve as the sensing region. There are two main techniques for continuous distribution optical fiber sensors: optical time domain reflectometry (OTDR), and optical frequency domain reflectometry (OFDR). For the case of quasi-distributed optical fiber includes: optical coherence multiplexing (OCM), time division multiplexing (TDM), wavelength division multiplexing (WDM), and OFDR can be used. TDM operates on the same principle as

OTDR. Figure 9.4 shows the case for OTDR and TDM. For the case of OTDR, the power at the detector can be shown to be (Yu, et al. 2004):

$$P_r(t) = P_0 R(z) e^{-\int_0^z 2\alpha(z) dz} \quad (9.1)$$

Where  $z$  is time dependent:

$$z = \frac{tc}{2n} \quad (9.2)$$

The reflectance  $R(z)$  can be due to artificial abnormalities along the length of the optical fiber or continuous reflections due to Rayleigh backscattering. Rayleigh backscattering is due to small variations in the refractive index of the optical fiber. In addition to backscattering, there is also loss due to attenuation of optical fiber as given by the attenuation coefficient  $\alpha(z)$ . The minimum detectable length of the optical fiber is directly related to the width of the pulse signal ( $\tau$ ). For example, if the pulse width is 1ns, the minimum detectable length is 10 cm, assuming an index of 1.45 for the optical fiber. This means the bandwidth of the receiver has to be at least 2Ghz using Nyquist criterion. It can readily be seen that OTDR system main disadvantage is the high bandwidth requirements of the signal processing system. The TDM version is similar to the OTDR except the reflections are discrete. Typically, the reflections are from reflective type optical devices such as FBGs. Each optical sensor signal will be displaced in time and fast optical signal processing can then be done to pick out each reflection separately. For the case of distributed FBG sensors, the recovered pulse can then be sent to an optical

spectrum analyzer or some type of dispersion element or the method discussed above for FBG interrogation.

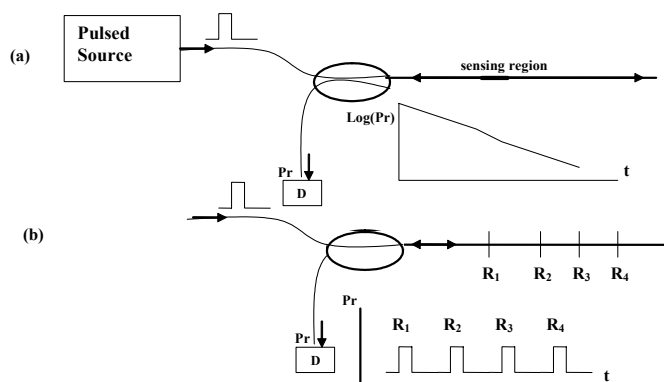


Figure 9.4 Optical time domain reflectometry for (a) continuous sensing of optical sensors (OTDR) and (b) discrete sensing of optical sensors (Time Division Multiplexing).

The next two types of quasi-distribution methods are wavelength division multiplexing and coherent multiplexing. In a WDM system, each optical sensor is given a distinct wavelength. The resulting optical signal will then be a composite of several wavelength and dispersive type element can then be used to wavelength de-multiplex and recover a particular sensor. Finally, in coherent multiplexing, a low coherence source is used to interrogate an array of interferometers. Figure 9.5(b) shows the case for an array of FPI. Each FPI is given a different optical length or cavity spacing,  $d_i$ . The resulting signal from the array is then scanned by a FPI. When the optical path length of the scanning FPI matches a particular FPI sensor, constructive interference will occur between the scanning FPI and the particular FPI, indicating the cavity spacing for the FPI. Each FPI must differ from the adjacent FPI by at least the coherent length of the

source so that they do not interfere with each other. The main advantage of WDM is the low bandwidth requirement of the signal processing compared to OTDR and its main disadvantage is its limited multiplexing ability since each optical sensor will be required to have a dedicated wavelength. This effectively limits the number of sensors to be multiplexed.

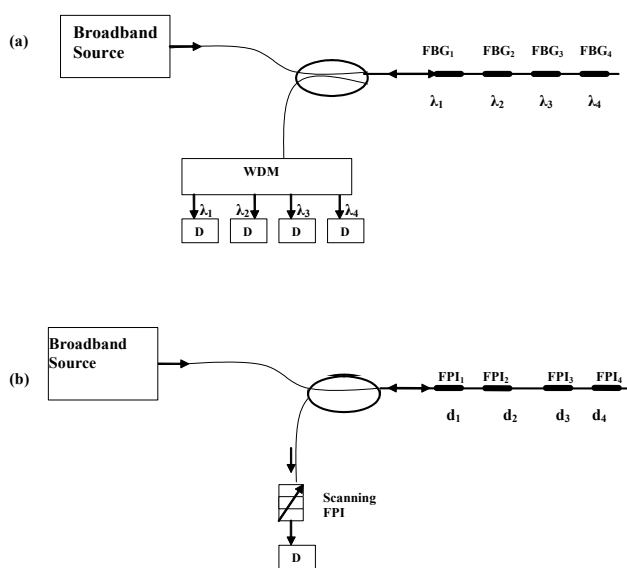


Figure 9.5 Examples of quasi-distributed sensors using (a) wavelength division multiplexing (WDM) for FBGs and (b) coherent multiplexing for fiber optic Fabry-Perot interferometers (FPI).

The next type of distributing sensing technique is the coherent optical frequency domain reflectometry (C-OFDR). C-OFDR was originally envisioned to replace OTDR due to its high spatial resolution possibilities. OFDR is the complement of OTDR. Instead of working in the time domain as OTDR, OFDR operates in the Fourier domain. OFDR technique is not a new technique, it has been around since the early 1980's and incoherent OFDR has been around much longer; the concept of I-OFDR is used in

RADAR. However, C-OFDR is unable to effectively measure Rayleigh back-scattering compared to OTDR, and the coherence and stability requirements of the laser source are also stringent. Due to the availability of long coherence length semiconductor lasers, C-OFDR is getting a second look for use in the distributed sensing realm. As shown in Figure 9.6, a high coherent laser source wavelength scans an interferometer, in this case, a Michelson.

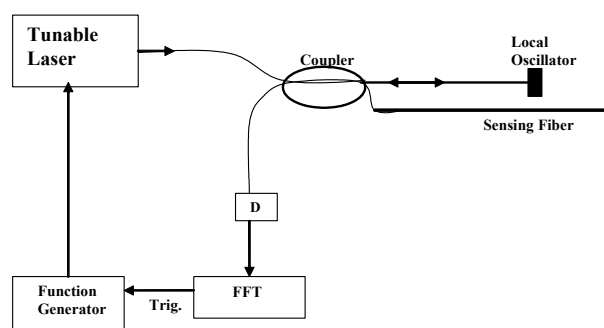


Figure 9.6 Distributed sensing using optical frequency domain reflectometry (C-OFDR).

One arm of the Michelson serves as a reference length, while the second arm, is the sensing optical fiber. The two signals from the arm combine. If the laser source is scanned as a function of wavelength, a composite interference pattern at the detector will be observed. This interference pattern is continuously modulated, where the frequency of modulation is directly related to optical path difference between the tip of the fiber and at particular backscattering position along the fiber. The backscattering can be due to Rayleigh backscattering or discrete reflective points. Taking the Fourier transform of the modulated interference pattern will separate each frequency component in the Fourier

domain, thus the reflectivity as a function of position can be determined similar to OTDR. Assuming most of the reflection in the sensing arm is due to Rayleigh scattering, the field from the reference is in the form:

$$A_s(\lambda, x) = R(x)e^{j2\frac{2\pi}{\lambda}x}, \quad (9.3)$$

where  $\lambda$  is wavelength of the source,  $R(x)$  is the field backscattering due Rayleigh scattering at position  $x$ , and  $L$  is the length of the sensing region. Likewise for the reference length:

$$A_r(\lambda) = A_1e^{j2\frac{2\pi}{\lambda}L} \quad (9.4)$$

Adding the reference and scattering due Rayleigh:

$$I(\lambda) = \left| \left( A_1e^{j2\frac{2\pi}{\lambda}L} + R(x)e^{j2\frac{2\pi}{\lambda}x} \right) \right|^2 \quad (9.5)$$

The interference term (correlation term) is then given by:

$$I_C(\lambda, x) = A_1R(x) \cos\left(\frac{2\pi}{\lambda}(2(L-x))\right) \quad (9.6)$$

Eq. 9.6 is integrated along the length of the sensing region to determine the composite interference signal. As the wavelength is varied, fringes patterns will be observed. Taking the Fourier transform (wavelength range) of Eq. 9.6 recovers the reflectance due to Rayleigh scattering at position  $x$ . The frequency of the fringe due to interference at position  $x$  is directly related to the optical path difference ( $L-x$ ), where the period of the fringe is given by the free spectral range:

$$\Delta\lambda_x = \frac{\lambda^2}{2n(L-x)} \quad (9.7)$$

Likewise, the resolution of the system is also given by the free spectral range:

$$\Delta x = \frac{\lambda^2}{2n\Delta\lambda} \quad (9.8)$$

where  $\Delta\lambda$  is the wavelength tuning range of the tunable laser. If the tuning range is 40nm, the resolution of the system is 20 $\mu$ m at 1550 nm and an index of 1.45. Similarly, the sensing range of the C-OFDR is directly related to the effective resolution wavelength resolution of the laser source:

$$L = \frac{\lambda^2}{2n\Delta\lambda_{x=0}} \quad , \quad (9.9)$$

where  $\Delta\lambda_{x=0}$  is the period of the fringes for a path difference of L. For the case of sensing range, if the resolution of the laser is 0.001pm, the sensing range of the C-OFDR system is 82 cm at 1550 nm with an index at 1.45. In addition, the tunable laser is usually ramped linearly in time; in this case, the bandwidth in Hertz (cycles/sec) is then given by:

$$f_{BW} = \frac{\Delta\lambda}{\Delta\lambda_{x=0} \cdot t_s} \quad , \quad (9.10)$$

where  $t_s$  is the time required to scan  $\Delta\lambda$ . The versatility of OFDR system is the ability to arbitrarily control the bandwidth. As shown in Eq. 9.10, the bandwidth can be controlled by either varying  $\Delta\lambda$  or the ramp time. However, the constraints will come from the specific application and the type of sensors used. For example, if the sensors are FBGs, the strain range or the amount of the Bragg wavelength shift required will determine  $\Delta\lambda$ . Also, if dynamic strain measurements are being performed,  $t_s$  will depend on the maximum frequency of the vibration (see Chapter 12).

Overall, C-OFDR can offer high resolution measurement compared to OTDR and the number of optical sensors able to be distributed can be very large since the interrogation is spatially dependent and not wavelength dependent like WDM systems. The main draw back of C-OFDR is the coherence requirement for the tunable laser. The power spectrum density describes the coherence requirement of the tunable laser and is given by the auto-correlation of the signal from detector which happens to be proportional to the irradiance. Ignoring shot noise and Rayleigh scattering, if the coherence of the laser is given by  $\tau_c$ , the power spectrum density of the signal from the detector resulting from interference between the reference arm and a reflector at point  $x_0$  on the test arm is given by Yu, et al. 2004:

$$\begin{aligned}
 PSF(f) = & (1 + R)^2 \delta(f) + 2R \cdot e^{-\frac{-2\tau_0}{\tau_c}} \delta(f - f_b) + \frac{2R\tau_c}{1 + \pi^2\tau_c^2(f - f_b)} \\
 & \times \left[ 1 - e^{-\frac{2\tau_0}{\tau_c}} \cdot \left\{ \cos(2\pi(f - f_b)\tau_0) + \frac{\sin(2\pi(f - f_b)\tau_0)}{\pi\tau_c(f - f_b)} \right\} \right]
 \end{aligned} \tag{9.11}$$

Where  $R$  is back reflectance of the reflector a position  $x_0$ ,  $f_b$  is the beat frequency of the interference, and  $\tau_0$  is the resulting time delay as given by the optical path difference divided by the speed of light. If the slope of the ramp is given by  $\gamma$ , the beat frequency in Hertz is given by  $\gamma\tau_0$ . The first component of Eq. 9.10 is a DC term and the second component is a function of the beat frequency, while the third term is continuous and a function of the coherence time and the time delay. As shown in Eq. 9.10, exceeding the coherence length of the laser result in the attenuation and broadening of the interference beat as shown by the third component (Yu, et al. 2004). The coherent requirement is not a

large constraint since today's semiconductor laser sources currently can achieve linewidths of 1 kHz, resulting in coherence lengths of hundreds of meters. The main concern in C-OFDR is the stability during the tuning process. The laser must be able to be tuning smoothly and without jitters. Jitters in the tuning mechanism introduce effects similar to phase as shown in Chapter 10 of this work.

## 10. MODELING OF FBGA AND C-OFDR SYSTEMS

This chapter discusses the implementation of C-OFDR interrogation of a FBGA system (discrete systems). The first practical implementation of FBGA/C-OFDR system was conducted by Froggatt (1998) at NASA Langley Research Center and later developed by Luna Innovation (Childers, et al. 2001) of Blacksburg, Virginia. This chapter focuses on the use of Transfer Matrices in FBGA/C-OFDR system. To the best of the author's knowledge, the use of Transfer Matrices in FBGA/C-OFDR systems is an original contribution by the author to the technology in the public literature. This chapter focuses on the design of a 3 element, 15 cm FBGA/C-OFDR system using the OSS software described in Chapter 2, and testing of the system using the cantilever beam method and three co-located resistive strain gauges to verify FBGA axial strain results.

### 10.1. Modeling FBGA system using diffractive optics

Figure 10.1 shows C-OFDR interrogation of N-element FBGA system with a backend reference reflector. A coherent source scans the FBGA as a function of wavelength. Physically, the reflections from each FBG in the array interfere with the reflection from the reference reflector. The net effect is a composite modulation of the FBGs, where beat frequencies of the modulation are directly related to the position of the FBGs with respect to the reference reflector. There are also interferences between the FBGs resulting in cavity interferences. Taking the Fourier transform of the FBGA system signal spatially separates out each FBG in the array. A band-pass filter, centered at a particular beat frequency, is then used to extract the corresponding FBG signal from the

Fourier transform. This is followed by an inverse Fourier transform to recover the FBG spectrums.

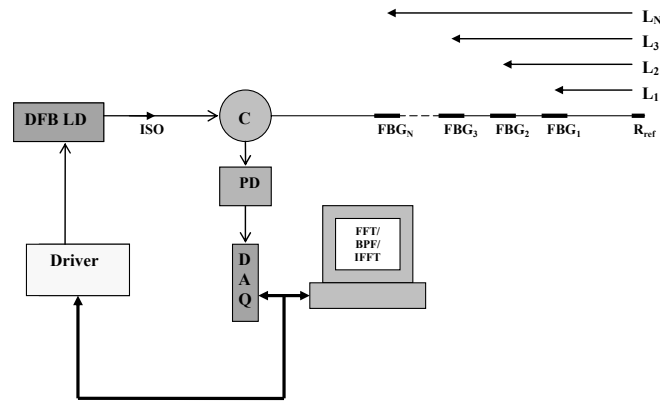


Figure 10.1 C-OFDR interrogation of an N-element FBGA system.

Figure 10.2 shows a close up model of a FBGA system with a backend reflector. The following analysis is a modification of Childers, et al. (2001) method for modeling the FBGA system as simple phase gratings. Childers, et al. (2001) assumed low reflectivity gratings to model the gratings as simple phase element, where the field contributions from the differential elements are added up to get the resultant field of the grating:

$$E(\lambda) = \int_{L-\frac{l}{2}}^{L+\frac{l}{2}} e^{i\frac{2\pi}{\lambda}(2x)} e^{i\Delta n \cos\left(2\pi\frac{x}{\Lambda}\right)} dx, \quad (10.1)$$

where  $l$  is the width of a single grating,  $L$  is the distance from the reference reflector,  $\Lambda$  is period of the grating, and  $\Delta n$  is the magnitude of refractive index change. In the above analysis, the plane waves are weighted by the phase contribution of the phase grating,

effectively, the Fourier transform of the phase grating; in addition, the interaction between the differential elements are ignored.

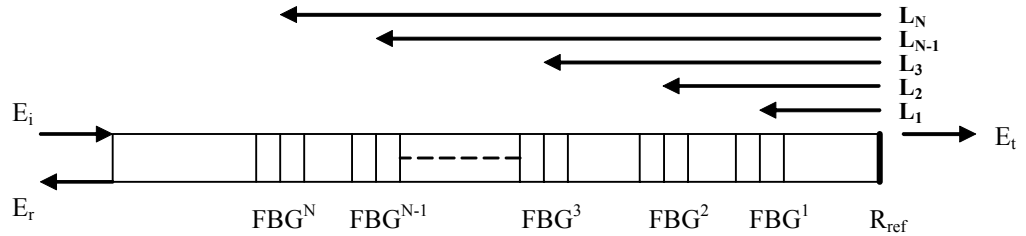


Figure 10.2 A model of a N-element fiber Bragg grating array with a backend reference reflector.

Eq.10.1 can be further simplified if the index modulation is assumed small such that  $e^\varepsilon \approx 1 + \varepsilon$  :

$$E(\lambda) = \int \Pi\left(\frac{x-2L}{2l}\right) \left[ 1 + i\Delta n \cos\left(\frac{x}{\Lambda} 2\pi\right) \right] e^{i\frac{2\pi}{\lambda}(2x)} dx \quad (10.2)$$

We can see from equation 10.2 that the resultant field is the Fourier transform of the variation of refractive index bounded by length of the phase grating, represented by the Rectangular ( $\Pi(x)$ ) function (Goodman 1996, Childers 2001):

$$E(\lambda) = F\left\{ \Pi\left(\frac{x-2L}{2l}\right) \right\} + F\left\{ i\Delta n \Pi\left(\frac{x-2L}{2l}\right) \cos\left(2\pi \frac{x}{\Lambda}\right) \right\} \quad (10.3)$$

The latter of Eq. 10.3 is signal of interest and is a convolution between the Fourier transform of sinc function and the Fourier transform of a cosine function. If the first component of Eq. 10.3 and the multiplication constants are ignored, the resultant field is then given by:

$$E(\lambda) = e^{-j2\pi(2L)(1/\lambda - 1/2\Lambda)} \text{SINC}\left(\frac{1/\lambda - 1/2\Lambda}{1/2l}\right) \quad (10.4)$$

Adding the contribution from the broadband reflector and subsequent gratings, the power observed at the detector from an FBGA and reflector is proportional to the following:

$$\begin{aligned} I(\lambda) &\sim \left| \sqrt{R_{ref}} + \sum_i e^{-j2\pi(2L)(1/\lambda - 1/2\Lambda)} \text{SINC}\left(\frac{1/\lambda - 1/2\Lambda_i}{1/2l_i}\right) \right|^2 \\ &= R_{ref} + 2\sqrt{R_{ref}} \sum_i \cos(2\pi(2L_i)(1/\lambda - 1/2\Lambda_i)) \text{SINC}\left(\frac{1/\lambda - 1/2\Lambda_i}{1/2l_i}\right) + \sum_i \text{SINC}^2\left(\frac{1/\lambda - 1/2\Lambda_i}{1/2l_i}\right) \end{aligned} \quad (10.5)$$

The second component of Eq. 10.5 is the useful signal but the latter component of Eq. 10.5 is not modulated, therefore, does not offer methods to distinguish between the FBGs. Ignoring the constant phase terms, extracting the second component, and the effective refractive index gives a signal that is proportional to the observed irradiance at the detector:

$$\begin{aligned} I_{R_{ref}-FBG}(\lambda) &\sim \sqrt{R_{ref}} \sum_i \cos\left(\frac{2\pi}{\lambda}(2nL_i)\right) \text{SINC}\left(\frac{n/\lambda - n/2\Lambda_i}{1/2l_i}\right), \\ &\sim \sum_i^N \sqrt{R_{ref} \cdot FBG_i(\lambda)} \cdot \cos\left(\frac{2\pi}{\lambda}(2nL_i)\right) \end{aligned} \quad (10.6)$$

where  $FBG(\lambda)$  can also be the grating reflectance given by square of Eq. 4.26.

## 10.2. Cavity interferences

The above analysis does not include cavity interferences or interferences between the gratings. Assuming low reflectivity FBGs, the cavity interferences contribution is proportional to:

$$\begin{aligned}
I_c(\lambda) &\sim \sum_i^N \sum_{j>i}^N \sqrt{FBG_i(\lambda) \cdot FBG_j(\lambda)} \cdot \cos\left(\frac{2\pi}{\lambda}(2n(L_i - L_j))\right), \\
&= C(N,2) \cdot FBG(\lambda) \cdot \cos\left(\frac{2\pi}{\lambda}(2n(L_i - L_j))\right)
\end{aligned} \tag{10.7}$$

where C is the combination of 2 elements that can range from 1 to N:

$$C(N, k) = \frac{N!}{k!(N-k)!} \tag{10.8}$$

The latter of Eq. 10.7 assumes the gratings are identical. It is interesting to note the effects of Eq 10.8 on the magnitude of the cavity interferences as a function of optical path length ( $L_i-L_j$ ). Assuming a 4-element FBGA with equally spaced identical FBGs, there are only three combinations that results in distinct optical differences (cf. Figure 10.1):

$$\begin{aligned}
i = 1 &: L_1 - L_2, L_2 - L_3, L_3 - L_4 \\
i = 2 &: L_1 - L_3, L_2 - L_4 \\
i = 3 &: L_1 - L_4
\end{aligned} \tag{10.9}$$

The effect of having equal cavity spacings and identical FBGs is that the sum of the cavity interferences having the same path differences will add up constructively. In the case above, the interference produced by  $i=1$  path difference will be three times larger  $i=3$ . The resulting trend is linearly decreasing interference peak magnitudes in the Fourier domain. In addition to linear drop of cavity interferences in the Fourier domain, it can readily be seen that the cavity interferences is the convolution of two rectangular functions, resulting in a triangle shape for the cavity interference peaks in the Fourier

domain, where the width of the base of the triangle is twice that of the rectangular interference peaks.

### **10.3. Transfer Matrix Approach**

In this work, we demonstrate the modeling-testing cycle of a FBGA/C-OFDR system with the aid of the transfer matrix approach. In the first part of this work, we demonstrate the modeling, design, and simulation of a three-element, 15.3 cm FBGA/C-OFDR system using transfer matrices. Compared to the previous techniques discussed, the transfer matrix method allows a system wide approach to modeling the FBGA/C-OFDR system. An elemental transfer matrix represents the optical and geometrical characteristics of a single element in the FBGA system. The response of the entire FBGA system is then determined simply by multiplying all the elemental transfer matrices in the proper order. The advantage of this approach is that any optical device can efficiently be incorporated if its transfer matrix is known. Unlike the two-beam or phase grating modeling techniques, higher interferences will also be taken into account and the reflectance of the FBGA/C-OFDR system can be determined directly. In this work, higher order interferences will be defined as interference resulting from multiple pass through the FBGA system and interference between the beats.

The FBGA system design was imprinted into the core of a Boron/Germanium co-doped photosensitive fiber using a phase mask and a doubled frequency Argon ion laser operating in the UV (244 nm) as shown in Chapter 4. The FBGA/C-OFDR system was then tested on a 75 cm aluminum cantilever beam. Three electric strain gauges were then

used to independently verify the strain measurements from the FBGA at various displacements of the cantilever beam.

Finally, in the discussion section, we compare experimental and the simulation results. With the aid of the simulation software, we will show that the tuning characteristic of the tunable laser used is the main source of error.

### 10.3.1. FBGA and C-OFDR

The transfer matrix  $\mathbf{T}$  can be considered as a multiplication of individual **FBGs**, reflector,  $\mathbf{R}_{ref}$ , and phase,  $\mathbf{P}$ , transfer matrices. For a FBGA with a Fresnel reflector at the tip, the transfer matrix of the FBGA system is given by:

$$T = [R_{ref}] [P] [FBG^1] [P] [FBG^2] [P] [FBG^3] \dots [FBG^{N-1}] [P] [FBG^N], \quad (10.10)$$

Where:

$$P = \exp \begin{bmatrix} -\frac{4\pi n}{\lambda} l_p & 0 \\ 0 & \frac{4\pi n}{\lambda} l_p \end{bmatrix}, \quad (10.11)$$

$$R_{ref} = \frac{1}{t} \begin{bmatrix} r & 0 \\ 0 & -r \end{bmatrix}, \quad (10.12)$$

$$r = \frac{n-1}{n+1}, \quad (10.13)$$

$$t = \frac{2n}{n+1}, \quad (10.14)$$

The FBGs are all identical, where the transfer matrix is given by Eq. 4.28. The FBGA system reflectance ( $R(\lambda)$ ) is given by:

$$R(\lambda) = \left| \frac{T_{21}(\lambda)}{T_{11}(\lambda)} \right|^2, \quad (10.15)$$

where the  $\mathbf{T}$  is the final FBGA system transfer matrix. In a double pass configuration, the beat frequencies produced by the interference between the FBGs and the reference reflector are directly related to the relative position ( $L_i$ ) of the individual FBGs with respect to the reference reflector:

$$f_i = \frac{2nL_i}{\lambda^2} \quad (10.16)$$

In addition to the interference between the FBGs and the reflector, there are also interferences between the FBGs, resulting in cavity interferences. The resulting beat frequency produced by the cavity interference is then given by:

$$f_{ij} = \frac{2n|L_i - L_j|}{\lambda^2} \quad (10.17)$$

Furthermore, higher order interferences can result from multiple pass through the system and interferences between the beats. Figure 10.3 shows the block diagram implementation of a Sensor Array Processor (SAP). The SAP orchestrates the communication between the main processor and also assembles the sensor array, in this case, the FBGA system. The basic function is as follows: For the case of the FBGA system, each transfer matrix for each device is stored in a library. The optical devices that are currently modeled include: sources, detectors, reflectors, coupler, gratings, and phase

delays. The transfer matrices are then assembled to form the FBGA system. Boundary conditions are then imposed, the resulting reflectance and transmittance of the FBGA system is then determined, and the results passed back to the main processor.

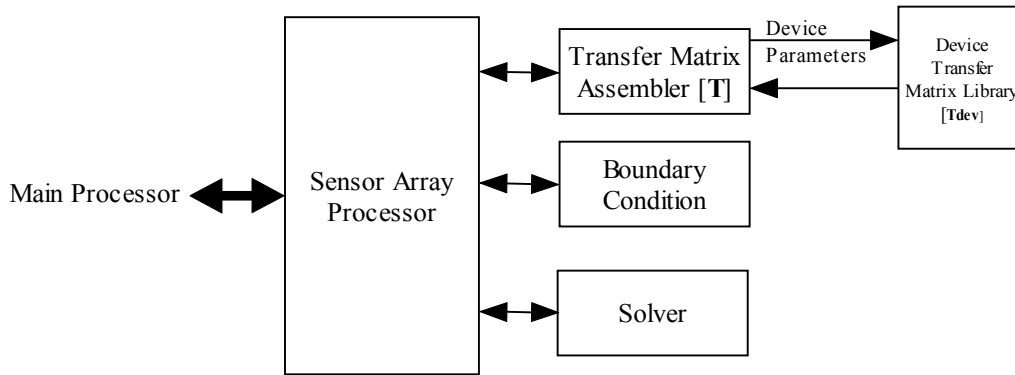


Figure 10.3 Block diagram implementation of Sensor Process for transfer matrix modeled devices.

To recover individual FBG spectrum using C-OFDR, the Fourier transform of the FBGA reflectance spectrum is taken. A simple band-pass filter, represented by a rectangular window (REC) of width  $W$  and centered at a desired beat frequency ( $f_i$ ), is then used to extract desired FBG signal from the Fourier spectrum. Once extracted, this information is then inverse Fourier transformed to recover the wavelength information of the desired FBG or in a mathematical form given by:

$$FBG_i(\lambda) = \left| F^{-1} \left\{ F(R(\lambda)) REC \left( \frac{f - f_i}{W} \right) \right\} \right|, \quad REC(x) = \begin{cases} 1 & |x| < \frac{1}{2} \\ 0 & otherwise \end{cases}, \quad (10.18)$$

where  $F(\cdot)$  and  $F^{-1}(\cdot)$  are the Fourier and inverse Fourier transform, respectively. The required bandwidth of the band-pass filter is inversely related to the wavelength bandwidth of the FBGs:

$$W \geq \frac{1}{\Delta\lambda} \quad (10.19)$$

For a low reflectance FBG, the wavelength bandwidth is directly given by free spectral range and the effective refractive index:

$$\Delta\lambda = \frac{\lambda^2}{2nl}, \quad (10.20)$$

It is possible for the cavity interferences to super impose onto FBG-reflector interferences when their corresponding beat frequencies are equal  $f_i = f_{ij}$ , resulting in the distortion of the recovered FBG spectrums. Several techniques have been implemented to eliminate this distorting. The first technique is to reduce the reflectance of the FBGs to a level that minimizes the cavity interferences. The second method is to down shift the cavity interferences to a lower frequency band such that  $L_1 > |L_N - L_1|$  (Froggatt, et al. 1998). A third technique, simulated in a prior paper (Abdi, et al. 2004), is to actively subtract the cavity interferences directly from the overall FBGA system interference signal. A fourth technique is to design the FBGA system such that the cavity interferences and the FBG-reflector interferences do not overlap. The latter is the technique used in this work. Figure 10.4 shows the block diagram implementation of the Signal Processor for the FBGA/C-OFDR system. The Signal processor orchestrates the communication between the Main Processor and the signal processing routines outlined for the FBGA/C-OFDR system.

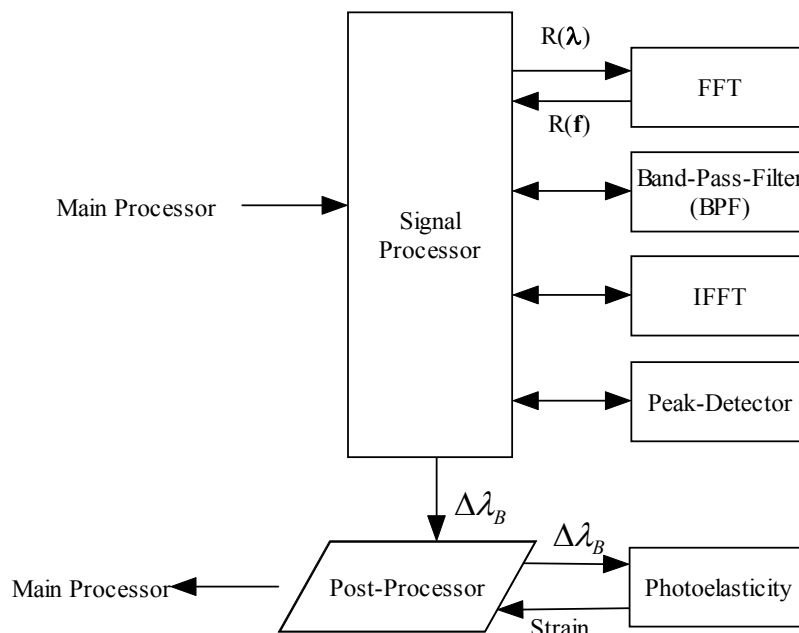


Figure 10.4 Block diagram implementation of the Signal Processor for C-OFDR system

The outline of the Signal Processor is as follows: The FBGA system reflectance, as calculated by the SAP, is Fourier transformed and the resulting Fourier transform then goes through a bandpass filter as outlined in this section. An inverse Fourier Transform is then used to recover the reflectance information for chosen FBG. A peak detector then determines the changes in the Bragg wavelength for the FBG. The photoelastic relationship from Chapter 5 is then used to determine the observed strain at the FBG.

### 10.3.2. FBGA/C-OFDR design and simulation

The Tunics-BT tunable laser has a minimum wavelength scan increments of 1 pm and repeatability of  $\pm 10$  pm. The optical path difference that corresponds to 1 pm period is 83 cm at 1550 nm using the free spectral range equation and a refractive index of 1.45. The maximum possible length of the FBGA system is 41.5 cm using the Nyquist criteria.

In the Nyquist criteria, a waveform is reproduced exactly if the sampling rate is twice the highest frequency component of the waveform. To be conservative, the length of the FBGA system was set at 20.8 cm or one-half the maximum length. The length of the FBGA was chosen to be around 15 cm, allowing a 5.8 cm margin to optimize the position of the reference reflector. The criterion for the optimum position of the reflector is so that cavity interferences do not overlap with the reflector-FBG interferences. The maximum number of FBGs possible for a 15 cm FBGA is limited by cavity interferences and the width of each FBG. The phase mask used allowed a maximum length of 1.3 cm for the FBG; a three-element FBGA was the best choice. The software program was used to determine optimum reflectance for each FBG in the array and the reference reflector position. It was determined that the optimum position of the reflector was between 2 cm and 4 cm from the FBGA to prevent an overlap. This actually predictable for evenly spaced FBGA; to prevent an overlap, the optimum reference length is one-half of the spacing between FBGs, in this case, 2.85 cm. The reflectance of each FBG in the array was set at 1% with a 4% reflectance for the reference reflector at the tip of the fiber. The reflectance of the FBGs were chosen so that the FBG-reflector interferences were comparable or larger in magnitude than the cavity interferences. However, this is not critical since the cavity interferences and the FBG-reflector interferences do not overlap by design. Figure 10.5(a) shows the final design layout. The final length of the FBGA is 15.3 cm and contains three FBGs of width 1.3 cm and 128 pm bandwidth. Each FBG is separated by 5.5 cm and with the reflectance reflector positioned 3.7 cm from the FBGA. Figure 10.5(b)(c) shows the resulting interference signal from the FBGA system in the

wavelength and Fourier domain. The range of the Fourier transform shown in Figure 10.5(c) is with respect to the reference reflector position. The first, third, and fifth peaks

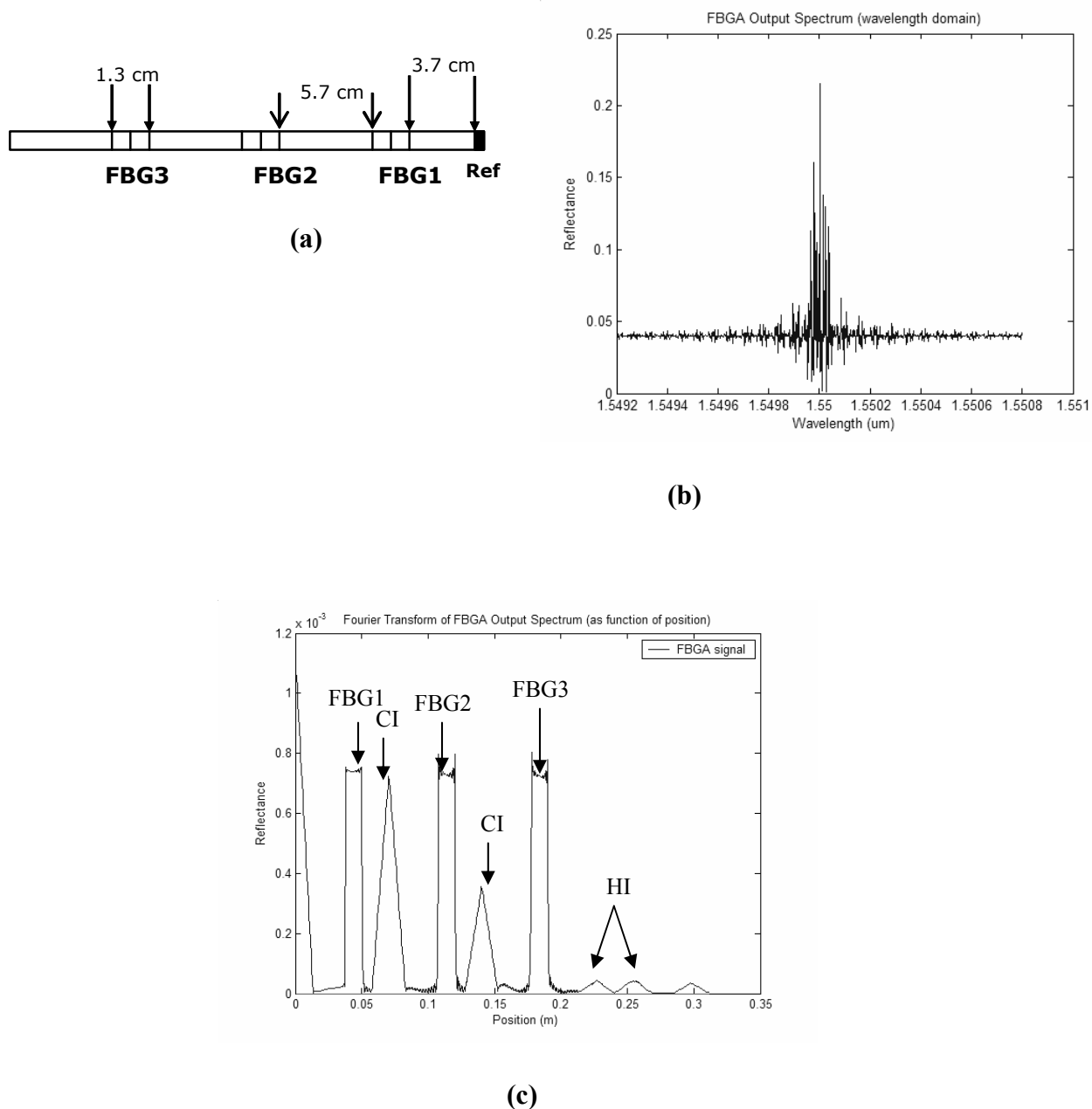


Figure 10.5 (a) Design of the three-elements, 15.3 cm FBGA and the resulting interference signal in the (b) wavelength domain (c) and the Fourier domain

in Figure 10.5(c) are the FBG-reflector interferences, and second and fourth peaks are the cavity interferences (CI); the rest of the interference peaks are higher order interferences. As shown in Figure 10.5(c), the FBG-reflector and the cavity interferences are separated in the Fourier domain; this satisfies the main criteria. The operating bandwidth is 1.6nm and the tunable laser wavelength increment is 1pm.

### **10.3.3. FBGA system fabrication**

The final design of the FBGA was copied onto a piece of paper, and the position of each FBG was marked along the photosensitive fiber. The optical fiber used was a Boron/Germanium co-doped photosensitive fiber, F-SBG-15 from Newport Corp operating at 1550 nm. A striper was then used to remove 2.5 cm of the coating around the position of each FBG in the array. The FBGs were inscribed into the core of the photosensitive fiber using the setup described in Chapter 4. By controlling the tension of the optical fiber and monitoring the back reflectivity using an EDFA source and an optical spectrum analyzer (OSA), each FBG in the array was given the similar peak wavelength and reflectance of  $\sim 1551.2$  nm and  $\sim 1\%$ , respectively. The bandwidth of each FBG was about 120 pm.

### **10.3.4. FBGA and C-OFDR testing**

The 3-element, 15 cm FBGA was bonded to the 75 cm x 3 cm x 0.2 cm aluminum cantilever beam using epoxy. Three ESG gauges (CEA-06-250UN-120) were located next to the position of each FBG in the array. A 30 cm measuring ruler located at the tip end was used to determine the vertical displacement of the beam. A tunable laser diode

(Tunics-BT) was used to source the FBGA, and a bridge/amplifier arrangement was used to interrogate the ESG. Figure 10.6 shows the layout. The resulting signal from the amplifier was then measured using a DVM. Both the tunable laser and fiber optic photo-detector were controlled through the computer (PC) using GPIB interface.

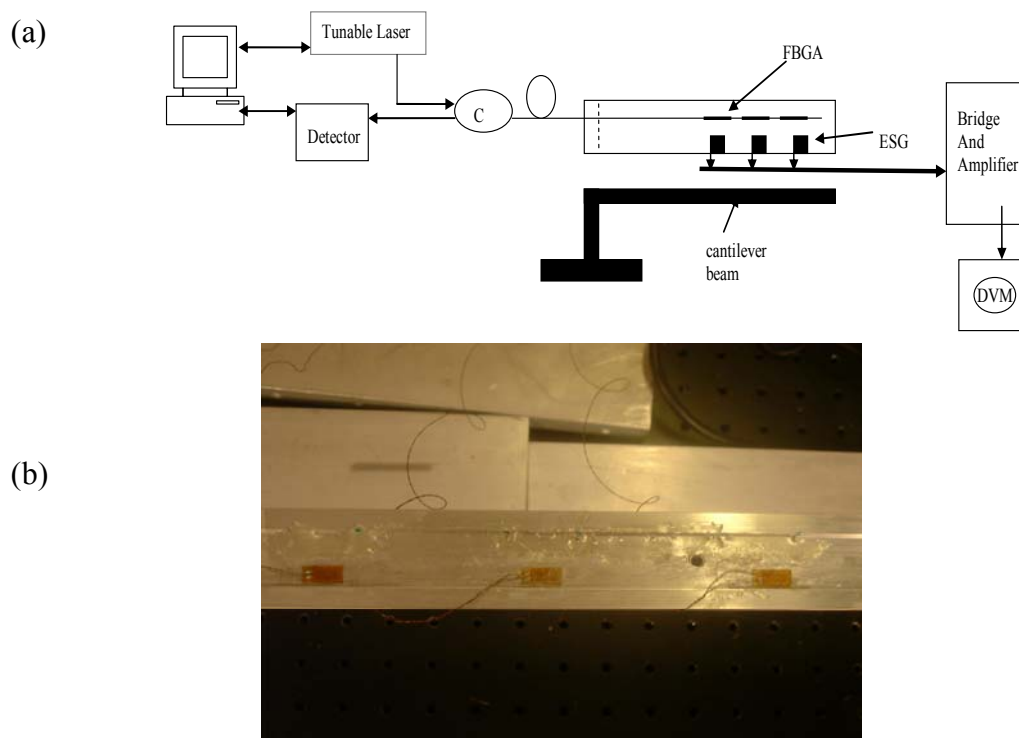


Figure 10.6 (a) FBGA and ESG attachment to a cantilever beam host. The tip of the cantilever beam is varied and the corresponding strain information from the FBGA and ESGs are compared. (b) Close up look of the FBGA and ESGs on the cantilever beam.

### 10.3.5. C-OFDR and FBGA results

The setup in Figure 10.6 was used to test the FBGA. The tip of the cantilever beam was displaced by 5 cm, 10 cm, and 15 cm. At each displacement, the signal from the bridge/amplifier was measured for each ESG. Following the ESG measurements, the signal from the FBGA system was recorded. The simulation software was used then used to process the raw FBGA system signal. The signal was Fourier transformed and the three FBG-reflector interference peaks extracted. To recover the spectrum for each FBG in the array, the extracted peaks are then inverse Fourier transformed. From this, the changes in the Bragg wavelength was recorded for each FBG as a the tip of the cantilever beam was displaced by 5 cm, 10 cm, and 15 cm. Figure 10.7(a)(b) shows the FBGA interference signal in wavelength and Fourier domain. Figure 10.7(c) shows the demodulated spectrum for each FBG at 0 cm and 15 cm cantilever tip displacement. Figure 10.8 shows the ESG results and the measured strain at each position of the FBG at various displacement points of the cantilever beam. The trend shown in Figure 10.8 is what is expected for a rectangular cantilever beam. For a rectangular cantilever beam, the clamped end has the largest axial strain and the tip of the cantilever beam has the lowest axial strain; between the two extremes is a linear relationship between the position and strain. In addition, the magnitude of the axial strain is directly related to the tip displacement; this will tend to shift the entire strain field upward as the tip displacement increases as shown in Figure 10.8. From Figure 8.8(b), the peak strain is around 140  $\mu\epsilon$  and the peak percent strain error with respect to ESG results is 18.5%. The ESG and FBGA results were comparable as shown in Figure 10.8(a). The differences can be

attributed to the quality of the bonding of the FBGA and ESG to the cantilever beam. There are also errors when the peaks are extracted and inverse Fourier transformed to get the FBG spectrum.

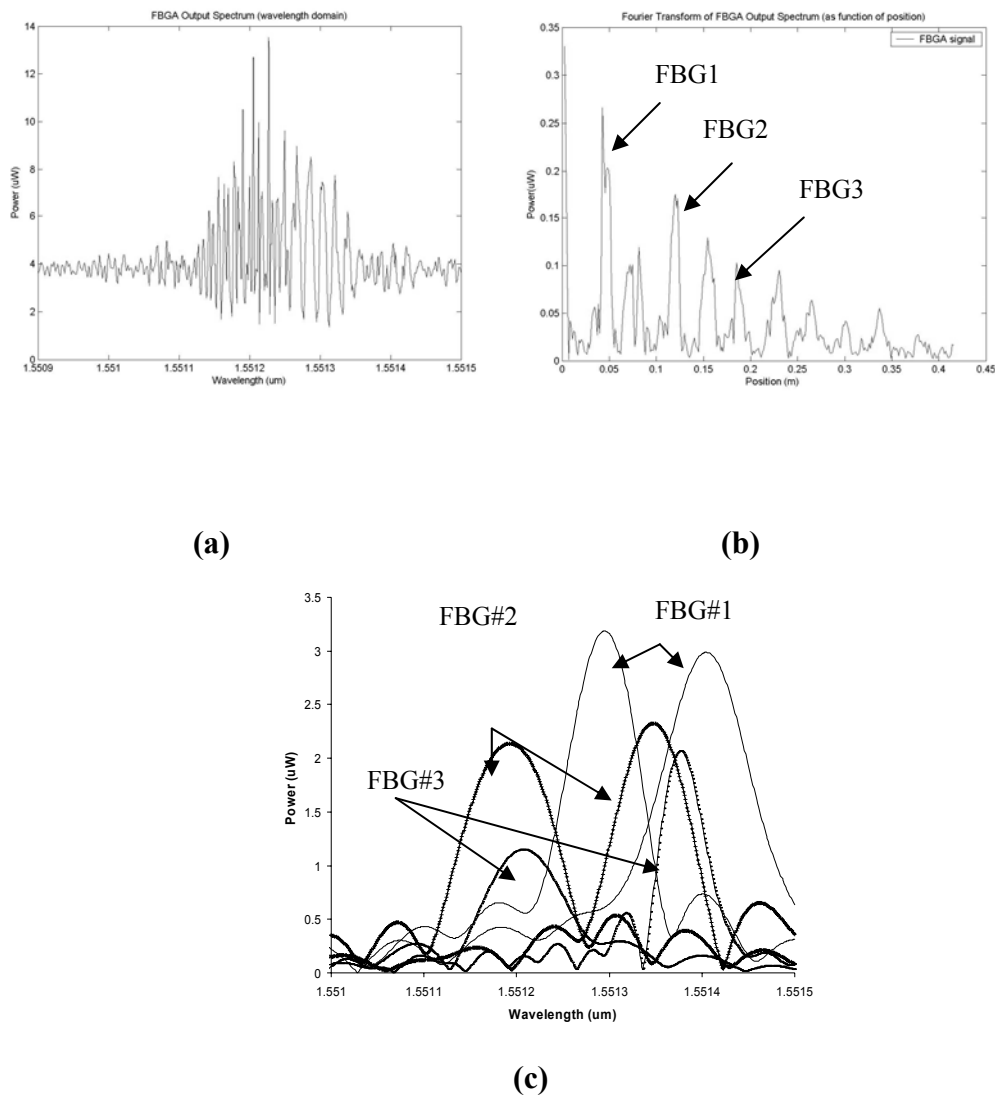
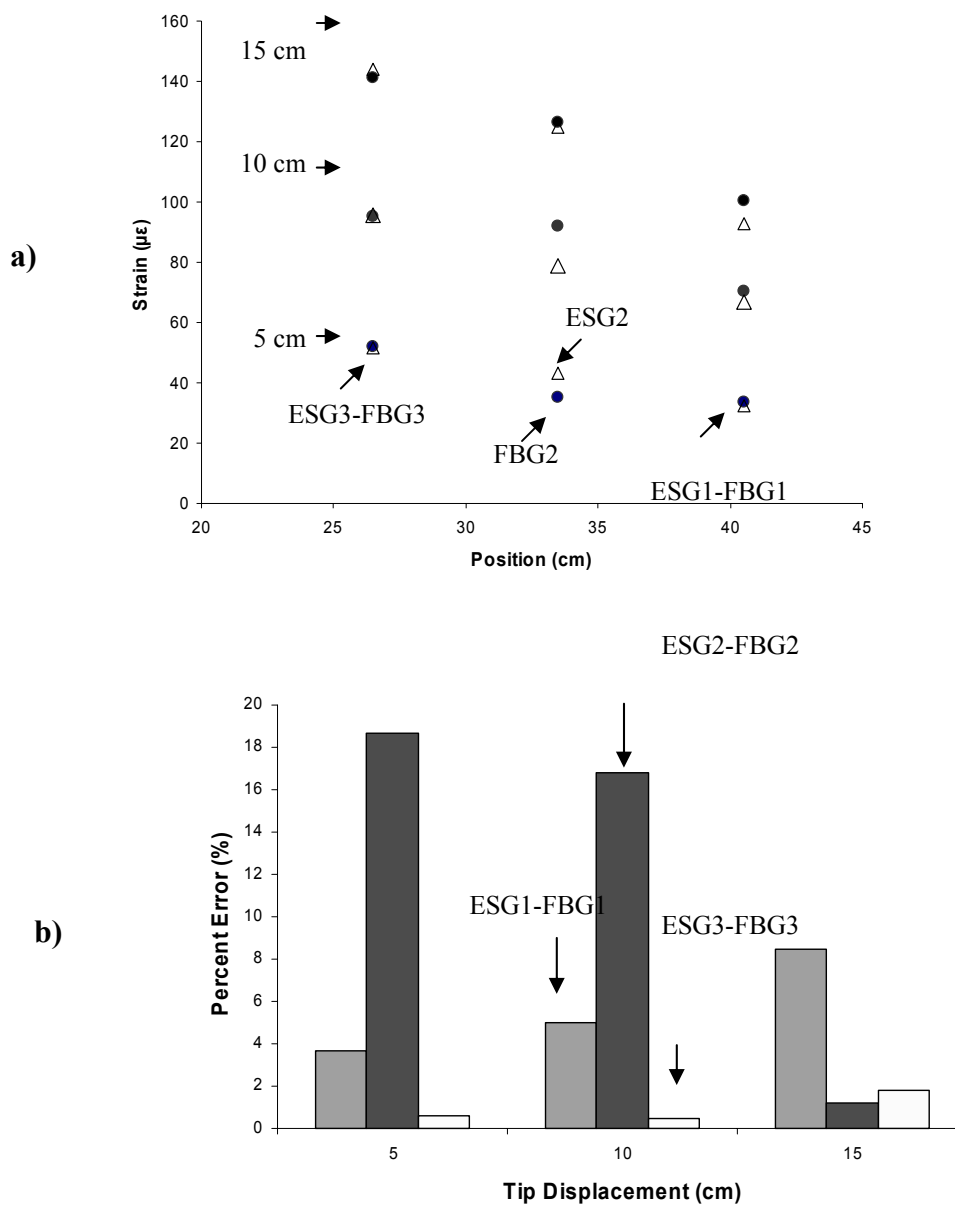


Figure 10.7 The figure shows the FBGA reflectance spectrum in the (a) wavelength and b) Fourier domain.



**Figure 10.8** (a) ESG and FBGA results as function of cantilever beam tip displacement and axial position. b) Percent strain error of each FBG in the array with respect to ESGs results as function of tip displacement.

Depending on the width of the rectangular window, the recovered spectrum shape can vary resulting in slight variations in the center wavelength. Also, the repeatability of the

laser introduces error in FBGA strain measurements. The latter is the most significant; if the worst case is taken, a repeatability  $\pm 10$  pm will translate to  $\pm 8$   $\mu\epsilon$  error.

### 10.3.6. Discussion

The simulated and experiment FBGA Fourier spectrum gave similar positioning of the interference peaks, including the higher order interferences. However, in the experimental data, the magnitude of the interference peaks decreases as a function of position. In addition to decrease in the magnitude of the inference peaks, the demodulated FBGA signal shows distortion of the recovered FBG spectrums; FBG3 shows the largest effect. This suggests error in the wavelength increments either due to tuning mechanics or the variations in the injection current of the laser. To confirm this hypothesis, the simulation done in section 10.3.2 was repeated but this time adding a 2.5 pm uniform random wavelength noise on top of the 1 pm wavelength increment. This is analogous to super-imposing white noise into the injection current of a laser diode. Since the wavelength is directly related to the injection current, adding white noise will broaden the line-width of the laser and decrease the coherence. If the magnitude of the white noise is large enough, this will tend to washout interferometric signals. For our case, we can consider the tuning mechanism of the laser or the injection current as noise centers. Adding 2.5 pm noise to the wavelength increment means that the minimum wavelength increment is 1 pm and the maximum wavelength increment is 3.5 pm. Figure 10.9 shows

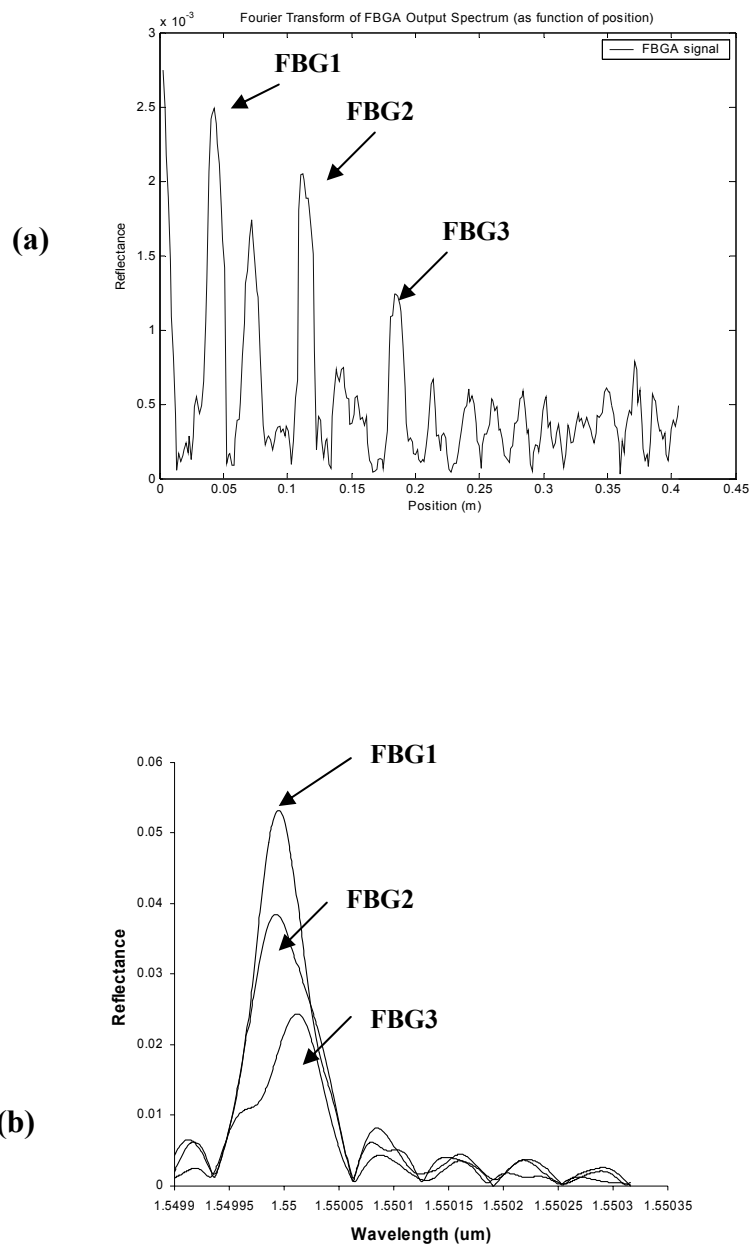


Figure 10.9 The figure shows the simulated FBGA reflectance in (a) the Fourier domain with a 2.5 pm uniform noise added to wavelength increment. (b) FBGA demodulated spectrum.

the results. In the figure, the magnitude of the interference peaks decreases as a function of position, similar to the experimental data. Also, the recovered FBG spectrums show a drop in their peak magnitude and distortion of its shape, particularly for FBG3, similar to the experiment. It took several tries using to get the results shown Figure 10.9, suggesting that the laser tuning mechanism is not a pure white noise distribution; in fact, the trend in the experimental data is consistent over several runs with some minor variations; suggesting that something inherent in the tuning mechanism of the laser. It is beyond the scope of this work to investigate the true tuning properties of the laser used, however, from the simulation results, we can conclude that the tunable laser has non-uniform wavelength stepping increments at the 1 pm setting. The effects of the variation of the wavelength increment on the FBGA system have been observed by others and reducing its effect is a current research topic (Passy, et al. 1994). Typically, the variation in the wavelength can be minimized by coupling a reference interferometer to the tunable laser (Froggatt et al. 1998). The resulting interference of the reference interferometer has precise spacing as was shown in the analysis of the FPI interferometer. The length of the interferometer must be greater than twice the length of the FBGA system to satisfy Nyquist criteria. The previous techniques used to investigate the stepping accuracy of the tunable laser suggest a way to determine the tuning quality of a tunable laser. For example, if a FBGA designed to work at 1pm resolution is used then there should be no drop in the magnitude of the interference peaks as function of position at the 1pm wavelength increment.

Using an incremental tunable laser has several disadvantages. The time to make entire scan was long, typically requiring 5 minutes at an increments of 1 pm, therefore, dynamic measurements was out of the question using our setup. Also, due to the finite stepping wavelength increment of the tunable laser, the maximum length of the FBGA was limited as was shown in this work. The FBGs in the array are also spaced too closely to be of a practical use. Its make more sense for each FBG to measure different parameters, for example, one FBG can measure strain, while the other two can measure temperature and pressure, respectively. To achieve a longer FBGA and/or faster measurements, continuous scan tunable laser is required, for example, a fast tunable fiber laser system. If the measurement speed is increased then each FBG in array can be calibrated using the FPI strain gauge calibrator. Each FBG in the array would then experience the same strain field; this will make it possible to simultaneously calibrate all the FBGs. Sidney, et al. (2002) demonstrated the calibration of a FBG using C-OFDR interrogate. Instead of using the EDFA, C-OFDR can be used to interrogate the FBGA. This will eliminate the cantilever beam for testing purpose and the FBGA can be used after calibration and testing, similar to what was shown in section 5 for a single FBG.

#### **10.4. Conclusion**

We have shown that the transfer matrix approach can be used to model a FBGA/C-OFDR system. In this approach, an elemental transfer matrix is used to represent the optical and geometrical characteristics of a single element in the FBGA system. The response of the entire FBGA system can then be determined simply by multiplying all the elemental transfer matrices in the proper order. The advantage of this

approach is that any optical device can efficiently be incorporated if its transfer matrix is known. We have successfully used this approach to design and simulate a 15.3 cm, 3-element fiber Bragg grating array with Optical Frequency Domain Reflectometry interrogation technique. Comparison between the simulation and experimental findings showed that the simulation and experimental results gave similar positional information of the FBGs, however, in the experimental data, the magnitude of the interference peaks decreased as function of FBG position. In addition, the recovered FBG spectrums showed a drop in peak magnitudes and distortion of the FBG spectrums. We were able to reproduce this effect in the simulation by injection white noise into the wavelength scan. From the simulation results, we conclude that the tunable laser had non-uniform variations in the wavelength increments, resulting in the near wash out of the interference peaks. However, the recovered FBG spectrums were usable and we were able to perform strain tests on a cantilever beam. The results showed that the peak strain error was 18% compared to the electric strain gauges. Overall, the transfer matrix technique gave an accurate representation of the experimental results and allowed direct a comparison between the experimental and simulation results. Improvements in measurement speed can be made by employing a continuous scanning tunable laser and reference interferometer to precisely determine source wavelength.

## 11. CAVITY SUPPRESSION IN FBGA/C-OFDR SYSTEM

As shown in the previous section, it is possible for the cavity interferences to super impose onto FBG-reflector interferences when their corresponding beat frequencies are equal, resulting in the distortion of the recovered FBG spectrums. Several techniques have been implemented to eliminate this distorting. In the previous section, the cavity interferences and reflector-grating interferences were purposely separated in the FBGA system. Two other techniques can be used to reduce the effects of cavity interferences. The first technique is to reduce the grating reflectance and increasing the reference reflector reflectance, effectively using the reflector a gain. The second technique is to down shift the cavity interferences to a lower frequency band (Frogget, 1998). In this work, a third technique that subtracts out the cavity interferences directly from the overall signal is simulated. To the best of the author's knowledge, cavity suppression in C-OFDR/FBGA system is an original contribution by the author to the technology in the public literature. This technique eliminates the need for the reference length to be greater than the length of the FBGA. Thus, the required bandwidth is one half that of the downshifting method. In the following sections, the three methods will be shown and compared.

### 11.1. Reducing FBG reflectance

The ratio between the peak power contained in the cavity interferences and the FBG-reflector interferences can be approximated as:

$$\frac{I_c(\lambda)}{I_{R-FBG}(\lambda)} \sim \frac{\sum_i^N \sum_{j>i}^N \sqrt{FBG_i(\lambda) \cdot FBG_j(\lambda)}}{\sum_i^N \sqrt{R_{ref} \cdot FBG_i(\lambda)}} = \frac{C(N,2) \sqrt{FBG(\lambda)}}{N \sqrt{R_{ref}}} = \frac{1}{2} (N-1) \sqrt{\frac{FBG(\lambda)}{R_{ref}}}, \quad (11.1)$$

As shown in Eq. 11.1, the ratio between the contributions between the cavity interferences and reflector-grating interferences is proportional to the number of gratings and the square root of the grating reflectance. The required grating reflectance to reduce the cavity interference contributions to a percentage of the grating-reflector interference contribution is given by:

$$\%cc = 50 \cdot N \sqrt{\frac{FBG(\lambda_B)}{R_{ref}}} \quad (11.2)$$

where %cc is the percent cavity interference contribution and assumes that we are solving at the Bragg wavelength and the number of gratings in the array is larger than one. From Eq 11.2, the reference reflector acts like a gain and increasing the reference reflector reflectance and decreasing the FBG reflectance should reduce the contribution of the cavity interferences. For example, if there are 10 gratings and with a 4% reference reflector, the peak grating reflectance should be  $\sim 2 \times 10^{-7}$  to reduce the cavity interferences to 1%. However, for example, if there are 100 gratings and with a 4% reference reflector, the peak grating reflectance should be  $\sim 2 \times 10^{-9}$  to reduce the cavity interferences to 1%. Since the grating reflectivity is very small, this means that the processing of the signal will be very dependent on the receiver sensitivity and signal to noise ratio (SNR).

## 11.2. Down shifting method

In the down shifting method, the reference length  $L_1$  (cf. Figure 11.1) is made larger than the length of the FBGA ( $L_N - L_1$ ) such that the beat frequencies:

$$f_i = \frac{2nL_{ref}}{\lambda^2} \gg \frac{2nL_g}{\lambda^2} \quad (11.3)$$

If Eq. 11.3 is the case, then the cavity interference can be ignored all together. There are several undesirable properties using the down shifting method to eliminate the cavity interference.

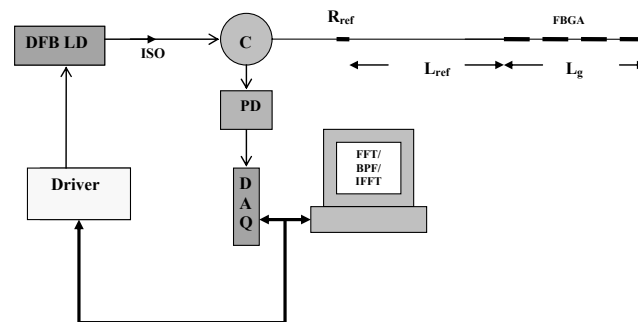


Figure 11.1 Model of FBGA/C-OFDR using cavity downshifting method

First, a length of fiber equal to the twice the length of the FBGA is needed. For short FBGAs this not a problem, however, for monitoring a length of a road, power-line, or a long span bridge this may not be feasible. Second, while the cavity interferences are down shifted to a lower frequency band, the reflector-FBG interferences are up shifted to a higher frequency band, in fact, by at least a factor of 2 without down shifting since the

length of the FBGA system doubles. This means that modulation frequencies will at least double, unnecessarily using up bandwidth. Third, it would be difficult to add extra FBGs to a pre-existing FBGA since the FBGA is constrained by the reference length, effectively making each FBGA system unique. To avoid such problems the reference length would need to be much larger than would be required.

### 11.3. Cavity interference suppression method

In the previous chapter, excluding the DC components, the output of the detector observed from the FBGA system can be determined by summing the cavity interference contributions and reflector-FBG contributions. The contribution of the reflector-FBG interference can then be determined by subtracting the cavity interference contribution from the overall contribution:

$$I_{ref-FBG} \approx I - I_c, \quad (11.4)$$

where  $I$  is the power contribution of the cavity and reflector-grating contributions. In this section, the transfer matrix approach will be used to demonstrate the simulation of a passive suppression of the cavity interference using two simultaneous measurements of the FBGA system. Two transfer matrices will be used to represent the two measurements. One transfer matrix will represent the FBGA system that contains the reference reflector while a second transfer matrix will represent just the FBGA without the reference reflector. The resulting reflectance of the two transfer matrices will then be subtracted to suppress the cavity interferences. A practical design will then be proposed using polarizers, a quarter-wave plate, and two polarization rotators.

As described in this section, the transfer matrix  $T$  from the previous chapter is split into two components, one containing the total interference signal ( $T^1$ ) with the reference reflector, and other transfer matrix containing only the cavity interference ( $T^2$ ) without the reference reflector:

$$\begin{aligned} T^1 &= [R_{ref}][P][FBG^1][P][FBG^2][P][FBG^3] \dots [FBG^{N-1}][P][FBG^N] \\ T^2 &= [FBG^1][P][FBG^2][P][FBG^3] \dots [FBG^{N-1}][P][FBG^N] \end{aligned} \quad (11.5)$$

The resulting transfer matrices and reflectances are then given by:

$$\begin{aligned} R_1(\lambda) &= \left( \frac{|T^1_{21}(\lambda)|^2}{|T^1_{11}(\lambda)|^2} \right) \\ R_2(\lambda) &= \left( \frac{|T^2_{21}(\lambda)|^2}{|T^2_{11}(\lambda)|^2} \right) \end{aligned} \quad (11.6)$$

To recover individual FBG spectrum using C-OFDR, the Fourier transform of the FBGA reflectance spectrum is taken. A simple band-pass filter, represented by a rectangular window (REC) centered at a desired beat frequency ( $f_i$ ), is then used to extract desired FBG signal from the Fourier spectrum. Once extracted, this information is then inverse Fourier transformed to recover the wavelength information of the desired FBG or in a mathematical form given by:

$$FBG_i(\lambda) = \left| F^{-1} \left\{ F(R_1(\lambda) - R_2(\lambda)) REC \left( \frac{f - f_i}{\Delta \lambda_{FBG}} \right) \right\} \right|, \quad REC(x) = \begin{cases} 1 & |x| < \frac{1}{2} \\ 0 & otherwise \end{cases}, \quad (11.7)$$

where  $F()$  and  $F^{-1}()$  are the Fourier and inverse Fourier transform, respectively.

### 11.3.1. Cavity interference suppression simulation and results

To test the above system, a 2 meter steel (Modulus of 200GPa), 4 cm thick cantilever beam and 2 meter, 9-element FBGA were simulated and the results compared with the FEM results. Figure 11.2 shows the cantilever beam and FBGA system. In the design, the reflector position is set in front of the FBGA. Table I shows the specifications for the cantilever and FBGA system. The reflectance of the gratings is 0.3% and centered at 1550 nm. The width of the gratings is 1 cm and spaced 23.9 cm apart. For the tunable laser, the scanning increment is 0.1 pm and with a bandwidth of 1.6 nm, enough to measure  $\pm 680 \mu\epsilon$  at 0.8 m/m/ $\mu\epsilon$  SGF, with a center wavelength at 1550 nm. To demonstrate cavity suppression, the cavity interferences were overlapped with reflector-FBG interferences. This was accomplished by setting the reference length to 37 mm. Using cavity down shifting method, the reference length would need to be at least 2 meters to avoid cavity interferences, therefore, the total length of the system would be 4 meters minimum.

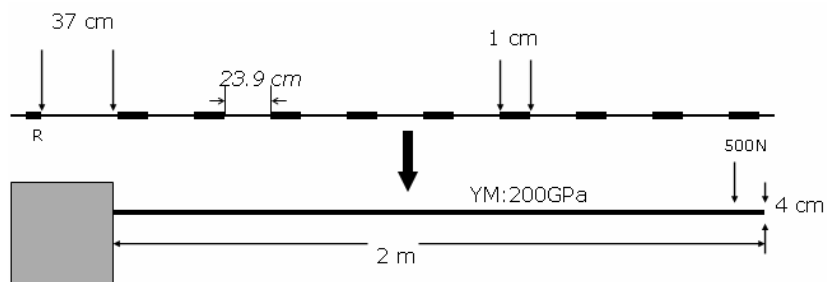


Figure 11.2 Cantilever beam model with end force F and attached FBGA

**Table 11.1. Cantilever beam, FBGA, and wavelength scanning specification for OFDR demodulation simulation**

Cantilever Beam:	FBGA specification:	Scanning specification:
Length: 2 m	Length of array: 2 meters	Operating wavelength: 1550 nm
Thickness: 4 cm	Number of FBGs: 9	Wavelength resolution: 0.1 pm
Young Modulus: 200 GPa	Spacing of FBGs: 23.9 cm	Bandwidth: 1.6 nm (~ ±680 ue)
Moment of Inertia: $2.13 \times 10^5 \text{ mm}^4$	FBG length: 10 mm	
End Force: 500 N (112 lb)	Peak reflectance per FBG: 0.3%	
	FBG bandwidth: 0.16 nm	
	Core index (n): 1.45	
	Reference arm: 37 mm	
	Reflector: 4% reflectance	

Figure 11.3 shows the resulting interference for the case of load and no load applied to the tip of the cantilever beam, respectively.

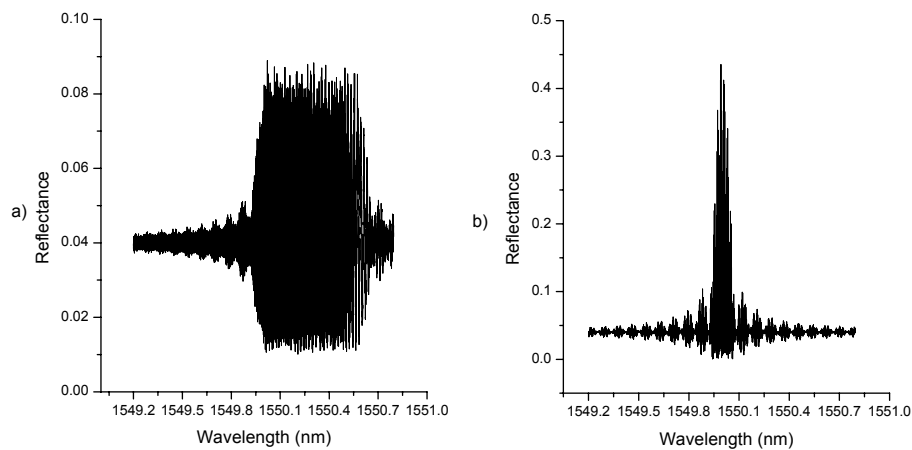


Figure 11.3 Interferences between FBGA and reflector with (b) no load and (a) 500 N force on the cantilever beam tip.

For the case of no load, the peak reflectance is at 0.4% and the interferogram is essentially a composite of all nine FBGs spectrums with a nominal center wavelength of 1550 nm. For the case of tip load, the interference spectrum spreads and the reflectance drops to 0.09%. The spread is due to variation in strain across the cantilever beam resulting in a proportional displacement of the center wavelengths of each FBG. Figure 11.4 shows the Fourier spectrum of both interference as a function of position, with and without cavity suppression. There are nine reflector-FBG interference peaks at each FBG position, along with the cavity interference peaks. There is a noticeable drop in the magnitude of the cavity interference peaks for the case of tip load as shown in Figure 11.4(c). Since the center wavelengths of each FBG is off from the nominal center wavelength of 1550 nm, there is less overlap between the spectrums of each FBG, resulting in the reduction of the cavity interferences. With cavity suppression, there is a significant drop in the magnitude of the cavity interferences for both load and no load cases. However, cavity interferences are still noticeable for the case of no load with cavity suppression. This is due to several factors including the fact that multiple pass interferences (more than 2 passes) between the fields from the reflector and each FBG cannot be suppressed by subtracting out the cavity interferences since the cavity interferences contain no such information about the reference reflector. In addition, interference between the beats can occur, resulting in higher order interferences. Higher order interferences can then also interfere with the field from the reference reflector. This component can not be suppressed using the cavity subtraction technique because of

reasons outlined above. The best way to eliminate higher interferences is to reduce the grating reflectance to a level that minimizes this component.

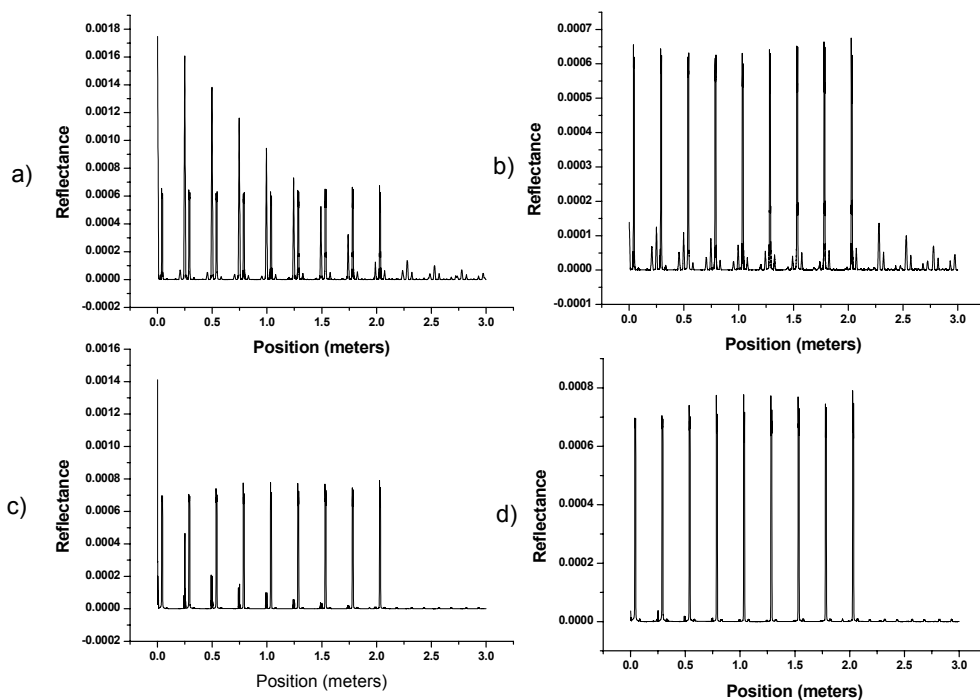


Figure 11.4 Interference between FBGA and reflector in the Fourier Domain with (a) no load, (b) no load with cavity suppression, (c) 500 N end force, (d) 500 N end force with cavity suppression.

The resulting C-OFDR processing is shown in Figure 11.5. An algorithm that used threshold and a narrow band pass filter in the Fourier domain was used to automatically extract individual interference peaks. An inverse Fourier transformed was then used to recover the FBG spectrum. A peak finder algorithm is then used to determine the center wavelength. The FBG spectrum and the C-OFDR demodulated signal for FBG#5, with

tip force applied, are shown in Figure 11.5(a)(b). Again, there is a shift in the center wavelength due to strain at the position of the FBG. Side lobes are noticeable in Figure 11.5(b) due to the rectangular window of the bandpass filter. Figure 11.5Fig. 4(c)(d) shows the strain on each FBG sensor as function of axial position along with FEM results, and the percent error with respect to the FEM, respectively. The results show good agreement between the FEM input and the OFDR results within 0.12% average strain error and 0.26% maximum strain error.

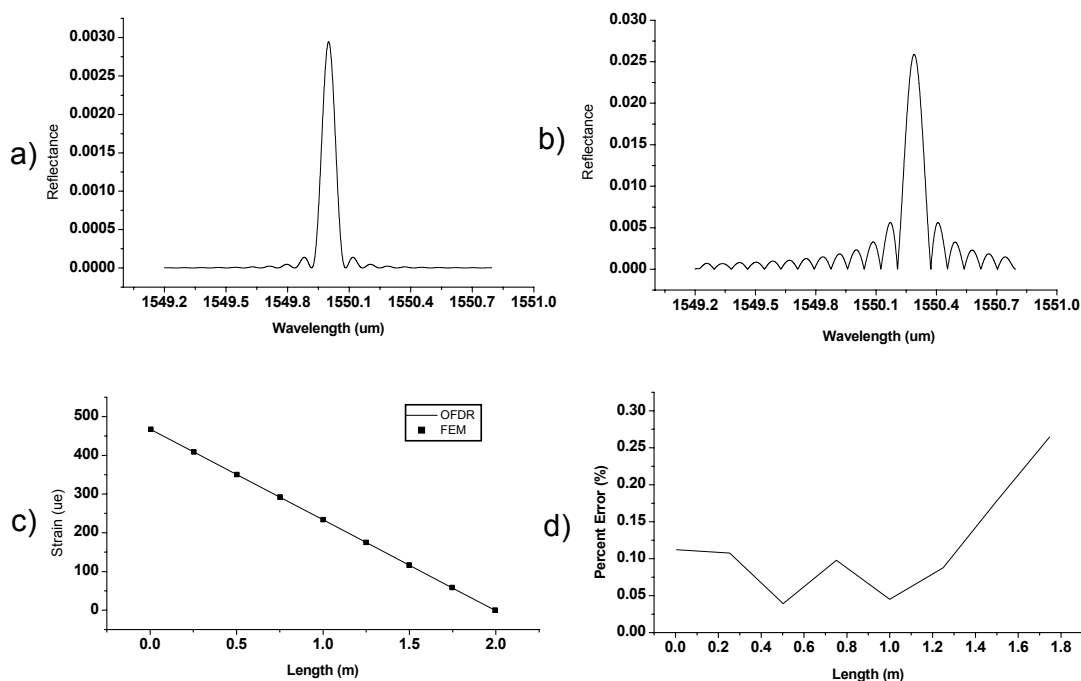


Figure 11.5 (a) individual FBG prototype spectrum. (b) OFDR demodulation for strained FBG sensor # 5. (c) OFDR and FEM strain results. (d) Percent strain error between FEM and OFDR results.

Notice that FBG #9 was not included in the percent error plot in Figure 11.5(d) because the error is essentially infinity since the strain at the tip of the cantilever beam is theoretically zero. Since external noise was not added during the simulation, the error in the C-OFDR results can be attributed to numerical noise such as due to the FFT/IFFT algorithm, positioning of the band-pass filter, and finding the peak finding algorithm.

### **11.3.2. Design implementation**

Two design implementations using a Michelson and FPI type interferometer are proposed as shown in Figure 11.6. In the case of the Michelson, the circular polarized source is split by a coupler and launched into the two arms of the interferometer. On the reference arm side, the circular polarized light is split by a polarization sensitive beam splitter into an s-polarization and p-polarization linear polarizations. The s-polarization reflects off the reference mirror and returns to coupler while the other is passed through the beam splitter. The s-polarization then mixes with the circularly polarized field from the FBGA. At the detectors end, two perpendicular polarizers will then filter the resulting interference pattern. One polarizer is perpendicular to s-polarized light, thus suppressing that polarization, and will only see the circular polarized light from the FBGA system. The second polarizer will see the interference between s-polarization and the circularly polarized light from the FBGA. The two resulting signals are then subtracted to suppress the cavity interferences. Figure 11.6(b) shows the same implementation using a FPI arrangement; in this case, a polarization sensitive beam splitter is set at the tip of the fiber. The advantage of the Michelson design is that the polarization beam splitter and the

reference reflector can be set close to interrogation system and not at the tip of the FBGA as in the case for the FPI design, offering a more compact design. To compute the polarization and the resulting signals from the detectors requires a two step process is required. In the first process, the power transmitted and reflected by the devices at each polarization is determined. This is then repeated for the two orthogonal polarization states. If the source is initially linearly polarized in the x-axis, a quarter-wave plate and two rotators can be used to convert polarization to circular. This method is desirable since the input polarization can be easier controlled.

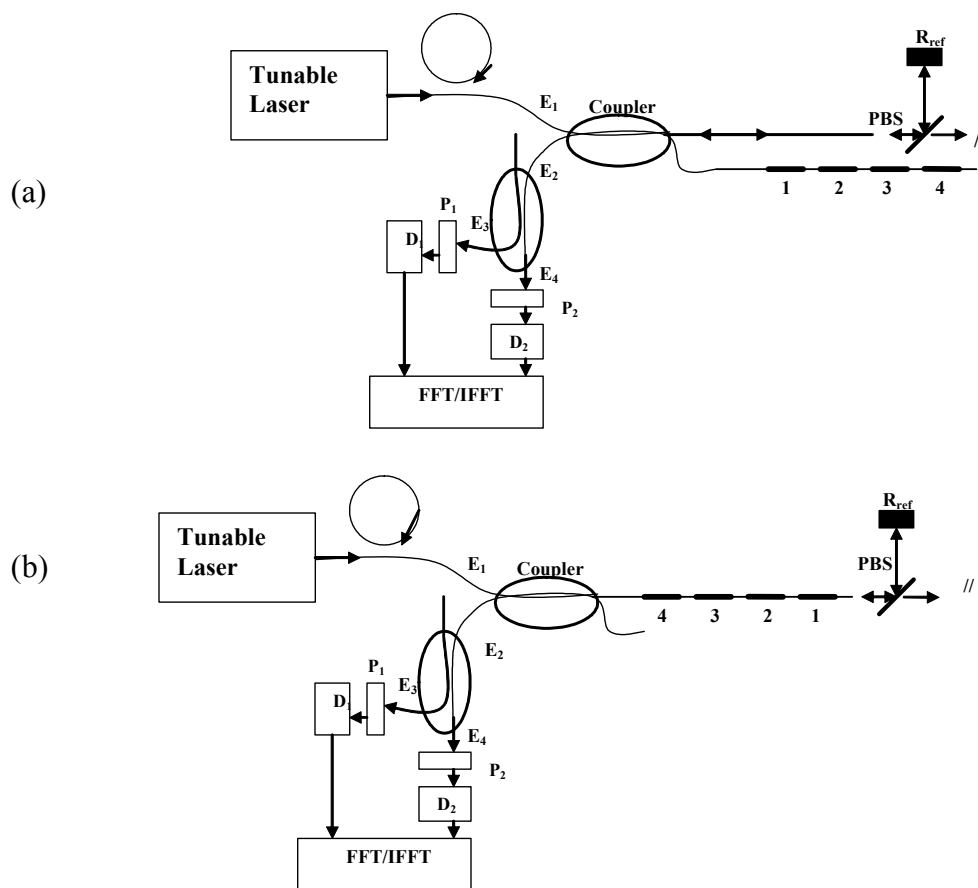


Figure 11.6 Cavity suppression systems using (a) Michelson and (b) FPI configurations.

For both orthogonal polarizations, the fields just before the polarizers are given by:

$$\begin{bmatrix} E_3 \\ E_4 \end{bmatrix}_{x,y} = M_C M_2 M_C M_{FBGA} M_C \begin{bmatrix} E_1 \\ 0 \end{bmatrix}_{x,y} \quad (11.8)$$

Where  $M_2$  eliminates the open port at the first coupler and  $M_{FBGA}$  and  $M_C$  are the transfer matrices for FBGA system and the couplers, respectively. In reality, there are two transfer matrices for  $M_{FBGA}$ , one for each orthogonal polarization. The transfer matrices are then given by:

$$M_C = \frac{1}{\sqrt{2}} \begin{bmatrix} 1 & j \\ j & 1 \end{bmatrix} \quad M_2 = \begin{bmatrix} 0 & 0 \\ 0 & 1 \end{bmatrix} \quad M_{FBGA} = \begin{bmatrix} \sqrt{R_{1,2}} & 0 \\ 0 & 0 \end{bmatrix} \quad (11.9)$$

Eq. 11.9 then expands to:

$$\begin{aligned} \begin{bmatrix} E_3 \\ E_4 \end{bmatrix}_{x,y} &= \frac{1}{\sqrt{2}} \begin{bmatrix} 1 & j \\ j & 1 \end{bmatrix} \begin{bmatrix} 0 & 0 \\ 0 & 1 \end{bmatrix} \frac{1}{\sqrt{2}} \begin{bmatrix} 1 & j \\ j & 1 \end{bmatrix} \begin{bmatrix} \sqrt{R_{1,2}} & 0 \\ 0 & 0 \end{bmatrix} \frac{1}{\sqrt{2}} \begin{bmatrix} 1 & j \\ j & 1 \end{bmatrix} \begin{bmatrix} E_1 \\ 0 \end{bmatrix}_{x,y} \\ &= \frac{E_1 \sqrt{R_{1,2}}}{2\sqrt{2}} \begin{bmatrix} -1 \\ j \end{bmatrix}_{x,y} \end{aligned} \quad (11.10)$$

$M_C$  assumes 50/50 coupler. At the detectors:

$$\begin{bmatrix} D_{i,x} \\ D_{i,y} \end{bmatrix} = M_{Pi} \begin{bmatrix} E_{i,x} \\ E_{i,y} \end{bmatrix}, \quad (11.11)$$

where the polarizers at the detector are given by:

$$M_{P1} = \begin{bmatrix} 1 & 0 \\ 0 & 0 \end{bmatrix} \quad M_{P2} = \begin{bmatrix} 0 & 0 \\ 0 & 1 \end{bmatrix} \quad (11.12)$$

If the input is circularly polarized such that  $E_1 = E_0 \begin{bmatrix} 1 \\ j \end{bmatrix}$ , then for D1:

$$\begin{aligned} \begin{bmatrix} D_{1,x} \\ D_{1,y} \end{bmatrix} &= \frac{E_0}{2\sqrt{2}} \begin{bmatrix} 1 & 0 \\ 0 & 0 \end{bmatrix} \begin{bmatrix} -\sqrt{R_1} \\ j\sqrt{R_2} \end{bmatrix} \\ &= \frac{-E_0\sqrt{R_1}}{2\sqrt{2}} \begin{bmatrix} 1 \\ 0 \end{bmatrix} \end{aligned} \quad (11.13)$$

and D2:

$$\begin{aligned} \begin{bmatrix} D_{2,x} \\ D_{2,y} \end{bmatrix} &= \frac{E_0}{2\sqrt{2}} \begin{bmatrix} 0 & 0 \\ 0 & 1 \end{bmatrix} \begin{bmatrix} j\sqrt{R_1} \\ -\sqrt{R_2} \end{bmatrix} \\ &= \frac{-E_0\sqrt{R_2}}{2\sqrt{2}} \begin{bmatrix} 0 \\ 1 \end{bmatrix} \end{aligned} \quad (11.14)$$

Finally, subtracting the output of the detectors:

$$R(\lambda) = D_{1,x}^2 - D_{2,y}^2 = \frac{E_0^2}{8} (R_1(\lambda) - R_2(\lambda)) \quad (11.15)$$

The result of Eq. 11.15 satisfies the cavity subtraction method and using the Fourier transform and band-pass filter matches Eq. 11.7. If the polarizers are ganged together and are able to be mechanically rotated, then the orthogonality can be maintained, therefore, the field contribution from the reflector can simultaneously be passed and rejected. Also, since the source is circularly polarized, the polarizers will have no effect

other than 50% reduction in the power. For the case of the Michelson, the transfer matrix of the FBGA system is given by:

$$M_{FBGA} = \begin{bmatrix} \sqrt{R_2(\lambda)} & 0 \\ 0 & Y(\varphi) \end{bmatrix} \quad (11.16)$$

Where  $Y(\varphi)$  is the phase delay due to the reference arm. If the beam splitter is set so that

x-polarization reflects off the reference reflector,  $Y(\varphi)$  is given by  $\sqrt{R_{ref}} \cdot e^{-j \frac{2\pi(2nL_{ref})}{\lambda}}$ ,

where  $r$  is the reflectivity of the reflector. For the y-polarization,  $Y(\varphi)$  is zero.

Expanding 11.8 for the Michelson:

$$\begin{aligned} \begin{bmatrix} E_3 \\ E_4 \end{bmatrix}_{x,y} &= \frac{1}{\sqrt{2}} \begin{bmatrix} 1 & j \\ j & 1 \end{bmatrix} \begin{bmatrix} 0 & 0 \\ 0 & 1 \end{bmatrix} \frac{1}{\sqrt{2}} \begin{bmatrix} 1 & j \\ j & 1 \end{bmatrix} \begin{bmatrix} \sqrt{R_2} & 0 \\ 0 & Y(\varphi) \end{bmatrix} \frac{1}{\sqrt{2}} \begin{bmatrix} 1 & j \\ j & 1 \end{bmatrix} \begin{bmatrix} E_1 \\ 0 \end{bmatrix}_{x,y} \\ &= \frac{E_1(\sqrt{R_2} + Y(\varphi))}{2\sqrt{2}} \begin{bmatrix} -1 \\ j \end{bmatrix}_{x,y} \end{aligned} \quad (11.17)$$

For field at detector D1:

$$\begin{aligned} \begin{bmatrix} D_{1,x} \\ D_{1,y} \end{bmatrix} &= \frac{-E_0}{2\sqrt{2}} \begin{bmatrix} 1 & 0 \\ 0 & 0 \end{bmatrix} \begin{bmatrix} \sqrt{R_2} + Y(\varphi) \\ j\sqrt{R_2} \end{bmatrix} \\ &= \frac{-E_0(\sqrt{R_2} + Y(\varphi))}{2\sqrt{2}} \begin{bmatrix} 1 \\ 0 \end{bmatrix} \end{aligned} \quad (11.18)$$

For the field at detector D2:

$$\begin{aligned} \begin{bmatrix} D_{2,x} \\ D_{2,y} \end{bmatrix} &= \frac{-E_0}{2\sqrt{2}} \begin{bmatrix} 0 & 0 \\ 0 & 1 \end{bmatrix} \begin{bmatrix} \sqrt{R_2} + Y(\varphi) \\ j\sqrt{R_2} \end{bmatrix} \\ &= \frac{-E_0\sqrt{R_2}}{2\sqrt{2}} \begin{bmatrix} 0 \\ 1 \end{bmatrix} \end{aligned} \quad (11.19)$$

The difference from the detectors:

$$\begin{aligned}
 R(\lambda) &= D_{1,x}^2 - D_{2,y}^2 = \frac{E_0^2}{8} \left( \left| \sqrt{R_2} + Y(\varphi) \right|^2 - R_2 \right) \\
 &= \frac{E_0^2}{8} \left( \sqrt{R_2(\lambda)} \sqrt{R_{ref}} e^{j \frac{2\pi L_{ref}}{\lambda}} + \sqrt{R_2(\lambda)}^* \sqrt{R_{ref}} e^{-j \frac{2\pi L_{ref}}{\lambda}} + R_{ref} \right)
 \end{aligned} \tag{11.20}$$

First two components represent the interferences between the reference reflector and FBGA and the third is a DC component. The result of Eq. 11.20 shows that the cavity interferences, represented by  $R_2$ , are removed. For both FPI and the Michelson configuration, the couplers are assumed to be insensitive to polarization and the resulting field from the FBGA is circularly polarized. The latter may be challenging since a standard fiber is unable to maintain polarization for a significant length. However, mechanically tweaking the relative angle between the two polarizers may be used to correct for non-ideal situations in order to suppress the cavity interferences.

#### 11.4. Conclusion

We have successfully simulated a 2 meter FBGA, attached to a 2 meter cantilever beam structure, using Transfer Matrixes (TM) and Optical Frequency Domain Reflectometry (OFDR) demodulation technique. The Transfer Matrices were acquired from the solutions of the couple mode theory. Two TM were used to suppress the cavity interferences without the need to added extra fiber to down shift the cavity interference to a lower frequency band, potentially saving fiber material. The cantilever beam is first simulated using a finite element model (FEM) to determine displacement and strain

response given a 500 N end force and the results are used as inputs to the FBGA. The results from the OFDR demodulation are then compared to the results from the FEM. The results show that the C-OFDR demodulation of the FBGA system agrees with the FEM input to within 0.26 %. An additional technique to aid in the cavity suppression may require the use of all three methods of cavity suppression. First, the cavity interferences can be placed between the FBGA-reflector interferences by properly designing the FBGA as was done in Chapter 10. If the FBGs are equally spaced, the optimum reflector position would be one half of the FBG spacing. This will eliminate any possibility of interferences with FBGA-reflector interferences. Second, the cavity subtraction method can then be used to significantly reduce the cavity interferences. Third, if higher order interferences become a problem, it will require decreasing the FBG reflectivity. Finally, a peak finding algorithm can then be used to automatically capture the FBGA-reflector interference peaks in the Fourier domain. In addition to the ideal simulation of cavity subtraction method discussed, a practical design is proposed using polarization devices and a circularly polarized source. The results show that this technique gives similar form as the ideal cavity subtraction method. However, other consideration must be taken into account, for example, non-ideal reflectances from the polarization devices and polarization insensitivity of standard optical fibers.

## 12. SUMMARY AND FUTURE WORK

### 12.1. Summary

This work describes practical application in Infrastructure Optics. Infrastructure Optics is a derivative of smart structures and is defined as the research, development, deployment of optic systems, primarily fiber optic sensor and communication technology, for use in infrastructure health monitoring. This includes embedding or attaching sensor networks into structures such as high value buildings, roads, highways, and bridges, in order to monitor various parameters such as temperature, strain, and pressure over a wide area. Towards this end, this research has developed an integrated design and simulation platform in which all three key components such structural analysis, sensor networks, and signal processing are able to be analyzed simultaneously. The Optical and Structural Simulation (OSS) software is used to design fiber Bragg grating strain sensor arrays with Coherent Optical Frequency Domain Reflectometry (C-OFDR) interrogation for use in monitoring a cantilever beam structure. C-OFDR has shown promise in its use in infrastructure health monitoring. C-OFDR has the ability to interrogate thousands of identical fiber Bragg gratings; this offers a significant advantage compared to competing technologies such WDM and OTDR. Using the OSS software, three key areas of FBGA/C-OFDR research are tackled: modeling and cavity suppression. In the modeling area, the transfer matrix technique is employed to model the FBGA/C-OFDR system. Compared to other techniques, the transfer matrix offers a system wide approach to modeling the system and is more accurate and precise compared to current modeling

techniques in the literature since the actual reflectivity of the system can be determined. This method was employed in the design and simulation of a 15.3 cm, 3-element fiber Bragg grating array. The array was designed in such a way that the cavity interferences did not overlap with reflector-FBGA interferences. The FBGA was then fabricated, calibrated using Fabry-Perot stain gauge calibrator, and testing on a 75 cm aluminum cantilever beam. The results showed that the tunable laser employed had significant noise issues do to its tuning mechanism. However, recovery of the FBG spectrums were achieved using C-OFDR, and axial strain tests on the cantilever beam showed agreement with three co-located electric strain gauges as the cantilever beam was deflected.

The next half of this work focused on suppressing the cavity interferences using the cavity interference suppression technique. The cavity interference suppression technique, directly subtracts the cavity interferences from the overall interference signal. Compared to current suppression technique, the cavity interference suppression technique does not require down shifting the cavity interferences to a lower frequency band or require significantly reducing the reflectivity of the FBGs. This effectively reduces the bandwidth of the FBGA/C-OFDR system by one-half compared to the down shifting method. The cavity interference suppression technique is modeling using two Transfer Matrices (TM). One transfer matrix contains cavity interference information while the second contains the entire interference signal. The resulting reflectances of the two matrices are then subtracted to suppress the cavity interferences. This technique was used on a 2-meter, 9-element FBGA attached to a 2-meter steel cantilever beam. Structural information of the cantilever beam is calculated using finite element modeling and the

axial strain results are applied to each element of the FBGA. Using C-OFDR, the axial strain information was recovered and then compared to the FEM input. The results show that cavity interference suppression is achieved for load and no load conditions and good agreement is achieved with the FEM inputs. In addition to the ideal simulation of cavity interference suppression method discussed, a practical design is proposed using polarization devices and a circularly polarized source. The results show that this technique gives similar form as the ideal cavity subtraction method. However, other consideration must be taken into account, for example, non-ideal reflectances from the polarization devices and polarization sensitivity of standard optical fibers.

## **12.2. Future Work**

This section discusses some practical applications and future work in FBGA/C-OFDR systems. It is hoped that other researchers will find interest.

### **12.2.1. Bandwidth Reduction**

A disadvantage of the FBGA design so far discussed in this work (cf. Figure 12.1(a)), in addition to coherence and stability requirements for the tunable laser, occurs for long haul FBGA  $> 1\text{km}$  in length. A long haul FBGA requires higher bandwidth to achieve reasonable scans time, limiting its usefulness. C-OFDR interrogations are also very difficult to implement for dynamic measurements. This dissertation is focused on static strain measurements using FBGA. For a dynamic case, for example, if frequency of a vibrating structure is 2.5 Hz, the scan time must be less than 0.2 sec, taking into the Nyquist criterion for two sampling. Assuming an FBGA system length of 46 meters,

wavelength scanning range of 7 nm for the tunable laser, and a Bragg centered wavelength at 1550 nm for the gratings, the bandwidth of the C-OFDR must be greater than 1.9 Mhz. A laser source must be able to scan 7 nm in 0.2 seconds smoothly and without any jitters. As can be seen, it would be difficult to implement C-OFDR in the measurement of vibration of structures above several Hertz. Shlyagin, et al. (1998) recognized the bandwidth issue for long haul FBGA and used the interference between two adjacent FBGs in the array to create an array of Fabry-Perot Interferometers (FPI) as shown in Figure 12.1(b). This relaxed the requirements on the tunable laser and the detection system. The FPIs are separated from each other by some distance to avoid interference. By varying the FPI cavity length, each FPI will have a distinct peak in the frequency domain. The advantage of this type of design is that the bandwidth is independent of the FBGA length but dependent on the maximum cavity spacing. The disadvantage is that they are FPI, and two fringe peaks in the wavelength domain (Measures 2004, Udd 1995) are required to determine changes in the cavity length, thus, determine the strain, not very convenient from a signal processing point of view. In order to take advantage of the two designs, they can be combined to form a third design as shown in Figure 12.1(c). Here, two smaller FBGA sections are connected together using a phase line in order to push the interference between the two sections outside the measurement bandwidth. By varying the relative position of the reference reflectors, the two FBGA sections can occupy the same spatial position in the frequency domain, thus, occupy the same frequency bandwidth. For example, if the FBGs are identical and have the same spacings, then N-sections can be incorporated if the FBGs are spaced N times

the length of a single FBG. Now, the bandwidth is dependent on the maximum length of the FBGA section instead of the overall length of the combined array. A clear disadvantage of this type of design is a delay line has to be used. If a length of fiber is used as a phase line, then a length as long as the FBGA section or greater than the coherence length of the laser is required. This may require controlling the coherence length of the laser so that its length is smaller than the length of a single section. Also, cavity interferences can super-impose on the reflector-FBGA interferences.

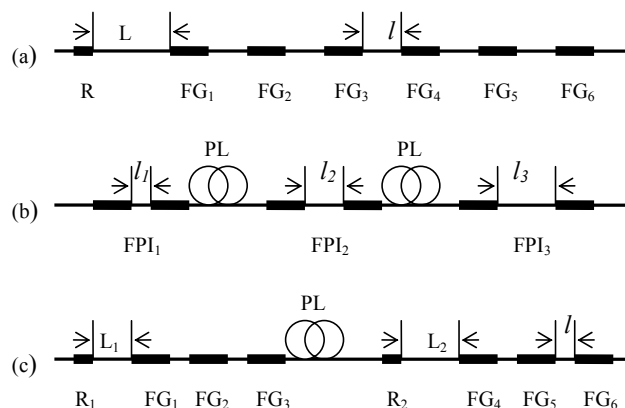


Figure 12.1 Several FBGA designs. (a) Regular single line FBGA (b) Array of Fabry-Perot Interferometers (FPI) connected through phase lines (PL). (c) Two smaller FBGA sections connected through a phase line (PL).

### 12.2.2. 2D FBGA/C-OFDR systems

In Figure 12.2, wavelength division multiplexing and OFDR interrogation is used to create a 2-D FBGA. The vertical and horizontal FBGs have different nominal wavelengths, and a highly reflective FBG is used to separate both wavelengths. The task here is to determine ways to give each FBG in the array a unique path length so that C-OFDR can be used to separate each FBG in the Fourier spectrum.

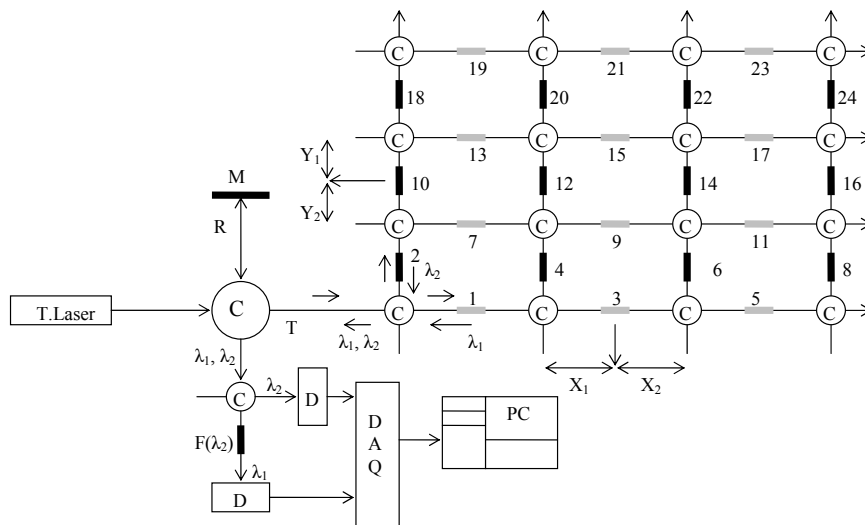


Figure 12.2 2D FBGA system

## REFERENCES

- Abdi, A.M. and Kost, A.R. (2006a), "Cavity interference suppression in a fiber Bragg grating array interrogated with coherent optical frequency domain reflectometry", submitted to IOP: Smart Materials and Structures Journal.
- Abdi, A.M., Suzuki, S., Schülzgen, A., and Kost, A.R. (2006b), "Fiber Bragg Grating Strain Sensor Array with Coherent Optical Frequency Domain Reflectometry", Invited Paper, submitted to *Journal of Smart Structures and Systems, an International Journal*.
- Abdi, A.M., Suzuki, S., Schülzgen, A., and Kost, A.R. (2005a), "Strain Measurements Using Fiber Bragg Grating Array," in Technical Digest, Frontiers in Optics, the 89<sup>th</sup> Annual Meeting of the Optical Society of America, paper FWO5, Tucson, AZ, October 19, 2005.
- Abdi, A.M., Suzuki, S., Schülzgen, A., and Kost, A.R. (2005b), "Fiber Bragg Grating Array Calibration", in *Smart Structures and Materials 2005: Sensors and Smart Structures Technologies for Civil, Mechanical, and Aerospace Systems*; Masayoshi Tomizuka, Chair, *Proceeding of SPIE v 5765*, 552-563.
- Abdi, A. M. and Kost, A. (2004), "Infrastructure Optics", *Proceeding of SPIE v5384, Smart Structures and Materials*, 218-228.
- Abdi, A.M. and Watkins, S.E. (2003), "Four-point calibration of PVDF sensor using extrinsic Fabry-Perot interferometric (EFPI) sensor", in *Smart Structures and Materials 2003: Smart Sensor Technology and Measurement Systems*; Daniele Inaudi, Eric Udd; Editors, *Proceedings of SPIE v 5050*, 71-80.
- Abdi, A. (1999), "Neural network demodulation for frequency response measurement of a fiber optic-based smart beam," MS Thesis, University of Missouri-Rolla, T7627.
- Alavie, A. T., Maaskant, R., Stubbe, R., Othonos, A., Ohn, M., Sahlgren, B., and Measures, R. M. (1995), "Characterization of fiber Bragg grating sensors and their relation to manufacturing technique", *Proceedings of SPIE v2444*, 528-535.
- Aktan, A.E., Catbas, F.N., Grimmelsman, K., Pervispour, M, Curtis, J., Shen, K., and Qin, X. (2002), "Health Monitoring for Effective Management of Infrastructure", *Smart Structures and Materials 2002: Smart Sensor Technology and Measurement Systems, Proceedings of SPIE. v4696*, 17-29.

Battiato, J. M. (1998), "Fiber Bragg Gratings", PhD Thesis, University of Arizona, E9791 1998 325.

Brooks, A. C., Froggatt, M. E., Allison, S. G., Moore, T. C., Sr., Hare, D. A., Batten, C. F., and Jegley, D. C. (2001), "Use of 3000 Bragg grating strain sensors distributed on four eight-meter optical fibers during static load tests of a composite structure", in *Smart Structures and Materials 2001: Industrial and Commercial Applications of Smart Structures Technologies, Proceeding of SPIE v4332*, 133-

Childers, B. A., Brown, T. L., Moore, J. P., and Wood, K. H. (2002), "Recent developments in the application of optical frequency domain Reflectometry to distributed Bragg grating sensing", *Proceedings of SPIE v4578, Fiber Optic Sensor Technology and Application*, 19-31. Childers,

Duncan, R. G., Childers, B. A., Gifford, D. K., Pettit, D. E., Hickson, A. W., and Brown, T. L. (2002), "Distributed sensing technique for test article damage detection and monitoring", *Proceeding of SPIE v5050, Smart Structures and Materials*, 367-375.

Eagar T.W. and Musso, C. (2001), "Why Did the World Trade Center Collapse? Science, Engineering, and Speculation," *The Journal of the Minerals, Metals, and Materials Society*, **53** (12), 8-11.

Figliola, R. S. and Beasley, D.E. (2000), *Theory and Design for Mechanical Measurements*, John Wiley and Sons, Inc., New York, NY.

Froggatt, M. and Moore, J. (1998a), "Distributed measurement of static strain in an optical fiber with multiple Bragg gratings at nominally equal wavelengths", *App. Optics*, **37**(10), 1741-1746.

Froggatt, M. and Moore, J. (1998b), "High-spatial-resolution measurement in optical fiber with Rayleigh scatter", *App. Optics*, **37**(10), 1735-1740.

Froggatt, M. (1996), "Distributed measurement of the complex modulation of a photo-induced Bragg grating in an optical fiber", *App. Optics*, **35**(25), 5162-5164.

Fuhr, P. L. and Huston, D. R. (1993), "Multiplexed fiber optic pressure and vibration sensors for hydroelectric dam monitoring", *Smart Mater. Struct.*, **2**, 260-263.

Gandhi, M.V. (1992), *Smart Materials and Structures*, 1<sup>st</sup> ed.. Chapman and Hall, London, UK.

Ghatak, A., and Thyagarajan, K. (1998), *Introduction to Fiber Optics*, Cambridge University Press, Cambridge, UK.

Goodman, J.W. (1996), *Introduction to Fourier Optics*, McGraw Hill, Boston, Mass.

Gregory, G. A, Fox, R. L., Froggatt, M. E., and Childers, B. A. (2002), "Novel piezoelectric actuators for tuning an optical fiber Bragg grating", *Opt. Eng.*, **41**(10), 2448-2455.

Kashyap, R. (1999), *Fiber Bragg Gratings*, Academic Press, London, UK.

Kobayashi, A.S., *Handbook of Experimental Mechanics* (1993), VCH Publishers, Inc, New York, New York.

Kostuk, R. (2002), Holography and Diffraction OPTI 527 class notes, College of Optical Sciences, University of Arizona.

Kostuk, R. (2001), Fiber Optics Laboratory OPT587 class notes, College of Optical Sciences, University of Arizona.

Kundu, T. (2003), Wave propagation in solids CE 603 class notes, Civil Engineering and Engineering Mechanics, University of Arizona.

Lau, K., Zhou, L., Tse, P., Yuan (2002), "Applications of composites, optical fibre sensors and smart composites for concrete rehabilitation", *Applied Composite Materials*, **9**, 221-247.

MacDonald, R.I. (1981), "Frequency domain reflectometer", *Applied Optics*, **20**(10), 1840-1844.

Measures, R. M. (2001), *Structural Monitoring With Fiber Optic Technology*, Academic Press, San Diego, CA, 2001.

Milsters, T. (2002), Diffraction and Interferometry OPTI 505 class notes, College of Optical Sciences, University of Arizona,

Okamoto, K. (2000), *Fundamentals of Optical Waveguides*, Academic Press, New York, NY.

Olson, N.G., Leung, C.K.Y., and Meng, A. (2002), "Mechanical behavior of optical fiber strain sensors", in *Fiber Optic Sensor Technology and Application, Proceedings of SPIE v4578*, 328-335.

Passy, R., Gision, N., Weid, J. P. von der, and Gilgen, H. (1994), "Experimental and Theoretical Investigations of Coherent OFDR with Semiconductor Laser Sources", *Lightwave Technol.*, **12**( 9), 1622-1630.

Pierce, G., MacLean, A., and Culshaw, B. (2000), "Optical frequency-domain reflectometry for microbend sensor demodulation", *Appl. Optics*, **39**(25), 4589-4581.

R. W. Basedow, T.D. Cocks, "Piezoelectric ceramic displacement characteristics at low frequencies and their consequences in Fabry-Perot interferometer", *Journal of Physics E: Scientific Instruments*, **13**(8), 840-844 (1980).

Shlyagin, M.G., Miridonov, S.V., and Spirin, V.V. (2002), "Overview of fiber optic sensor activities at Mexican research center CICESE", in *Fiber Optic Sensor Technology and Application 2001*, Proceedings of SPIE v4578, 8-17.

Spammer, S.J. and Fuhr, P.L. (1998), "Concrete embedded optical fiber Bragg grating strain sensors", in *Industrial Electronics, 1998. Proceedings. ISIE '98. IEEE International Symposium on Industrial Electronics*, **1**, 330-334.

Sun, F., Xiao G., Zhang Z., and Grover C.P. (2004), "Piezoelectric bimorph optical-fiber sensor", *Applied Optics*, **43**(9), 1922-1925.

Udd, E. (1995), *Fiber Optic Smart Structures*, 1<sup>st</sup> ed., Wiley & Sons, New York, NY.

Ulrich, R. and Eickhoff, W., "Optical Frequency domain reflectometry in single-mode fiber", *Applied Physics Letters*, **39**(19), 693-695.

Vries, M del, Nasta, M., Bhatia, V., Tran, T., Greene, J., and Claus, R.O. (1995), "Performance of embedded fatigue loaded reinforced concrete specimen," *Smart Mater. Struct*, **4**, A107-A113.

Woerner, D.F. (2002), "The selection and infusion of autonomy for Mars rovers", in *2002-First-International-IEEE-Symposium on 'Intelligent-Systems'*, *Proceedings of IEEE*, **1**, 86-91

Yu, F.T.S. and Yin, S. (2002), *Fiber Optic Sensors*, 1<sup>st</sup> ed., Marcel Dekker, Inc., Madison Avenue, NY.